

**Structural Characterization of Thin Films of Molecules on Solid Surfaces: Development  
of a Portable UHV Chamber to Bridge RHEED and SFG Spectroscopy Techniques**

by  
Hamed Vali

A Dissertation Submitted to the Department of Chemistry,  
College of Natural Science and Mathematics  
in partial fulfillment of the requirements for the degree of

DOCTOR OF PHILOSOPHY

in Chemistry

Chair of Committee: Ding-Shyue Yang

Co-Chair of Committee: Steven Baldelli

Committee Member: Shoujun Xu

Committee Member: Melissa Zastrow

Committee Member: Paul Ruchhoeft

University of Houston  
December 2021

Copyright 2021, Hamed Vali

## **DEDICATION**

This dissertation is dedicated to my wife, our parents, and our brothers, and the memory of our two unforgettable losses, Aziz and Maman Zari.

## ACKNOWLEDGMENTS

In my Ph.D., I received support from many people and friends who helped me during hard times to finish this journey.

Special thanks to my two advisors, Dr. Ding-Shyue Yang and Dr. Steven Baldelli, who has always supported me since the first day to build up my knowledge and skills and be always interested in gaining more knowledge. I appreciate their trust and patience during hard times.

Special thanks to our postdoctoral scholar, Dr. Xing He, who helped me endlessly with a theoretical understanding of the RHEED and the experimental part.

I would also like to thank my lab-mates, Mazhar Chebl, Alamdar Shah, and Mithun Gosh, for their friendly assistance when they were asked and their emotional support in some of the most challenging moments of my Ph.D. life.

I want to thank Mark Bushman and Boris Makarenko, who helped me in the process of designing the instruments without hesitation.

Lastly, I want to thank my wife and family for their love and support and my friends for their help.

Thanks to whoever was slightly related to the past years of this big transition of my life.

## ABSTRACT

In surface science, it is often essential to visualize and obtain the structures of molecules at solid-liquid and solid-vacuum interfaces. Each surface characterization method has its advantages and disadvantages, and there is no single technique that can provide all possible information about one sample. Therefore, the combined use of complementary surface science methods may offer a more detailed picture of the system. One must then consider multiple factors depending on the nature of the methods or the samples under study. This thesis describes studies of selected interfacial structures, taking advantage of the strengths of reflection high-energy electron diffraction (RHEED) and sum-frequency generation (SFG) spectroscopy techniques, which include thin films of ionic liquids (ILs) deposited by physical vapor deposition and self-assembled monolayers on gold. A thickness-dependent structural transition of ILs on highly-oriented pyrolytic graphite (HOPG) was observed by RHEED, where an ordered structure for 2–10-nm films was found at low temperatures while no apparent 3D crystallization was found for films thinner than 2 nm nominally and thicker than ~10 nm. An open question about the structural details is discussed, which motivates the design of a portable setup to maintain the sample under vacuum and bridge the RHEED and SFG techniques. Furthermore, a combined study using RHEED and SFG on rubrene single crystals and a temperature-dependent SFG study in a high-vacuum cell are two other case studies in this thesis. In summary, this work enables a vast possibility of future experiments to investigate structures of thin films, their interactions with other systems, studies on both sides of a thin film (film-solid, film-vacuum) interfaces.

The support of an R. A. Welch Foundation grant (E-1860) and a National Science Foundation grant (CHE-1653903) is acknowledged.

# TABLE OF CONTENTS

<b>DEDICATION</b> .....	<b>iii</b>
<b>ACKNOWLEDGMENTS</b> .....	<b>iv</b>
<b>ABSTRACT</b> .....	<b>v</b>
<b>TABLE OF CONTENTS</b> .....	<b>vi</b>
<b>LIST OF TABLES</b> .....	<b>ix</b>
<b>LIST OF FIGURES</b> .....	<b>x</b>
<b>1 Chapter 1: Introduction</b> .....	<b>2</b>
1.1 History of Surface Science.....	2
1.2 Surfaces and Interfaces .....	3
1.3 Molecular-level surface chemistry.....	5
1.4 Bibliography .....	10
<b>2 Chapter 2: Techniques, Theories, and Data Analysis Parameters</b> .....	<b>14</b>
2.1 Reflection High-Energy Electron Diffraction.....	14
2.2 Principle of Electron Diffraction .....	15
2.2.1 Electron Waves .....	15
2.2.2 Reciprocal Lattice, Diffraction Laws, and Ewald Sphere.....	16
2.2.3 Atomic Scattering Factor and Geometrical Structure Factors .....	19
2.2.4 RHEED Experimental Geometry.....	19
2.2.5 Examples of RHEED Pattern.....	20
2.2.6 Rocking Curve .....	22
2.2.7 Mean Free Path and Electron Penetration Depth.....	23
2.3 Sum Frequency Generation Spectroscopy .....	23
2.3.1 Theory .....	23
2.3.2 Instrumental Setup .....	26
2.3.3 SFG Spectra Fitting.....	28
2.4 Conclusion .....	29
2.5 Bibliography .....	30
<b>3 Chapter 3: Ordered-Disordered Structural Transition of Ionic Liquid on Highly Oriented Pyrolytic Graphite (HOPG)</b> .....	<b>33</b>
3.1 Introduction.....	33
3.2 Experimental.....	37

3.2.1 Ultrahigh Vacuum System.....	37
3.2.2 Ionic Liquid Thin Film Deposition.....	38
3.2.3 RHEED Experiment.....	40
3.3 Results and Discussion .....	40
3.3.1 Room Temperature Structure of the IL on HOPG.....	40
3.3.2 Low-Temperature Structure of the IL on HOPG.....	42
3.3.3 Lattice Parameters Calculation for a Rectangular Unit Cell.....	48
3.3.4 Vertical Spacing –The Rocking Curve .....	50
3.4 Conclusion .....	55
3.5 Bibliography .....	57
<b>4 Chapter 4: Development of the Portable UHV chamber .....</b>	<b>63</b>
4.1 Introduction.....	63
4.2 Design Limitations.....	66
4.2.1 Sample Transfer Type.....	66
4.2.2 SFG Optical Setup .....	67
4.3 Sample Transfer General Steps.....	67
4.3.1 RHEED Setup .....	68
4.3.2 Position of the Portable Chamber .....	69
4.4 Portable Chamber Design .....	71
4.4.1 Fully Assembled Portable Chamber .....	72
4.4.2 Step-by-Step Sample Transfer .....	72
4.4.3 Sample Car Bayonet Connection.....	74
4.4.4 Sample Car Details .....	75
4.4.5 Custom-Made Sample Receiver .....	79
4.4.6 Optical Window Design.....	79
4.5 Conclusion .....	81
4.6 Bibliography .....	82
<b>5 Chapter 5: Surface Structure Analysis of Rubrene Single Crystals .....</b>	<b>84</b>
5.1 Introduction.....	84
5.2 Experimental.....	85
5.2.1 Rubrene Single Crystal .....	85
5.3 RHEED and SFG Data.....	87
5.3.1 RHEED Data.....	87
5.3.2 SFG Data.....	92

5.4 Analysis and Discussion .....	94
5.5 Bibliography .....	99
<b>6 Chapter 6: Low-Temperature Study of Self-Assemble Monolayers on Gold .....</b>	<b>104</b>
6.1 Introduction.....	104
6.2 Gold Substrate and SAM Sample Preparation.....	105
6.3 High-Vacuum Setup.....	106
6.4 Low-Temperature SFG of n-Alkanethiol Monolayers on Gold .....	110
6.5 SFG Experimental Data and Discussion.....	112
6.6 Future Work .....	116
6.7 Conclusion .....	118
6.8 Bibliography .....	119
Appendix A.1 Reported crystal structures of the ILs.....	123
Appendix A.2 Example of the reciprocal lattice vectors calculation:.....	125
Appendix A.3 Simulation Details .....	125
Appendix B.1 Additional pictures of the portable chamber.....	128

## LIST OF TABLES

Table 3-1 Some of the properties of EMIM FSA IL .....	39
Table 3-2 Mean-free path and penetration depths of electron for elastic scattering condition at 30 keV .....	40
Table 3-3 Summarized film thicknesses, ordering horizontally and vertically for each film thickness.....	44
Table 3-4 Selected ILs – Crystallize with $\alpha=\beta=\gamma=90^\circ$ . T (C) is crystallization temperature in Kelvin.....	47
Table 3-5 [EMIM][TFSA] streaks indexing from simulation .....	48
Table 3-6 [EMIM][FSA] Experimental streaks vs. [EMIM][TFSA] simulated streaks positions. ....	49
Table 3-7 The qualitative comparisons of the four ILs' thin films on HOPG substrate with respect to the [EMIM][TFSA] film quality based on the RHEED diffraction patterns.....	54
Table 4-1 The relation between pressure and the time a monolayer is created on a surface.....	64
Table 5-1: RHEED analysis of the single crystal rubrene surface performed along different surface indices .....	88
Table 5-2 Orientational parameters for the orientational analysis of the phenyl groups of the rubrene on the surface.....	98
Table 6-1 Abbreviations for labeling the plots and their definition.....	113

# LIST OF FIGURES

Figure 1-1. Timeline of the historical development of surface chemistry, regenerated from reference [1].....	2
Figure 1-2. An example of the interface in our everyday life.....	3
Figure 1-3. Ordering range of the deposited thin films on a solid substrate.....	7
Figure 2-1 A schematic view of Bragg reflection from a set of parallel lattice planes with a distance of $d$ . .....	17
Figure 2-2 Scattering of the two incident waves from two scatterers and a set of parallel planes shows the relation between Laue and Bragg condition reproduced based on reference [4]. .....	18
Figure 2-3 Ewald sphere construction and the corresponding reciprocal lattice point that touches the Ewald sphere and satisfies the diffraction condition. ....	19
Figure 2-4 Schematical geometry of RHEED. The incident electron on the surface and the diffracted beam on the phosphor screen. ....	20
Figure 2-5 Four different types of surfaces and their general diffraction features in RHEED patterns [6].....	21
Figure 2-6 Schematic RHEED pattern at one specific angle, the middle streak, and the selected area to create the rocking curve. ....	22
Figure 2-7 Schematic description of the SFG setup and SFG process. ....	25
Figure 2-8 Schematic view of a polarized light. ....	27
Figure 2-9 Schematic of the ESKPLA laser [17].....	27
Figure 2-10 OPG/OPA schematic outline, from refrence [19].....	28
Figure 3-1 Selected cations and anions composing the most common ionic liquids.....	33
Figure 3-2 The two anions are mainly discussed in this chapter. ....	36
Figure 3-3 RHEED images of (a) HOPG before IL deposition (b) As-deposited IL on HOPG (c) HOPG after desorbing the IL at elevated temperatures .....	41
Figure 3-4 RHEED images of the HOPG substrate at different parts of the substrate (Z scan images).....	42
Figure 3-5 Crystallization of the 2.4 nm film IL on HOPG by lowering the temperature (from (a) to (h)). ....	42

Figure 3-6 RHEED images of (a) 3.2 nm film IL on HOPG at low temperature. ....	43
Figure 3-7 Schematic of an azimuthally averaged RHEED pattern. ....	44
Figure 3-8 General possibility of 2-D unit cell structures of a crystal.....	45
Figure 3-9 (a and b) The ILs with similar cations and anions and different anion symmetry result in different crystal structures. ....	47
Figure 3-10 The anions of the ILs compared in the main text.....	48
Figure 3-11 The rocking curve for [EMIM][FSA] IL. ....	51
Figure 3-12 (Left) In-plane lattice mismatch for the predicted IL lattice parameters (a and b). ..	52
Figure 3-13 Typical intensity changes of the IL diffraction spots as a function of temperature in cooling (green) and heating (red) cycles.....	55
Figure 4-1 Omicron-type sample transfer (A) The commercial transfer head, the rotational sample stage/manipulator, and the two pins' engagement grab the omicron plate. (B) Three main parts of the transfer arm head (C) The sample stage block, with the omicron plate (D) The omicron plate with a sample. ....	67
Figure 4-2 Height and angle limitation on the SFG setup. ....	68
Figure 4-3 RHEED general setup and main parts.....	69
Figure 4-4 The position of the detachable portable chamber. ....	70
Figure 4-5 Sample transfer between two chambers with two separate transfer arms.....	71
Figure 4-6 Schematic side view of the portable chamber assembled on the ionic liquid chamber .....	72
Figure 4-7 Sample car design and the transfer arm head.....	73
Figure 4-8 Sample car engagement.....	74
Figure 4-9 The overview of the sample car layers.....	76
Figure 4-10 Calibration curves for the resistive heater.....	77
Figure 4-11 Heating and natural cooling curves.....	78
Figure 4-12 The cooling rate of the sample plate for the portable chamber.....	78
Figure 4-13 The portable chamber side view with the two input laser beams and the SFG output beam.....	80

Figure 4-14 The layout of the custom-made viewport for the portable chamber .....	81
Figure 5-1 Molecular structure of rubrene. L, M, and N represent the three molecular axes. ....	86
Figure 5-2 Rubrene single crystal and its absorption spectrum along 4 different dotted lines.....	87
Figure 5-3 RHEED patterns of six selected zone axes to determine the surface arrangement of the molecules. ....	89
Figure 5-4 Rocking curve of the rubrene crystal. ....	90
Figure 5-5 The three scenarios of the rubrene single crystal surface and their corresponding diffraction features. ....	91
Figure 5-6 Experimental cell and SFG arrangement for rubrene single crystal. ....	92
Figure 5-7 Rubrene SFG for PPP polarization combination. ....	93
Figure 5-8 Rubrene SFG for SSP polarization combination. ....	94
Figure 5-9 The herringbone structure of the rubrene molecules.....	95
Figure 5-10 The phenyl ring on the surface of the rubrene crystal, the rotation angle, the tilt angle, and azimuthal angle, and their relation to (a,b,c) axis. ....	96
Figure 5-11 Orientational relation between three types of coordinates (crystallographic, molecular, and lab).....	97
Figure 5-12 Three different angle combinations of the phenyl ring.....	97
Figure 6-1 Schematic of an n-Alkanethiol SAM on a gold substrate and the three main parts of the molecule.....	105
Figure 6-2 The birdhouse shape cell (Green part) with two optical windows as input and output of the laser beam. ....	106
Figure 6-3 The cooling rate of the sample stage with liquid nitrogen .....	107
Figure 6-4 The bird cell on the SFG optical table, with all connections, including pumping, electrical, and thermocouple connections. ....	108
Figure 6-5 Inside the bird cell, with a resistive heater, thermocouple connection, and the custom-made resistive heater consists of a nichrome wire embedded inside an alumina ceramic. ....	108
Figure 6-6 The schematic outline of the assembly of the heating and cooling parts of the sample stage. ....	109
Figure 6-7 Two types of possible heating for the bird cell heater .....	110

Figure 6-8 The PPP polarization configuration for three samples with different chain lengths and three temperatures. (top-left) C <sub>10</sub> sample (top-right) C <sub>8</sub> sample (bottom-left) C <sub>18</sub> sample (bottom-right) Comparison of C <sub>10</sub> and C <sub>18</sub> .....	112
Figure 6-9 The SSP configuration data for C <sub>18</sub> sample at room temperature and lowest possible temperature (85 K).....	113
Figure 6-10 PPP data for C <sub>18</sub> sample for three selected scans for a 25 scans experiment.....	114
Figure 6-11 The PPP configuration data of the same sample, outside and inside the high vacuum cell, to compare the effect of the cell on the spectrum. ....	114
Figure 6-12 Reversibility check of the PPP peaks before and after cooling. ....	115
Figure 6-13 Reversibility check of the SSP peaks before and after cooling. ....	115
Figure 6-14 Decomposition of the C-H stretching region of ODT SFG data on gold.....	116
Figure 6-15 The PPP SFG data for ODT on a gold wafer and the fitting with six resonances. .	117
Figure 6-16 The Two in-plane and out-of-plane modes for asymmetric CH <sub>3</sub> .....	118

# Chapter 1

Introduction

# Chapter 1: Introduction

## 1.1 History of Surface Science

The history of surface science, particularly the chemistry of surfaces, originated over a thousands years ago, like the well-known phenomena of the oil spreading on the surface of the water, which was explained by Benjamin Franklin [1]. Gabor A. Somorjai, in his book about surface chemistry [1], shows a beautiful timeline about the development of surface science for the past two decades, as is shown in Figure 1-1, starting from the early 1800s and the catalysis application, and later the heterogeneous catalysis discovery, which has been considered as the birth of surface science. In 1927, Davisson and Germer discovered the surface diffraction of electrons [2]. In the 1950s, the possibility of economic development of ultrahigh vacuum (UHV) systems provided new possibilities and challenges in surface science due to the possibility of studying clean surfaces of single crystals for the first time and preparing surfaces and interface in a more controlled environment.

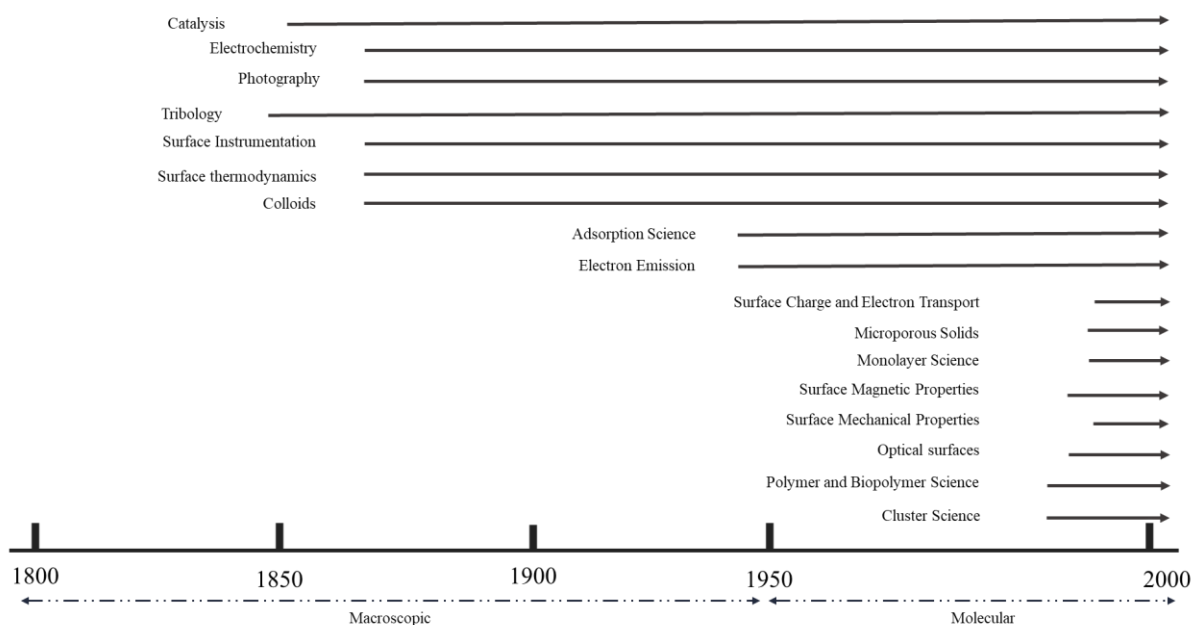


Figure 1-1. Timeline of the historical development of surface chemistry, regenerated from reference [1]

Many surface characterization techniques have been developed since the 1950s. Following the timeline in Figure 1-1, it is notable that many macroscopic properties have been studied at the molecular level since 1950, including adsorption, desorption, catalysis, phase transformation, and growth. After 1950 the development of these techniques and their combination created useful information to understand the surface and interface phenomena, both in the macroscopic and molecular levels.

## 1.2 Surfaces and Interfaces

Generally, surfaces/interfaces are defined based on the boundary of two phases of matters, including solid-liquid, solid-vacuum, and liquid-vacuum interfaces. These interfaces are found in our everyday life, like a ball in a beaker filled with water on a bench, as is shown in Figure 1-2. At the molecular level, these interfaces also exist, where the surfaces behave differently than the bulk due to their different chemical environment and the number of nearest neighbors.

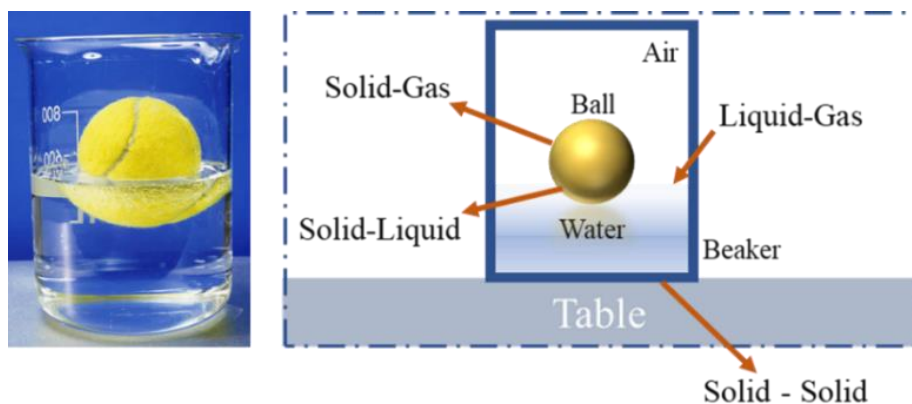


Figure 1-2. An example of the interface in our everyday life

The difference between the forces exerted on molecules inside an isotropic medium and at interfaces plays a vital role in their physical and chemical properties. Forces on molecules, applied by other molecules inside an isotropic medium, are generally centrosymmetric in all directions, while non-centrosymmetric at the interfaces. As a result, interfaces usually show properties that are different than those of the bulk. Chemical

activities at the interfaces usually dominate the chemical reactions [3], making the interfaces and surface chemistry one of the most extensive and crucial research areas for further development of many applications and material properties [1, 4]. As is shown in Figure 1-1, the molecular-level understanding of the surface properties is a significant research field in surface chemistry. By increasing the requirements for better control of surface and interface properties at the molecular level, elucidated understanding of chemistry at surfaces is growing every day. Even though there are fundamental developments in many surface chemistry industries, such as semiconductor-related devices [5] and biomedical-related devices [6], further development in surface characterization techniques are still required to extract more information from a system under study.

Aside from improving each surface characterization technique or developing new techniques, it is usually necessary to study one system with a combination of multiple surface characterization techniques to accumulate more data about one system due to the complexity of the systems under study. Many surface characterization techniques exist [4], which each one has its advantages and disadvantages. The combination of these techniques is a powerful tool to find answers in more detail for more complex systems, such as scanning tunneling microscopy (STM) and atomic force microscopy (AFM) studies on biological systems [7].

Each surface characterization technique has some capabilities and some limitations [4]. For example, STM provides information with direct imaging of an ordered surface using a change in current. In contrast, diffraction techniques like low-energy electron diffraction (LEED) provide indirect/average surface structural information using patterns created by electrons striking the sample surface along the surface normal and deflecting from the surface normal. Considering a sample studied with LEED and STM, while both techniques provide surface structural information, STM shows atomic size defects which are all averaged in the LEED diffraction pattern. The same comparison is true for any such techniques, while each provides some information that other techniques are not capable of.

### 1.3 Molecular-level surface chemistry

Understanding the molecular arrangement and orientation on the solid surface is a critical task in surface science since it is a critical parameter that controls phenomena that happen on surfaces and interfaces. These molecules are either simply the surface molecules of a molecular crystal, which might differ from the bulk molecules, or the molecules adsorbed on the surface of a solid, such as metals, and semiconductors.

Thin films can be created with different methods on a wide range of substrates. For example, two major types of adsorbed molecules on solid substrates are the organic thin films and the thin films of ionic liquids. The deposition of organic thin films on solid substrates was first reported more than a hundred years ago, and two major methods, which are known as self-assembled monolayers (SAMs), Langmuir-Blodgett (LB) films, are today well-established methods to create high-quality films on solid substrates [8]. Even though creating a high-quality LB film requires many parameters, such as a very clean setup, the self-assembly films are created in a regular lab environment in a solution [9]. The SAMs are also deposited with vapor deposition methods on solid substrates [10, 11] to better control the molecules' self-assembly. The thin-film deposition method from the gas phase of ionic liquids, using the physical vapor deposition method, was also reported in 2008 [12]. Usually, the UHV systems are equipped with additional cleaning parts, such as sputtering and heating stages for annealing, which creates the possibility of studying thin films in a controlled and clean environment. Vapor deposition of molecules is used to study the thin films for a more detailed understanding of molecular-level behavior of materials at interfaces, with many techniques such as X-ray photoelectron spectroscopy (XPS), temperature-programmed desorption (TPD), infrared spectroscopy, and sum-frequency generation [5-7, 10-27].

As mentioned, a big step in understanding surface phenomena at the molecular level happened when UHV-based techniques, like LEED, Auger electron spectroscopy (AES), and XPS became available. The next significant development in understanding surfaces and interfaces was providing correlation between

surface structures and the chemical properties of materials at the molecular level, which was achieved by combining different techniques and studying surface phenomena in situ, or even by isolating one molecule under study. There are many examples of these combinations that provide more details of one system by providing complementary information [14, 20-22, 24, 28-31].

Depending on the material under study, the importance of the cleanness of the sample surface varies dramatically. For example, the molecular surface orientation of a molecular single-crystal might be unaffected if it is exposed to air. At the same time, it might be affected if a thin film of the same molecule deposited on a solid substrate is exposed to air. To decide whether a property needs to be studied under a vacuum, many factors must be considered. It is usually not a straightforward task, and the decision is based on comparing experimental results. First, a clean environment must be defined. The details about a clean environment and necessity of that for some systems are discussed in Chapter 4. Generally, when an atomically clean surface is exposed to air, based on the flux of the gas molecules incident on the surface and the sticking coefficient, there is a time required to cover the surface with a monolayer of a gas molecule. For example, for a sticking coefficient of unity, this time is on the order of 1 h at  $10^{-9}$  torr pressure, before a monolayer of a gas with a molar weight of 28 g/mole is adsorbed on the surface at room temperature [1].

In addition, the property of the material under study defines the surface and the interface. A surface may be one atomic layer or several atomic layers. Understanding the surface/interface structures is one of the essential tasks to distinguish the surface from the bulk region for a specific property. For example, the familiar yellow color of gold atoms appears for a minimum of 50 layers of gold atom deposited on iron [1]. It means a minimum thickness of gold is required to generate the bulk optical properties resulting in that yellow color. Thin-film is a term used when a layer of a material with a fraction of nanometer to micrometers is deposited on another material (called the substrate). Since there is less material consumption for a thin film compared to their bulk, thin films are of great importance for real-world problems.

The study of thin-film structures is a crucial topic of surface science. The thin film deposition methods on a substrate are divided into two major categories: chemical deposition and physical deposition. Physical vapor deposition (PVD) is a technique with the thickness control of fractions of one nanometer. It is used to study surface-related applications, such as lubrication, electrodes, surface property modification, surface structures, and thickness-dependent properties. [12-15].

Most of the surface structural techniques provide information about only one side of the thin films. It means, as it is shown in Figure 1-3, the information is either from the top-most layer (Figure 1-3 (a)) or from the buried interface (solid-liquid interface, Figure 1-3 (b)). Combining these techniques is advantageous for providing more accurate structural information for both sides of the thin films.

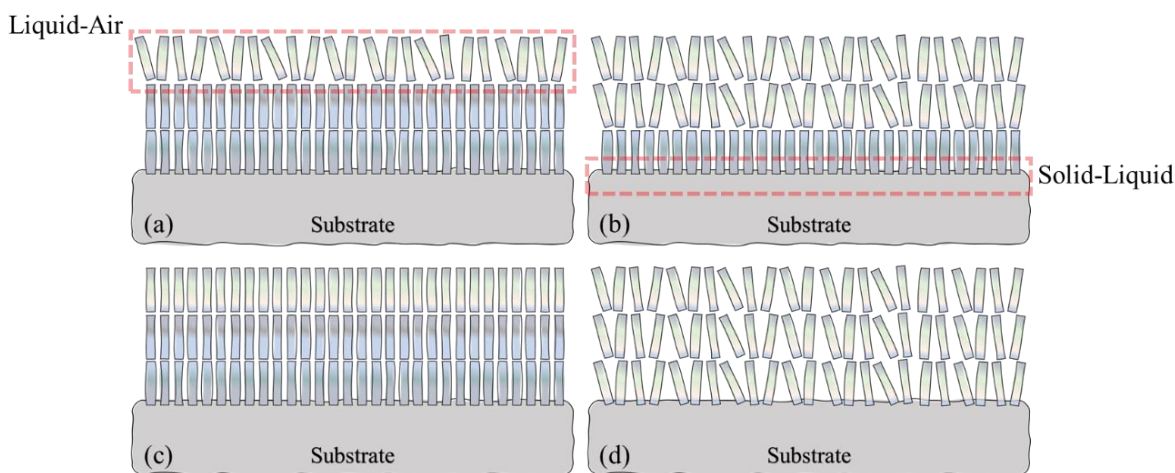


Figure 1-3. Ordering range of the deposited thin films on a solid substrate

One of the powerful combinations to study surface/interface structures, both for a molecular crystal and a thin film deposited on another substrate, is reflection high-energy electron diffraction (RHEED) and sum-frequency generation (SFG) spectroscopy combination. First, both techniques are surface sensitive. But the main strength of this combination is the result of the complementary structural information provided by combining them. Sum frequency generation spectroscopy is a powerful technique to extract structural information from buried interfaces, such as a solid-liquid interface (as shown in Figure 1-3 (b)) [13]. SFG can

extract orientational information and distribution information for both solid-liquid, and liquid-air interfaces, which has been used many times to study ionic liquids on solid supports [16, 18, 28, 32-37].

On the other hand, most optical spectroscopic techniques do not have good spatial resolution due to the diffraction limit of light. As a result, atomic coordination is poorly resolved with these techniques. As a result, to provide atomic and molecular information with higher resolution, the requirement is to use a proper electromagnetic wave or a matter-wave with a wavelength equal or less than the order of lattice constants. Among the three types of radiation, X-rays, neutrons, and electrons, which are used to study the structure of materials, each of them has advantages and disadvantages. Neutron sources are not readily available to every lab since nuclear reactors usually require strong and continuous neutron beams. In this technique, the neutrons are scattered by nuclei, which is stronger interaction than X-rays, which are only scattered by electron clouds of the nuclei. But the intensity of the neutron source is ten to a hundred million times weaker than that of X-rays, which as a result it takes much longer to record one frame of diffraction for neutron diffraction technique compared to the X-rays.

The other type of radiation to study the structure of materials is the electron. One of the important advantages of electron diffraction vs. X-ray diffraction is that the electrons scatter much stronger than the X-rays and penetrate less inside a material. Electrons are more sensitive to small volumes and generate high-quality patterns even for a very thin film of material in a short time, while X-rays are generally a better source for bulk crystallography. However, it means big samples are required to study a crystal using X-ray diffraction compared to the electron diffraction methods.

Thin films of materials are one example of a small volume of materials on a substrate, discussed previously in this chapter. Some of these thin films, such as thiol monolayers, are usually stable in air, while in some other cases, like the thin films of ionic liquids (ILs) on solid substrates, it can be affected if the sample is exposed to air. Thin films of the ILs show thickness-dependent structural transitions, which has been

reported previously [38]. The structural transition has three main regions, where before and after a specific film thickness, there is no crystallization, while in between, a crystallization of the IL thin films has been observed. To answer the question, whether the additional upper layers of the IL induce more disordered film on the bottom layers or not, or even whether there is some order of molecular ordering when there is no sign of crystallization, it is beneficial to combine RHEED and SFG, which is capable of answering to this type of questions.

The main purpose of this thesis is to provide the possibility to answer more fundamental questions about different types of thin films on solid substrates in a well-controlled environment. For this purpose, in Chapter 3, PVD-deposited ILs on highly oriented pyrolytic graphite (HOPG) is studied with RHEED in a thickness- and temperature-dependent approach in a UHV environment, and an open question is discussed. The necessity and benefit of bridging RHEED and SFG and its capability to answer the question are explained. A UHV system is designed and developed in the lab, customized for bridging the two techniques in Chapter 4. An example of a stable sample in the air is shown in Chapter 5. The organization and orientation of the molecules on the surface of a single crystal are studied by combining the two methods. Lastly, an unexpected peak disappearance for a well-studied thiol on gold is reported, which shows the possibility of new research directions, even for a well-defined material such as octadecanethiol (ODT) on gold. Even though the future possibilities are not limited to the abovementioned areas, in this thesis, the focus was on developing the systems to initiate the possibilities to combine these techniques.

## 1.4 Bibliography

- [1] G. A. Somorjai and Y. Li, *Introduction to Surface Chemistry and Catalysis*, John Wiley & Sons, 2010.
- [2] C. Davisson and L. H. Germer, "The scattering of electrons by a single crystal of nickel," *Nature*, vol. 119, no. 2998, pp. 558-560, 1927.
- [3] G. A. Somorjai and Y. Li, "Impact of surface chemistry," *Proceedings of the National Academy of Sciences*, vol. 108, no. 3, pp. 917-924, 2011.
- [4] J. C. Vickerman and I. S. Gilmore, *Surface Analysis: The Principal Techniques*. John Wiley & Sons, 2011.
- [5] J. Ekerdt, Y.M. Sun, A. Szabo, G. Szulczewski, and J. White, "Role of surface chemistry in semiconductor thin film processing," *Chemical Reviews*, vol. 96, no. 4, pp. 1499-1518, 1996.
- [6] P. D'Orazio, "Biosensors in clinical chemistry," *Clinica Chimica Acta*, vol. 334, no. 1-2, pp. 41-69, 2003.
- [7] P. Hansma, V. Elings, O. Marti, and C. Bracker, "Scanning tunneling microscopy and atomic force microscopy: application to biology and technology," *Science*, vol. 242, no. 4876, pp. 209-216, 1988.
- [8] A. Ulman, *Ultrathin organic films: From Langmuir-Blodgett to self-assembly*, Boston: Academic Press, 1991.
- [9] R. G. Nuzzo and D. L. Allara, "Adsorption of bifunctional organic disulfides on gold surfaces," *Journal of the American Chemical Society*, vol. 105, no. 13, pp. 4481-4483, 1983.
- [10] A. Eberhardt, P. Fenter, and P. Eisenberger, "Growth kinetics in self-assembling monolayers: a unique adsorption mechanism," *Surface Science*, vol. 397, no. 1-3, pp. L285-L290, 1998.
- [11] P. Schwartz, F. Schreiber, P. Eisenberger, and G. Scoles, "Growth kinetics of decanethiol monolayers self-assembled on Au (111) by molecular beam deposition: An atomic beam diffraction study," *Surface Science*, vol. 423, no. 2-3, pp. 208-224, 1999.
- [12] T. Cremer, M. Killian, J. M. Gottfried, N. Paape, P. Wasserscheid, F. Maier, and H. -P. Steinruck, "Physical vapor deposition of [EMIM][Tf<sub>2</sub>N]: a new approach to the modification of surface properties with ultrathin ionic liquid films," *ChemPhysChem*, vol. 9, no. 15, pp. 2185-2190, 2008.
- [13] S. Baldelli, "Interfacial structure of room-temperature ionic liquids at the solid-liquid interface as probed by sum-frequency generation spectroscopy," *The Journal of Physical Chemistry Letters*, vol. 4, no. 2, pp. 244-252, 2013.

- [14] M. Seah, "A review of the analysis of surfaces and thin films by AES and XPS," *Vacuum*, vol. 34, no. 3-4, pp. 463-478, 1984.
- [15] J. E. Mahan, *Physical vapor deposition of thin films*. 2000.
- [16] J. Bowers, M. C. Vergara-Gutierrez, and J. R. Webster, "Surface ordering of amphiphilic ionic liquids," *Langmuir*, vol. 20, no. 2, pp. 309-312, 2004.
- [17] C. S. Santos and S. Baldelli, "Surface orientation of 1-methyl-, 1-ethyl-, and 1-butyl-3-methylimidazolium methyl sulfate as probed by sum-frequency generation vibrational spectroscopy," *The Journal of Physical Chemistry B*, vol. 111, no. 18, pp. 4715-4723, 2007.
- [18] B. D. Fitchett and J. C. Conboy, "Structure of the room-temperature ionic liquid/SiO<sub>2</sub> interface studied by sum-frequency vibrational spectroscopy," *The Journal of Physical Chemistry B*, vol. 108, no. 52, pp. 20255-20262, 2004.
- [19] J. Zhao, E. G. Garza, K. Lam, and C. M. J. A. s. s. Jones, "Comparison study of physical vapor-deposited and chemical vapor-deposited titanium nitride thin films using X-ray photoelectron spectroscopy," *Applied Surface Science*, vol. 158, no. 3-4, pp. 246-251, 2000.
- [20] R. Atkin, S. Z. El Abedin, R. Hayes, L. H. Gasparotto, N. Borisenko, and F. Endres, "AFM and STM studies on the surface interaction of [BMP] TFSA and [EMIm] TFSA ionic liquids with Au (111)," *The Journal of Physical Chemistry C*, vol. 113, no. 30, pp. 13266-13272, 2009.
- [21] H. Yan and H. Okuzaki, "Effect of solvent on PEDOT/PSS nanometer-scaled thin films: XPS and STEM/AFM studies," *Synthetic Metals*, vol. 159, no. 21-22, pp. 2225-2228, 2009.
- [22] A. Baski and H. Fuchs, "Epitaxial growth of silver on mica as studied by AFM and STM," *Surface Science*, vol. 313, no. 3, pp. 275-288, 1994.
- [23] S. Tam and M.E. Fajardo, "Single and double infrared transitions in rapid-vapor-deposited parahydrogen solids: Application to sample thickness determination and quantitative infrared absorption spectroscopy," *Applied Spectroscopy*, vol. 55, no. 12, pp. 1634-1644, 2001.
- [24] S. Leroy, F. Blanchard, R. Dedryvère, H. Martinez, B. Carré, D. Lemordant, D. Gonbeau, "Surface film formation on a graphite electrode in Li-ion batteries: AFM and XPS study," *Surface and Interface Analysis: An International Journal devoted to the development and application of techniques for the analysis of surfaces, interfaces and thin films*, vol. 37, no. 10, pp. 773-781, 2005.
- [25] S. Sato, M. Tokumitsu, T. Sodesawa, and F. Nozaki, "Temperature-programmed desorption of dimethylpyridine adsorbed on silica-alumina prepared by chemical vapor deposition," *Bulletin of the Chemical Society of Japan*, vol. 64, no. 3, pp. 1005-1007, 1991.
- [26] K. Uosaki, Y. Shen, and T. Kondo, "Preparation of a highly ordered Au (111) phase on a polycrystalline gold substrate by vacuum deposition and its characterization by XRD, GISXRD, STM/AFM, and electrochemical measurements," *The Journal of Physical Chemistry*, vol. 99, no. 38, pp. 14117-14122, 1995.

- [27] P. C. Hiemenz and R. Rajagopalan, *Principles of Colloid and Surface Chemistry, Revised and Expanded*. CRC Press, 2016.
- [28] Y. Jeon, J. Sung, W. Bu, D. Vaknin, Y. Ouchi, and D. Kim, "Interfacial restructuring of ionic liquids determined by sum-frequency generation spectroscopy and X-ray reflectivity," *The Journal of Physical Chemistry C*, vol. 112, no. 49, pp. 19649-19654, 2008.
- [29] P. Hapala, G. Kichin, C. Wagner, F. S. Tautz, R. Temirov, and P. Jelínek, "Mechanism of high-resolution STM/AFM imaging with functionalized tips," *Physical Review B*, vol. 90, no. 8, p. 085421, 2014.
- [30] S. N. Magonov and M.H. Whangbo, *Surface analysis with STM and AFM: experimental and theoretical aspects of image analysis*. John Wiley & Sons, 2008.
- [31] J. Pethica and W. J. P. S. Oliver, "Tip surface interactions in STM and AFM," *Physica Scripta*, vol. 1987, no. T19A, p. 61, 1987.
- [32] S. Rivera-Rubero and S. Baldelli, "Surface spectroscopy of room-temperature ionic liquids on a platinum electrode: A sum-frequency generation study," *The Journal of Physical Chemistry B*, vol. 108, no. 39, pp. 15133-15140, 2004.
- [33] C. Romero and S. Baldelli, "Sum frequency generation study of the room-temperature ionic liquids/quartz interface," *The Journal of Physical Chemistry B*, vol. 110, no. 12, pp. 6213-6223, 2006.
- [34] C. Aliaga and S. Baldelli, "Sum frequency generation spectroscopy of dicyanamide based room-temperature ionic liquids. Orientation of the cation and the anion at the gas-liquid interface," *The Journal of Physical Chemistry B*, vol. 111, no. 33, pp. 9733-9740, 2007.
- [35] C. Aliaga, C. S. Santos, and S. Baldelli, "Surface chemistry of room-temperature ionic liquids," *Physical Chemistry Chemical Physics*, vol. 9, no. 28, pp. 3683-3700, 2007.
- [36] J. B. Rollins, B. D. Fitchett, and J. C. Conboy, "Structure and orientation of the imidazolium cation at the room-temperature ionic liquid/SiO<sub>2</sub> interface measured by sum-frequency vibrational spectroscopy," *The Journal of Physical Chemistry B*, vol. 111, no. 18, pp. 4990-4999, 2007.
- [37] W. Zhou, S. Inoue, T. Iwahashi, K. Kanai, T. Miyamae, D. Kim, Y. Katayama, Y. Ouchi, "Double-layer structure and adsorption/desorption hysteresis of neat ionic liquid on Pt electrode surface—an in-situ IR-visible sum-frequency generation spectroscopic study," *Electrochemistry Communications*, vol. 12, no. 5, pp. 672-675, 2010.
- [38] X. He, C. Wu, K. Rajagopal, N. Punpongjareorn, and D.S. Yang, "Ordered ionic liquid structure observed at terraced graphite interfaces," *Physical Chemistry Chemical Physics*, vol. 18, no. 5, pp. 3392-3396, 2016.

# Chapter 2

Techniques, Theories, and Data Analysis Parameters

## Chapter 2: Techniques, Theories, and Data Analysis Parameters

In this chapter, the theories of electron diffraction and sum-frequency generation are discussed. In each chapter, more details of the analysis are discussed explicitly related to that experimental data.

### 2.1 Reflection High-Energy Electron Diffraction

One of the most popular and powerful techniques for structural characterization of materials is the diffraction technique. Diffraction techniques can provide various structural information, including the crystal structure, crystal defects, phase, grain size, strain, and order of crystallinity. Based on the crystallinity of the material, the amount of information that can be extracted from the material is different. For example, it is relatively easy to extract the crystal structure of a single crystal by analyzing their diffraction patterns, while for a powder form of the same material, less information can be extracted, even though the diffraction pattern is still unique for that material in its powder form.

For a diffraction pattern to be generated from a crystal, an incident beam (radiation) of the wave with a wavelength smaller than the inner distances of a crystal lattice is required, which is in angstrom or even sub angstrom order. Chronologically, X-rays were the first type of radiation with such a small wavelength for diffraction studies. Max Von Laue, in 1912, reported the first X-ray diffraction pattern [1], and later in 1927 [2], a diffraction pattern of Ni using electron waves was reported by Davison and Germer. This was only possible after de Broglie demonstrated the wave-particle duality of electrons in 1924.

The interaction of electrons and X-rays with materials differentiates them from each other, even though the general principle of diffraction is still applicable for both. Electrons are generally diffracted by the electrostatic potential of the orbital electrons of the specimen and the atomic nuclei. On the other hand, X-rays are mostly diffracted by orbital electrons. As a result, the scattering cross-section of electrons is much larger

( $10^4 - 10^5$  times) than that of X-rays, which means electrons interact more strongly with the material. In practice, it means a high-quality diffraction pattern can be recorded from a tiny volume (up to  $1 \mu\text{m}^3$ ) and in a shorter time than the X-rays. In addition, accelerated electrons have a much smaller wavelength compared to the X-rays (one or two orders of magnitude, i.e.,  $0.025 \text{ \AA}$  for 200 KeV accelerated electrons vs.  $2.5 \text{ \AA}$  for  $\text{Cu(K}\alpha)$ ), which leads to an Ewald sphere with a much larger radius ( $1/\lambda$ ), and results in the observation of more 2-dimensional reciprocal lattice points.

## 2.2 Principle of Electron Diffraction

### 2.2.1 Electron Waves

De Broglie proposed the concept of the wave behavior of electrons in 1924, which says the same as the wave-particle duality behavior of light, other (charged) particles such as electrons also have the wave-particle duality behavior. He proposed a general relation between the energy of a photon and its momentum ( $E = h\nu$ ,  $p = \varepsilon/c$ ), and electron waves also have a relation between their wavelength, energy, and momentum ( $\lambda = h/p$ ).

For a non-relativistic particle, when  $E_k \ll E_0 = m_0c^2$ , the De Broglie wavelength become:

$$\lambda = \frac{h}{\sqrt{2 m_0 E_k}}$$

And for a relativistic particle, when  $E_k \ll E - m_0c^2$ , the De Broglie wavelength become:

$$\lambda = \frac{h}{\sqrt{2 m_0 E_k (1 + \frac{E_k}{2E_0})}}$$

Since the momentum is  $pc = \sqrt{E_k(E_k + 2m_0c^2)}$ . Here,  $m_0$  is the rest mass of the electron,  $c$  is the speed of light in a vacuum, and  $E_k$  is the kinetic energy of mass  $m$  moving with velocity  $v$ ,  $E_k = mv^2/2$ . The

kinetic energy of the accelerated electrons is related to the accelerating voltage by  $E_k = eV$ , where  $e$  is the charge of an electron, and  $V$  is the accelerating voltage.

### 2.2.2 Reciprocal Lattice, Diffraction Laws, and Ewald Sphere

A crystal is defined with an infinite periodic arrangement of lattice points in 3D space. The lattice points can be filled by one atom or a couple of atoms, or molecules. The 3D space can be filled with 14 possible periodic arrangement, which is called Bravais lattices, in which all lattice points are identical and can be defined by a set of vectors in real 3D space as follow:

$$\vec{R} = n_1 \vec{a}_1 + n_2 \vec{a}_2 + n_3 \vec{a}_3$$

Where  $n_1, n_2$ , and  $n_3$  are integer numbers, the  $a$ -vectors are the primitive vectors of a unit cell in three principal crystallographic directions.

On the other hand, the Fourier transform of the periodic vectors of the real space (the Bravais lattices) results in a periodic space ( $k$  space) with primitive vectors which are reciprocally associated with the real space. This second periodic lattice is called the reciprocal lattice of the corresponding real Bravais lattice. The real ( $\vec{a}_i$ ) and reciprocal ( $\vec{b}_i$ ) lattice primitive vectors have the following relations:

$$\vec{b}_i \cdot \vec{a}_j = 2\pi \delta_{ij} \quad \begin{array}{l} \delta_{ij} = 0 \text{ if } i \neq j \\ \delta_{ij} = 1 \text{ if } i = j \end{array}$$

$$\vec{b}_1 = 2\pi \frac{\vec{a}_2 \times \vec{a}_3}{\vec{a}_1 \cdot (\vec{a}_2 \times \vec{a}_3)}$$

$$\vec{b}_2 = 2\pi \frac{\vec{a}_3 \times \vec{a}_1}{\vec{a}_1 \cdot (\vec{a}_2 \times \vec{a}_3)}$$

$$\vec{b}_3 = 2\pi \frac{\vec{a}_1 \times \vec{a}_2}{\vec{a}_1 \cdot (\vec{a}_2 \times \vec{a}_3)}$$

The same as the real space general vector ( $\vec{R}$ ), the reciprocal space is expressed with a combination of three primitive vectors and integer coefficients ( $h k l$ ):

$$\vec{G}_{hkl} = h \vec{b}_1 + k \vec{b}_2 + l \vec{b}_3$$

The diffraction generation process was first explained by Lawrence Bragg and his father in 1913 after they observed only specific incident angles generate a bright spot, which was later called the Bragg spots. The diffraction condition is called Bragg diffraction [3]. This diffraction behavior was explained by considering each crystal lattice to be defined with a set of planes with equal spacings and parallel to each other. When two parallel radiations are scattered off by each of these planes, a path difference is generated, related to the plane spacing ( $d$ ) and the incident angle ( $\theta$ ). As a result, the diffraction spots are generated when the path distance is an integer multiple of the wavelength, which creates a constructive interference of the two beams. This relation is schematically shown in Figure 2-1.

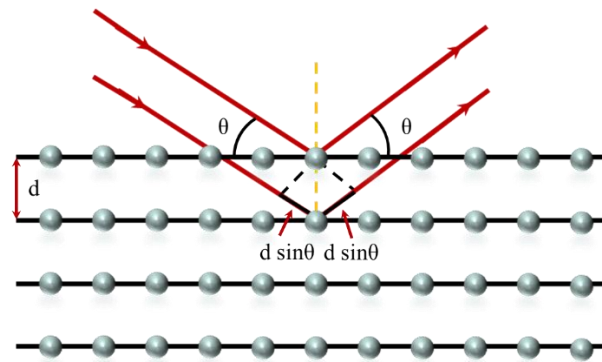


Figure 2-1 A schematic view of Bragg reflection from a set of parallel lattice planes with a distance of  $d$ . The path difference between two incident and reflected beams with the same angles is  $2d \sin\theta$ . Constructive interference happens when this distance is multiple integers of the wavelength reproduced based on reference [4].

On the other hand, Laue formulation, schematically shown in Figure 2-2, is a more general case to explain the diffraction patterns. Each lattice point is defined as a scatterer source, which scatters the incident beam in all directions. In one specific situation, which is when a diffraction maximum is observed, the Laue condition and Bragg condition are similar. The Laue considers each scatterer separately, with the incident and

scattered wave with a magnitude of  $\left|\frac{2\pi}{\lambda}\right|$ . For each set of the incident and scattered vectors with direction normal of  $\vec{n}$ , and  $\vec{n}'$ , from two scatterers separated by  $d$ , the path difference is  $\vec{d} \cdot (\vec{n} - \vec{n}')$ . This path difference for a constructive interference must be an integer multiple of incident wavelength;  $\vec{d} \cdot (\vec{n} - \vec{n}') = m\lambda$ .

By replacing the two scatterers with a Bravais lattice vector  $\vec{R}$ , which as a result the relation between the momentum change of the incident and scattered waves with the reciprocal lattice vector is  $\Delta\vec{k} = \vec{G}_{hkl}$ . This means a constructive interference happens when the momentum vector change is equal to any reciprocal lattice vectors. As a result, based on the Laue condition, the  $\Delta\vec{k}$  vector is perpendicular to the reflecting planes, which results in equal angles for the incident and reflected beams. The planes are equal to the Bragg planes, and the interplanar spacing of the lattice planes satisfies  $|\vec{G}_{hkl}| = \frac{2\pi}{d_{hkl}}$ .

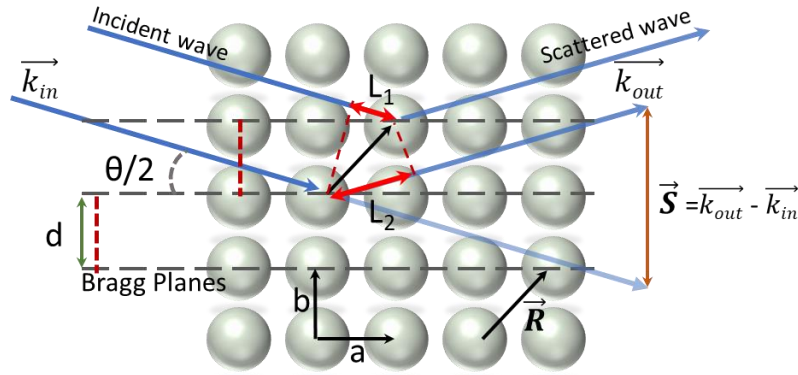


Figure 2-2 Scattering of the two incident waves from two scatterers and a set of parallel planes shows the relation between Laue and Bragg condition reproduced based on reference [4].

The diffraction condition is geometrically explained with the Ewald sphere. As is shown in Figure 2-3, the Ewald sphere is a sphere with its origin at the tip of the electron beam, with a radius of  $\left|\frac{2\pi}{\lambda}\right|$ . For constructive interference, the momentum vector change must be equal to a reciprocal lattice vector, which geometrically means that the Ewald sphere should hit reciprocal lattice points, as shown with red spots in Figure 2-3.

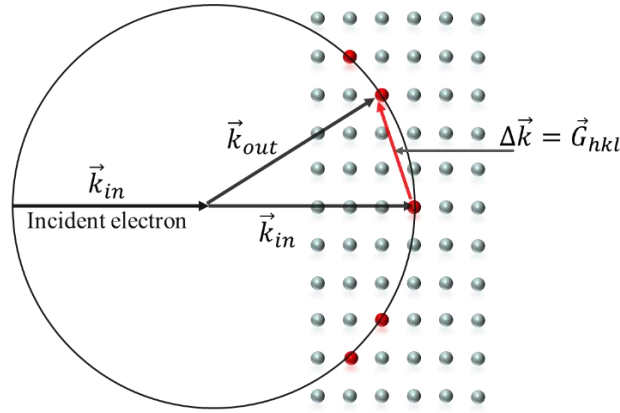


Figure 2-3 Ewald sphere construction and the corresponding reciprocal lattice point that touches the Ewald sphere and satisfies the diffraction condition.

### 2.2.3 Atomic Scattering Factor and Geometrical Structure Factors

The atomic scattering factor is a measure of the scattering amplitude of a wave by an isolated atom, which depends on the type of the atom and the incident radiation. The electron scattering amplitude  $f(k', k)$  is related to the electron atomic scattering factor  $f_{(s)}^{(e)}$ . The structure factor combines the amplitude and the phase of all diffracted waves within a unit cell. The structure factor can be written as

$$F_{hkl} = \sum_j f^{(e)}(s) \exp [2\pi i(hx_j + ky_j + lz_j)]$$

With the sum over all atoms in the unit cell. The intensity of the diffracted electron is directly proportional to the structure factor  $I_{hkl} = |F_{hkl}|^2$ .

### 2.2.4 RHEED Experimental Geometry

RHEED setup consists of an electron gun, a phosphorus screen, and a 5-axis manipulator, shown schematically in Figure 2-4. The main component of the electron gun is the cathode ( $LaB_6$ ) which acts as the electron source. Electrons can be generated with either resistive heating, named “thermal electron,” or photoelectrons by laser radiation. After the generated electrons leave the surface of the crystal, their shape and beam path toward the sample is controlled using a set of electromagnetic lenses. The prepared electrons are then accelerated using the grid voltage.

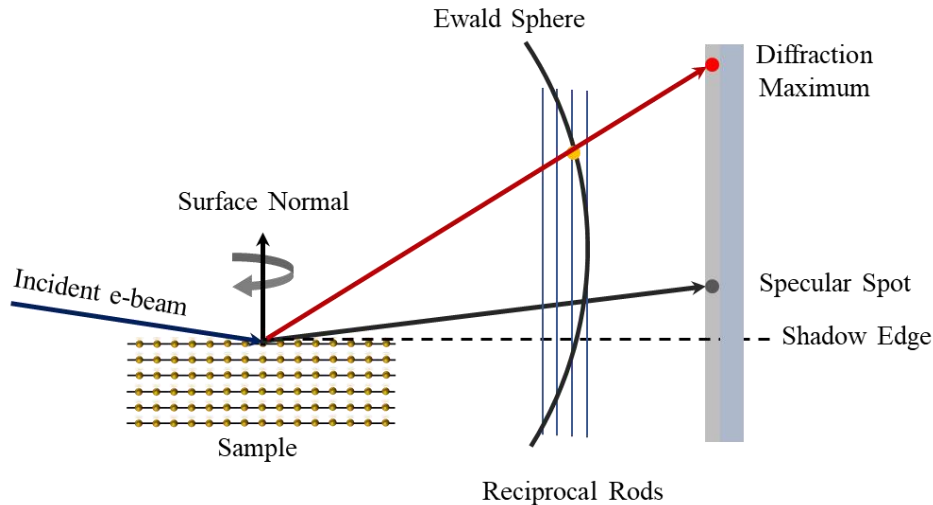


Figure 2-4 Schematic geometry of RHEED. The incident electron on the surface and the diffracted beam on the phosphor screen. The corresponding Ewald sphere and reciprocal rods are involved in the diffraction pattern generation.

The sample heating with a resistive heater up to 500 K, coupled with a cryostat (Janis Research) down to 90 K, provides a wide range for temperature-dependent studies. The incident angle of the electrons on the sample and their azimuthal angles are controllable by the 5-axis goniometer.

### 2.2.5 Examples of RHEED Pattern

In addition to the lattice parameters, other types of information, such as grain size and surface morphology information, can be estimated from the RHEED patterns. The RHEED patterns are generated based on the quality of the sample surface. In 3D-reciprocal space, the reciprocal of a 3D-lattice point of a Bravais lattice is another 3D Bravais. While, in the case of RHEED, one dimension, along the surface normal, is shortened to a few top layers. Because of the reciprocal relations, the corresponding direction in reciprocal space is elongated. The width and intensity modulation along these reciprocal rods convey information about the sample surface [5, 6].

Some of the most common surfaces and their corresponding RHEED pattern are shown in Figure 2-5. For the case of a single crystalline atomically flat surface, the RHEED pattern shows reflection-type

diffraction spots, lie on the Laue zones, with similar intensity, as is shown in Figure 2-5 (a). This is an ideal case, however, in real situations the electrons penetrate in deeper layers, and due to multiple planes involvement along the surface normal, the intensity is usually modulated. If the domain sizes are smaller, the reciprocal spots become reciprocal rods, and a streak-like pattern is observed in their RHEED images, as is shown in Figure 2-5 (d). In the case of a polycrystalline, these small domains are also oriented in all directions, which creates ring-like patterns since the rod-like patterns are now randomly oriented in all directions from the same set of planes resulting in a ring of a specific diameter. Each ring also conveys information about a specific set of lattice planes. A radial averaging of the diffraction intensity of the rings is required to extract the scattering vector of each ring. The last type is the surfaces with 3D islands, which the high-energy electrons penetrate the islands, and the diffraction pattern is a transmission-like pattern, as is shown in Figure 2-5 (b).

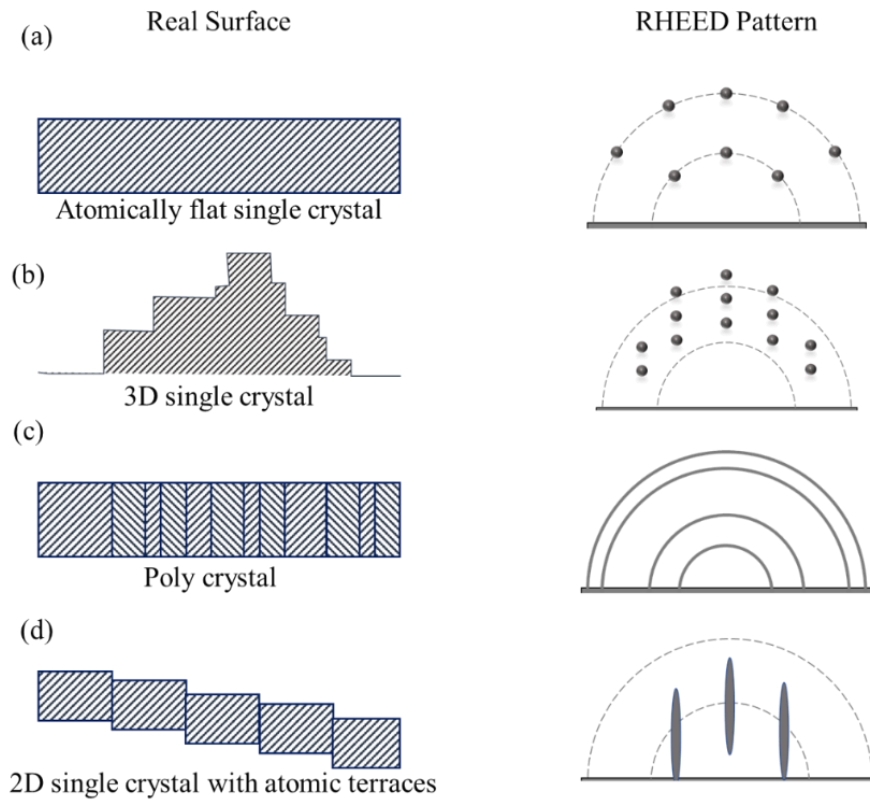


Figure 2-5 Four different types of surfaces and their general diffraction features in RHEED patterns [6].

### 2.2.6 Rocking Curve

In addition to the azimuthal information, by rotating the sample around the surface normal, as is schematically shown in Figure 2-4, the third dimension of the sample is probed by increasing the incident angle of the electron beam, from grazing angle to higher angles ( $4^\circ - 5^\circ$ ). Since the RHEED patterns generated at grazing incidence angle usually do not convey information about the vertical ordering of the sample, following the Bragg spots along the surface normal by increasing the incidence angle, called the RHEED rocking curve, is informative about the vertical ordering. The process is shown in Figure 2-6, from the RHEED pattern (on the left) to the rocking curve (on the right).

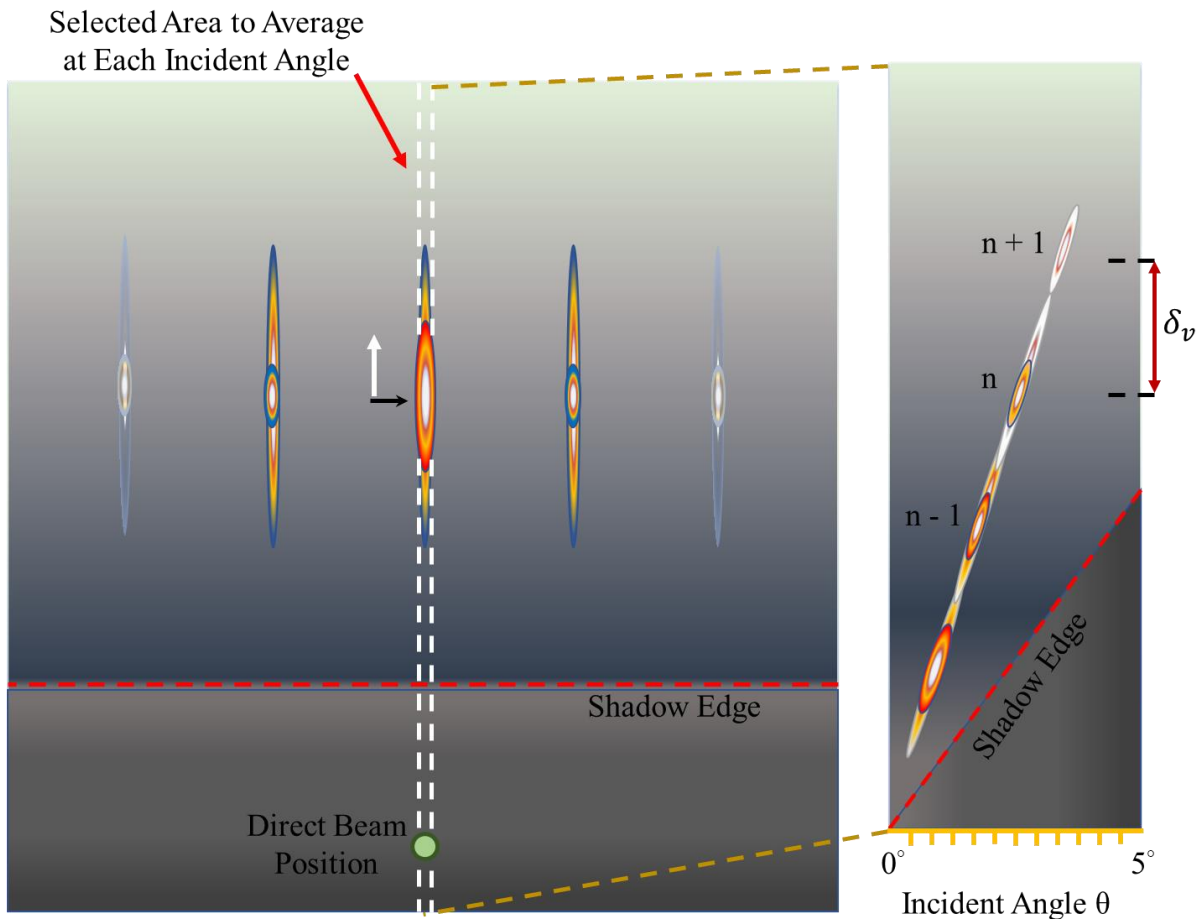


Figure 2-6 Schematic RHEED pattern at one specific angle, the middle streak, and the selected area to create the rocking curve. On the right side, three consecutive diffraction orders are shown, and the vertical spacing shown by  $\delta_v$ .

The RHEED patterns are recorded as a function of the incidence angle. Increasing the incidence angle causes the electrons to penetrate more in the sample, and as a result, higher orders of diffraction spots are recorded. As it is shown in Figure 2-6 (left), the middle streak is selected and averaged, following along the surface normal (white arrow), and adding up to create an image of the intensity (y-axis) vs. incidence angle (x-axis), shown on the right. The scattering vector is then the distance from reciprocal space to the direct beam and is calculated by  $S = \frac{R}{L\lambda}$ , with  $\lambda = 0.07 \text{ \AA}$  for 30 keV electrons, R is the distance to the direct beam, and L is the camera length. The real-space distance (d) is then calculated by  $d = \frac{1}{S}$ .

### 2.2.7 Mean Free Path and Electron Penetration Depth

For a given electron energy and a material, the probing depth depends on the incidence angle and the mean free path of the electron beam. In the case of the single elastic scattering, the electron penetration depth is calculated by  $\zeta_e \cong l_e \sin\theta$ , with  $l_e$  being the mean free path, and  $\theta$  the incidence angle. The mean free path itself is calculated by  $l_e = \frac{1}{\sigma N}$ , with  $\sigma$  being the total cross-section of scattering and N the density of scatterers. Generally, heavier atoms have a higher scattering cross-section, low mean free path, and low penetration depth compared to lighter atoms.

## 2.3 Sum Frequency Generation Spectroscopy

### 2.3.1 Theory

When molecules interact with an electric field, the molecular vibrational response to the field is linear for a weak electric field, while it is nonlinear in the case of the strong electric field, such as the fields generated by strong pulsed laser fields. The linear response has an induced dipole of  $\mu = \mu^0 + \alpha E$ , which  $\mu^0$  is the permanent dipole of the molecule [7-9], related to the localized electron distribution around an atom or a functional group, and  $\alpha$  is the polarizability of the molecule. On the other hand, the molecular response to an

intense field is nonlinear, and higher orders of the molecular polarizabilities are involved in the induced dipole.

So, the induced dipole is then rewritten as

$$\mu = \mu^0 + \alpha E + \beta : EE + \gamma : EEE + \dots$$

$\beta$  and  $\gamma$  are the second-order and third-order hyperpolarizabilities. The polarization (P) of a system can be written as the sum of all orders of the polarizations as

$$P = P^{(1)} + P^{(2)} + P^{(3)} + \dots$$

$$P = \varepsilon_0 \chi^{(1)} E + \varepsilon_0 \chi^{(2)} : EE + \varepsilon_0 \chi^{(3)} : EEE + \dots$$

Which as a result

$$P^{(2)} = \chi^{(2)} : EE$$

$\chi^{(2)}$  is the second-order susceptibility tensor.

Sum frequency generation (SFG) is a second-order nonlinear optical process that happens when two laser beams spatially and temporally overlap on a sample [7, 8, 10]. As a result, a third beam is generated with its energy as the sum of the two input beams. Typically, for a vibrational SFG experiment, the two input laser beams are a tunable mid-IR beam ( $2000 \text{ cm}^{-1} - 4000 \text{ cm}^{-1}$ ) and a fixed visible laser (532 nm). From the conservation of energy, the energy of the SFG photon is  $\omega_{SF} = \omega_{VIS} + \omega_{IR}$ , where  $\omega_{SF}$ ,  $\omega_{VIS}$ , and  $\omega_{IR}$  are the frequency of the output beam, the visible and the IR beams, respectively.

In addition, the parallel components of the momentum vectors are conserved, leading to

$$\vec{k}_{||,SF} = \vec{k}_{||,VIS} + \vec{k}_{||,IR}$$

$$n_{SF} \omega_{SF} \sin(\theta_{SFG}) = n_1 \omega_1 \sin(\theta_1) + n_2 \omega_2 \sin(\theta_2)$$

where  $\vec{k}_{||}$  is the parallel component of a wave vector,  $n$  represent refractive indices, and  $\theta$  represent the angle of incidence or emission for the three beams involved in the SFG process [11-16]. This process and the geometry of the SFG beams are shown in Figure 2-7.

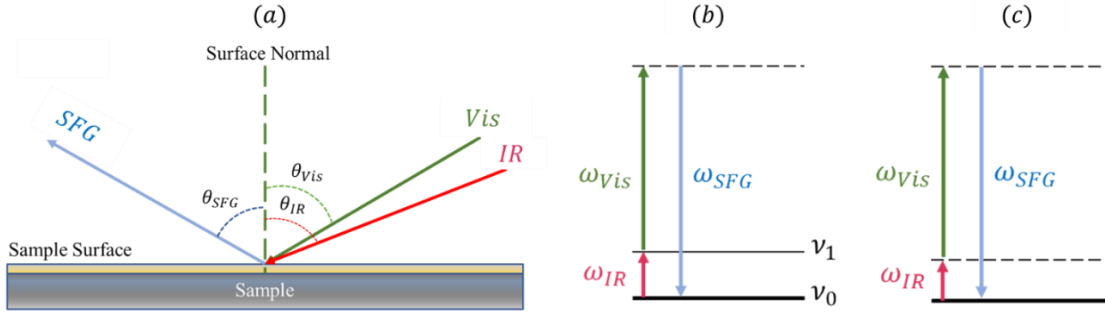


Figure 2-7 Schematic description of the SFG setup and SFG process. (a) The two input lasers, the SFG output, and the angles of each vs. surface normal, (b) Energy levels for a resonant SFG process, and (c) Non-resonant SFG process. Dashed lines represent a non-stationary (virtual) energy level, and solid lines represent stationary energy levels.

According to the following relation between the two incident laser beams and the second-order polarization, which is the case for SFG process, in a centrosymmetric media, due to an inversion symmetry,  $\chi^{(2)} = 0$ , therefore, SFG process is a surface/interface specific process in a centrosymmetric media.

$$P^{(2)} = \chi^{(2)} : EE$$

$$-P^{(2)} = \chi^{(2)} : (-E_1)(-E_2)$$

$$-P^{(2)} = \chi^{(2)} : E_1E_2 = P^{(2)}$$

The oscillating polarization leads to the generation of the SFG electromagnetic wave, and the intensity of the SF field is proportional to the square of the two input electric fields by

$$I_{SF} \propto |P^{(2)}|^2 = |\chi^{(2)} : E_1E_2|^2$$

To describe the process with energy levels, see Figure 2-7 (a) and (b), the two input fields change the state of the material from a ground state to a virtual state and emit an SF photon as it goes back to the ground state. If a stationary intermediate energy level is involved in this process, such as a vibrationally excited state, the process becomes resonant-enhanced, and the SF intensity increases.

$$\chi^{(2)} = \chi_{NR}^{(2)} + \chi_{res}^{(2)}$$

$$\chi_R^{(2)} = \sum_q \frac{Aq}{\omega_{IR} - \omega_q - i\Gamma_q}$$

$$A_q = N \langle \beta^{(2)} \rangle$$

In these equations, I denote the intensity of the SFG beam,  $\chi^{(2)}$  is the second-order nonlinear susceptibility tensor,  $\omega_q$  is the frequency of normal mode of vibration,  $\omega_{IR}$  and  $\omega_{vis}$  are the frequencies of IR and visible beams. In addition,  $A_q$  and  $\Gamma_q$  are the amplitude and the linewidth of the normal vibrational mode. The numberer of molecular modes contributing to the vibration are shown with N, and  $\beta^{(2)}$  is the hyperpolarizability, which is the average of all possible molecular orientations (shown with  $\langle \rangle$ ). To extract the molecular information of the molecules at the surface, different polarization configurations of the three laser beams must be selected, which results in the selection of different components of the susceptibility tensor. The macroscopic nonlinear susceptibility and the microscopic hyperpolarizability of the surface molecules are then related to each other by

$$\chi_{ijk}^{(2)} = N_s \sum_{i'j'k'} \langle R_{ii'} R_{jj'} R_{kk'} \rangle \beta_{i'j'k'}$$

The magnitude of the second-order susceptibility is sensitive to the degree of polar orientation of the molecule at the surface. The s- and p-polarized fields are schematically shown in Figure 2-8, which shows the p-polarized light probes the x and z component, while the s-polarized probes only the y components.

### 2.3.2 Instrumental Setup

The SFG setup consists of six main components, including Nd:YAG laser, optical parametric generator/amplifier (OPG/OPA), sets of waveplates and polarizers, monochromator/detector, Boxcar/computer programs. A 1064 nm fundamental beam generated from the laser passes through the OPG/OPA setup, converting the fundamental beam to a fixed 532 nm and a tunable IR beam. The two newly generated beams leave the OPG/OPA setup, passes through mirrors, waveplates, and polarizers to adjust the polarization, size, and intensity of the laser beams before reaching the sample. The generated SFG is filtered with a monochromator and passes through a photomultiplier tube (PMT) and a boxcar to intensify the signal

and average the outputs before sending it to the computer through a data acquisition device (DAQ) for further analysis.

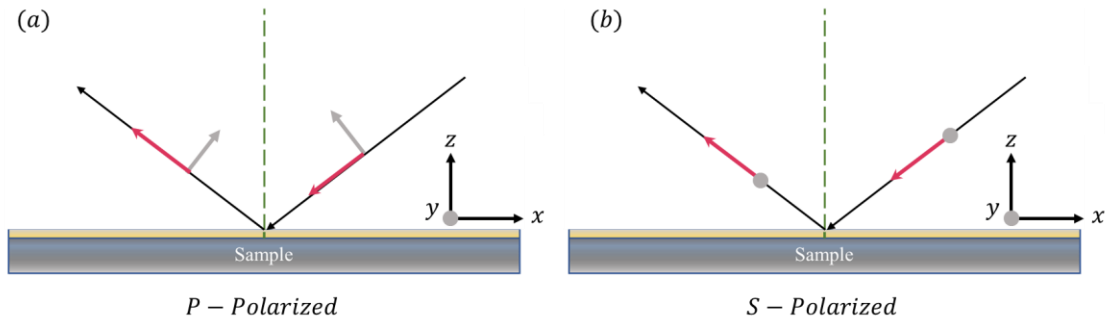


Figure 2-8 Schematic view of a polarized light (a) P-polarized light, which contains information of both the x and z axes. (b) S-polarized light only probes y components. The red arrows show the direction of the light, and the gray arrows show the polarization. The gray circle is arrows perpendicular to the x-z plane.

The Outline of the laser is shown in Figure 2-9, for a 1064 nm EKSPELA PL2251, 21 ps pulses at 20 Hz. The laser consists of three main components; a master oscillator, a regenerative amplifier, and a power amplifier [17]. The fundamental 1064 nm pulsed laser is produced by the master oscillator, which then the generated beam seeds the regenerative amplifier, where the pumped Nd:YAG diode amplifies the pulse power for a few cycles. Then, the pulse enters the third stage, where the flash-lamp pumped Nd:YAG rod amplifies the laser in final step, and sends the output to OPG/OPA setup [18].

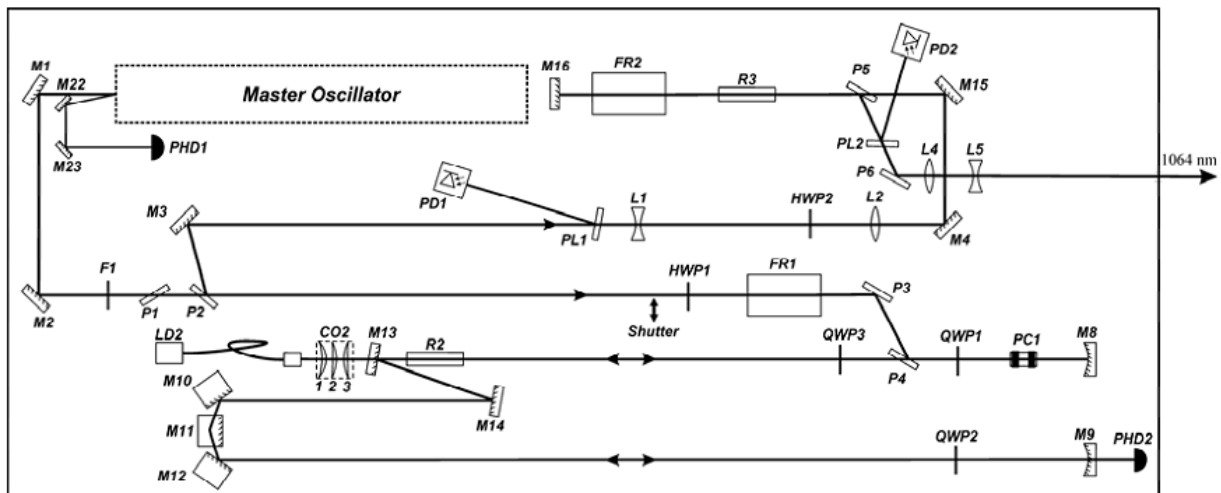


Figure 2-9 Schematic of the ESKPLA laser [17]

The output 1064 nm beam from the laser is split by beam splitter BS1. 90 % is then sent to the OPG/OPA, which is split again with BS2; one portion is then frequency-doubled to create the 532 nm, which itself is also split by BS3, one beam and sent to the sample, and the other is used to pump KTP crystals 1 and 2. The other part of the beam is sent to OPA. Finally, the output is mixed with the remaining of the initial 1064 nm beam to generate the mid-IR wavelength in the OPA stage by KTA crystals 3 and 4. The tunable IR wavelength is controlled by turning the four crystals relatively and generating a 2000 cm<sup>-1</sup> to 4000 cm<sup>-1</sup> IR field.

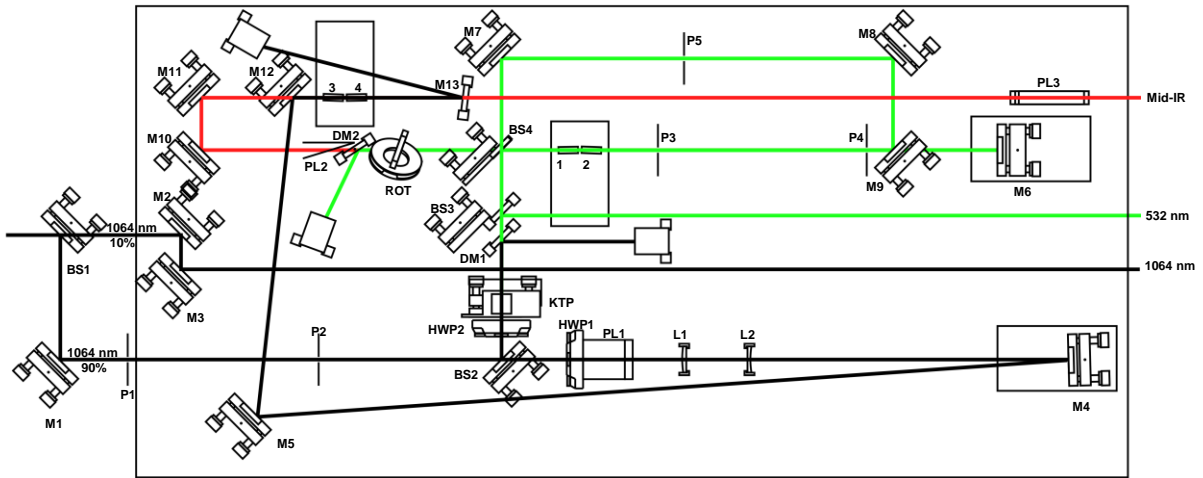


Figure 2-10 OPG/OPA schematic outline, from refrence [19]

### 2.3.3 SFG Spectra Fitting

The SFG signal is usually scanned more than one time, in the desired wavelength range, to improve the final spectrum after averaging the SFG spectra and normalizing them. The averaged and normalized SFG spectra are then fitted to

$$\chi^{(2)} = \chi_{NR}^{(2)} + \chi_{res}^{(2)}$$

$$\chi_R^{(2)} = \sum_q \frac{Aq}{\omega_{IR} - \omega_q - i\Gamma_q}$$

The intensity of each resonance is then calculated by dividing the amplitude by the peak width according to

$$I_{SFG} = \left(\frac{A}{\Gamma}\right)^2$$

If the Fermi resonance of a mode is also present, since it is the overtone of the fundamental mode, the intensity of that must be added to the fundamental mode when the intensity of two modes, such as symmetric methyl stretch and antisymmetric methyl stretch, are compared, which means

$$I = \left(\frac{A_S}{\Gamma_S} + \frac{A_{FR}}{\Gamma_{FR}}\right)^2$$

## 2.4 Conclusion

The basic theory of RHEED and SFG and their experimental parameters were discussed in this chapter. Data acquisition and analysis are discussed in each chapter for the specific situation and the specific sample under study.

## 2.5 Bibliography

- [1] M. De Graef, Introduction to Conventional Transmission Electron Microscopy. Cambridge University Press, 2003.
- [2] C. J. Davisson and L. H. Germer, "Reflection of electrons by a crystal of nickel," Proceedings of the National Academy of Sciences of the United States of America, vol. 14, no. 4, p. 317, 1928.
- [3] W. H. Bragg, W. L. Bragg, and P. Character, "The reflection of X-rays by crystals," Proceedings of the Royal Society of London. Series A, Containing Papers of a Mathematical and Physical Character, vol. 88, no. 605, pp. 428-438, 1913.
- [4] N. W. Ashcroft and N. D. Mermin, Solid-State Physics, Rinehart and Winston, New York London, 1976.
- [5] A. Ichimiya, P. I. Cohen, and P. I. Cohen, Reflection High-Energy Electron Diffraction. Cambridge University Press, 2004.
- [6] S. J. Hasegawa, "Reflection high-energy electron diffraction," Characterization of Materials, vol. 97, pp. 1925-1938, 2012.
- [7] C. D. Bain, "Sum-frequency vibrational spectroscopy of the solid/liquid interface," Journal of the Chemical Society, Faraday Transactions, vol. 91, no. 9, pp. 1281-1296, 1995.
- [8] D. C. Duffy, P. B. Davies, and C. D. Bain, "Surface vibrational spectroscopy of organic counterions bound to a surfactant monolayer," The Journal of Physical Chemistry, vol. 99, no. 41, pp. 15241-15246, 1995.
- [9] A. G. Lambert, P. B. Davies, and D. J. Neivandt, "Implementing the theory of sum-frequency generation vibrational spectroscopy: A tutorial review," Applied Spectroscopy Reviews, vol. 40, no. 2, pp. 103-145, 2005.
- [10] M. Buck, M. Himmelhaus, "Vibrational spectroscopy of interfaces by infrared-visible sum-frequency generation," Journal of Vacuum Science & Technology A: Vacuum, Surfaces, and Films, vol. 19, no. 6, pp. 2717-2736, 2001.
- [11] Y. R. Shen, "Surfaces probed by nonlinear optics," Surface Science, vol. 299, pp. 551-562, 1994.
- [12] Y. R. Shen "Surface nonlinear optics: a historical perspective." *IEEE Journal of Selected Topics in Quantum Electronics*. 2000 Nov; 6 (6):1375-9.
- [13] K. Sun, M. Lan, and J. Z. Wang, "Absolute configuration and chiral self-assembly of rubrene on Bi (111)," Physical Chemistry Chemical Physics, vol. 17, no. 39, pp. 26220-4, Oct 21, 2015.
- [14] H.F. Wang, L. Velarde, W. Gan, and L. Fu, "Quantitative sum-frequency generation vibrational spectroscopy of molecular surfaces and interfaces: line shape, polarization, and orientation," Annual Review of Physical Chemistry, vol. 66, no. 1, pp. 189-216, 2015/04/01 2015.

- [15] P. Vancsó, G. Z. Magda, J. Peto, J. Y. Noh, Y. -S. Kim, C. Hwang, L. P. Biro, L. Tapasztó, "The intrinsic defect structure of exfoliated MoS<sub>2</sub> single layers revealed by scanning tunneling microscopy," Scientific Reports, Article vol. 6, p. 29726, 2016.
- [16] H.F. Wang, "Sum frequency generation vibrational spectroscopy (SFG-VS) for complex molecular surfaces and interfaces: Spectral line shape measurement and analysis plus some controversial issues," Progress in Surface Science, vol. 91, no. 4, pp. 155-182, 2016.
- [17] M. Seah, "A review of the analysis of surfaces and thin films by AES and XPS," Vacuum, vol. 34, no. 3-4, pp. 463-478, 1984.
- [18] W. Koechner, Solid-State Laser Engineering. Springer, 2013.
- [19] A. A. Pikalov, "Sum frequency generation imaging microscopy: factor analysis of mixed monolayers," (Doctoral Dissertation), 2019.

# Chapter 3

Ordered – Disordered Structural Transition  
of Ionic Liquid at Highly Oriented  
Pyrolytic Graphite (HOPG)

## Chapter 3: Ordered-Disordered Structural Transition of Ionic

### Liquid on Highly Oriented Pyrolytic Graphite (HOPG)

#### 3.1 Introduction

Ionic liquids (ILs), which are molten salts comprised only of anions and cations, are an attractive class of materials with both industrial and scientific interest [1]. Some of the common cations and anions in IL studies are shown in Figure 3-1. In general, ionic liquids are categorized as molten salts with melting points below 100 °C. Usually, due to their low charge density and low molecular symmetry, ILs do not form stable crystal lattices, which as a result, lowers their melting points compare to classical molten salts [1, 2].

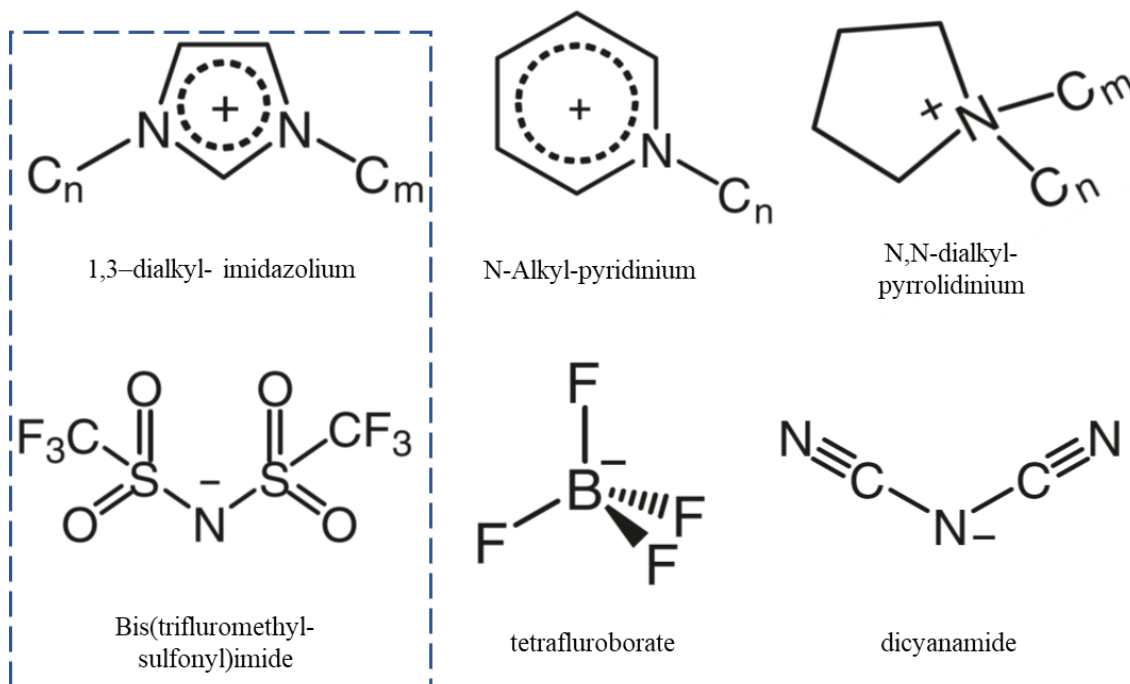


Figure 3-1 Selected cations and anions composing the most common ionic liquids.

Due to the unique physio-chemical properties of the ILs, including their low vapor pressure, high thermal stability, wide electrical window, solvation properties, and tunable physio-chemical properties [3-8], they have been used in many applications, such as catalysis, green chemistry, fuel cells, electrochemistry,

lubrication, separation, and corrosion [3, 7, 9-14]. The importance of the IL interfacial structures is evident from the abovementioned applications and processes and requires detailed understanding to improve their efficiency, mainly in IL-gas (or IL-vacuum) and IL-solid interfaces.

Because of the low vapor pressure of the ILs, it is possible to perform experiments on a fundamental level to understand their structures in an ultra-clean (ultra-high vacuum (UHV)) environment as a model system. It was also shown that due to the similar property of the ILs, and their high thermal stability, it is possible to deposit thin films of ionic liquids using the physical vapor deposition (PVD) technique [4]. Since the IL thin films have a wide range of applications, such as lubrication, and heterogenous catalysis., thin-film deposition with PVD provides the advantage of studying their interfacial structure in a thickness-dependent approach and nanometer-level control.

Variety of techniques has been used to study the surface/interface structures of the ionic liquids on solid substrates, including sum-frequency generation (SFG) spectroscopy [15-17], X-ray photoelectron spectroscopy (XPS) [5, 18-21], scanning tunneling microscopy (STM) [22, 23], atomic force microscopy (AFM) [24, 25], and reflection high-energy electron diffraction. [4, 26-40]. From these studies, layered ordering of some ionic liquids has been reported on different substrates. Including checkerboard structure for  $[C_1C_1Im][Tf_2N]$  (= 1,3-dimethyl imidazolium bis(trifluoromethyl)imide) and  $[C_8C_1Im][Tf_2N]$  (= 1-methyl-3-octylimidazolium bis(trifluoromethyl)imide) on Au (111) with both the anion and cation in contact with the substrate and double layers structure of  $[C_1C_1Im][Tf_2N]$  thin films on glass with the cation in contact with the glass and the anion at the vacuum side. Also, it was shown that the ILs on Au (111) were formed in a layer-by-layer mode up to a specific thickness. However, it was a double-layer in the first step and a 3D-island growth for the next layers in the case of the IL/glass. Preferential arrangements of the ions at the IL-gas interface can affect the mass transport properties at the interface. In addition, other properties like surface wetting or the ion arrangement at the interface can be influenced at the IL-solid interfaces. Each of the

abovementioned properties is of major components of many applications such as “Supported Ionic Liquid Phase” (SILP) [41], which is a porous inert system coated by IL layer to dissolve catalysts in it. As a result, due to the differences in solubility and mass transport of different designed systems, it is possible to enhance some interactions of interest.

Thin-film preparation of ILs has been reported using dip-coating, spin-coating, laser deposition, electrospray ionization deposition, and physical vapor deposition [42-48]. However, the physical vapor deposition method brought the capability of highly controlled thickness-dependent studies in sub-monolayers to study the growth mechanism of the IL thin films in more detail. Unfortunately, in all the techniques used for this purpose, the extracted information is either for both the IL-gas (IL-vacuum) and the IL-solid interface or from one interface only. There is no unique method capable of studying both sides of the IL films separately.

It is shown in this chapter; the IL thin films show a thickness-dependent crystallinity on a solid substrate, which has a transition from a crystal state to an amorphous state after a specific range of thickness (which is different for different ILs). This scenario is only valid for some ILs which crystallize on a solid substrate. In this work, the importance of combining different techniques to address this phenomenon in more detail was discussed, and a future direction to further study the crystal-amorphous transition is explained. The thickness-dependent structure of 1-ethyl-3-methylimidazolium bis(fluorosulfonyl)imide [EMIM][FSA] IL thin films on the highly oriented pyrolytic graphite (HOPG) is reported for the first time, and the most likely crystal structure of [EMIM][FSA] is predicted.

Even though the structure of [EMIM][FSA] IL has never been reported, its similarity to the well-studied [EMIM][TFSA], shown in Figure 3-2, is the primary reference to investigate the structural properties of these ILs in this chapter. The imidazolium cations contain an aromatic ring, where the positive charge is delocalized. As a result, a low average charge density is achieved, which is one of the main reasons a stable

crystal lattice is not created for most ILs due to multiple possibilities for low energy conformations. Furthermore, the positive charge is not usually extended toward the alkyl chain attached to the nitrogen atom of the aromatic ring, which results in a relatively neutral part. Generally, three main intermolecular interactions for the imidazolium-based ILs can be defined: long-range Coulombic interactions, plus dispersive and hydrogen-bonding interactions. In addition, the [TFSA] and [FSA] anion are chemically relatively similar to each other, with a difference of the CF<sub>3</sub> group and F atom on two sides of the molecules. The negative charge distribution is relatively uniform in the anions. However, the CF<sub>3</sub> groups have an electron-withdrawing effect and cause a steric effect by hindering access to the [SNS<sup>-</sup>] part [6, 49]. In addition, ILs, based on [TFSA] anion, are generally chemically inert, hydrophobic, and thermally stable. The similarity of the two ILs and application studies on [EMIM][FSA] IL are the main motivations to study this IL for further understanding its structural behavior.

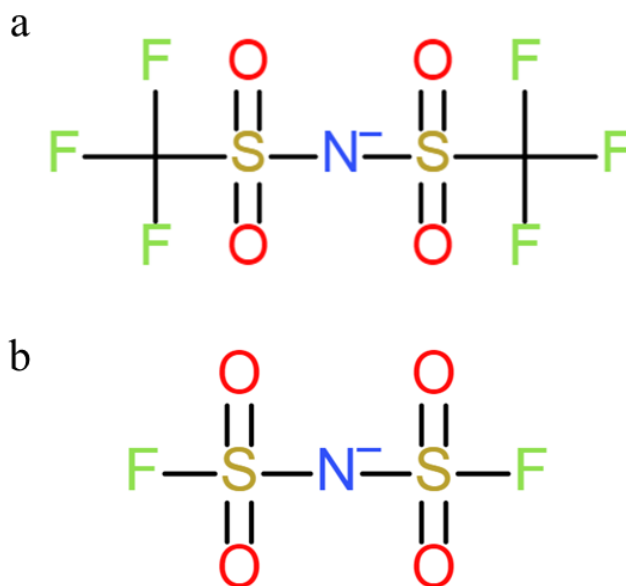


Figure 3-2 The two anions are mainly discussed in this chapter. (a) The [TFSA] anion, well-studied with imidazolium-based cations. (b) [FSA] anion is used in many applications, but no structural studies have been reported.

## 3.2 Experimental

### 3.2.1 Ultrahigh Vacuum System

The Ultrahigh vacuum (UHV) system consists of three main chambers:

- I Diffraction chamber, with an electron gun, a phosphor screen, and a 5-axis goniometer
- II Load-lock chamber, with three sample storages, and thermal annealing stage for sample preparation
- III Deposition chamber for IL thin film preparation

A gate valve separates each chamber to isolate each chamber during different steps of an experiment. Sample cooling is possible down to 90 K using liquid nitrogen flow in a cryostat (Janis Research) connected to the goniometer (McAllister Technical Services) with a braided copper. The temperature measurement is possible with a K-type thermocouple in direct contact with the sample surface. A resistive heater mounted in the cryostat enables the temperature control of 90 K to 500 K with a precision of 0.1 K on the copper sample holder and  $< 1$  K on the sample surface.

The electron beam generation is possible from the cathode (a  $\text{LaB}_6$  crystal, the electron source), either continuously in thermal mode, by resistive heating the cathode, or in pulsed mode, by focusing the pulsed laser beam (257.5 nm) at the tip of the crystal (due to the photoelectric effect). Two quadrupoles and octupoles sets optimize the shape of the generated electron beam. The electrons are accelerated (with a kinetic energy of 30 KeV) with grid voltage inside the electron gun. For static measurements, i.e., IL crystallization, the electron beam is focused on the screen with a horizontal full-width half maximum of  $\sim 150$   $\mu\text{m}$ . The incident angle ( $0^\circ - 5^\circ$ ) of the electron beam with respect to the sample surface is controlled by rotating the sample (goniometer). The resulting diffraction pattern is then imaged on the phosphor screen using a CMOS camera. The photon intensity is intensified by a micro-channel plate (MCP) before imaging, and the diffraction patterns are collected and stored in a computer for further analysis.

### 3.2.2 Ionic Liquid Thin Film Deposition

Deposition of the IL thin films was performed in the IL chamber, which is equipped with an effusion cell (SVT associates) for physical vapor deposition (PVD) of the IL, and a quartz microbalance (QCM) to monitor the film thickness. The effusion is assembled on a linear actuator with a top-down geometry to change the distance of the IL source from the substrate. The crucible containing the IL is also equipped with a heating element for deposition at elevated temperatures. Before deposition, the empty crucible is degassed at temperatures over 670 K (~ 400 °C). The IL is then loaded in the crucible (10 ml capacity, made of graphite) in a nitrogen-filled glovebox. The crucible is assembled within 5 min on the effusion cell, and the IL chamber is pumped down slowly to prevent sudden degassing of the trapped gases in the IL, which causes the IL to spill out of the crucible. In the next step, the IL is dried at room temperature for a couple of days, then degassed two or three times at a temperature of 105 °C – 110 °C for several hours. Finally, the IL chamber is pumped down to the pressure of  $7 \times 10^{-10}$  torr, using a set of a turbopump (PFEIFFER Vacuum) and an oil-sealed rotary pump (Leybold GmbH). In this study, an ultrapure ionic liquid, 1-ethyl-3-methylimidazolium bis(fluorosulfonyl)amide ([EMIM][FSA]) (Some properties are shown in Table 3-1), with a halide concentration below 50 ppm was loaded into the crucible, in a glovebox, under nitrogen environment. It was treated following the abovementioned procedure to prepare the IL for deposition.

The distance of the IL source and the evaporation temperature are two variables involved in controlling the film thickness. Furthermore, the flux density  $J$  (molecules  $\text{cm}^{-2} \text{s}^{-1}$ ) is related to the geometrical parameters of the effusion cell and the molecular mass of the IL with equation 3-1.

$$J = 4.62 \times 10^{22} \frac{pr^2}{L^2(MT)^{1/2}} \quad 3-1$$

In this equation,  $r$  is the effusion cell radius,  $p$  is the vapor pressure in mbar, and  $M$  is the molecular mass of the IL, and  $L$  is the distance to the source. In equation 3-1, the flux density change is smaller with

temperature compared to the pressure. As a result, flux density changes exponentially with the temperature of the IL source.

Table 3-1 Some of the properties of EMIM FSA IL

Properties		
EMIM FSA	Melting Point	-13 °C
	Density	1.39
	Viscosity	24.5 cP at 25°C
	Molar Mass	291.3 g/mol
	Decomposition Temperature	307°C
	Cation	1-Ethyl-3-methylimidazolium
	Anion	bis(fluorosulfonyl)imide
	Property	Hydrophobic

The quartz microbalance (QCM, Nor-Cal Products Inc.) is sensitive to small changes in mass ( $\Delta m$ ), which as a result leads to frequency change ( $\Delta f$ ) of the gold-coated quartz crystal, which resonates at 6 MHz. The relation between  $\Delta f$  and  $\Delta m$  is described by the Sauerbrey equation [50].

$$\Delta f = C \times \Delta m \tag{3-2}$$

$$C = - \frac{2f_0^2}{A_q(\rho_q\mu_q)^{\frac{1}{2}}}$$

Where  $f_0$  is the resonance frequency (in Hz) of the fundamental mode of quartz crystal,  $\rho_q$  is the density of quartz (2.648 g/cm<sup>3</sup>),  $\mu_q$  is the shear modulus of the quartz (2.947 × 10<sup>11</sup> g.cm<sup>-1</sup>.s<sup>-2</sup>), and  $A_q$  is the active crystal area between two electrodes (cm<sup>2</sup>). The deposition rate of the IL was controlled with the deposition temperature (383 K to 413 K) and the relative distance of the deposition source (crucible) and the substrate. Ultrathin ionic liquid films were deposited on highly oriented pyrolytic graphite (HOPG) with different film thicknesses, which was achieved by controlling the deposition time. The rate was monitored before, after, and in the middle of deposition to better estimate the film thickness. For thicker films above 10 nm, the rate was

monitored every 10 min and averaged at the end for a more accurate thickness estimation. The partial pressure of the parents and the fragments of the ions was monitored using a residual gas analyzer (RGA,  $m/z \leq 200$ ) to confirm the deposition of both the cation and the anion [51].

### 3.2.3 RHEED Experiment

The diffraction patterns of the IL-HOPG interfacial structures at different IL film thicknesses were recorded in reflection geometry at grazing incidence angles. Electrons accelerated by a voltage of  $\sim 30$  KV result in a de Broglie wavelength ( $\lambda$ ) of  $\approx 0.07$  Å. The average electron flux was maintained lower than 1 pA/mm<sup>2</sup> to prevent sample damage with electrons during the experiment. No sign of sample damage was seen during any sets of diffraction patterns. The elastic mean-free path length of 30 KV electrons in the IL is  $\approx 57$  nm. Therefore, a probe depth of  $\approx 0.5$  nm - 5 nm is obtained at the grazing incident angle range of 0.5 to 5 degrees, which means more probing of the topmost layer of the IL. The mean-free-path and penetration depth of the elastically scattered electrons are shown in Table 3-2. Since the cell volume of the [EMIM][FSA] is unknown, it is assumed that the penetration depths of both ILs are close to each other.

Table 3-2 Mean-free path and penetration depths of electron for elastic scattering condition at 30 keV

Material	Cell Volume	$l_e$ (Å)	$\delta_p$ (Å)	$\theta$
EMIM TFSA	3072	570	9.9	1°
			19.9	2°
			29.8	3°
			39.7	4°
HOPG	35	2750	48	1°
			192	4°

## 3.3 Results and Discussion

### 3.3.1 Room Temperature Structure of the IL on HOPG

Diffraction image of the HOPG substrate and the as-deposited IL on HOPG is shown in Figure 3-3 (a and c) before and after IL deposition. The HOPG surface is recovered after the IL deposition by desorbing

the IL at elevated temperatures ( $> 400$  K). It was also found that the IL thin film on the HOPG substrate only shows a diffuse scattering pattern (Figure 3-3 (b)) at room temperature, with no sign of crystallization. As a result, the IL at room temperature does not have a long-range vertical and horizontal ordering of the cations and the anions. In other words, ions of the IL are organized in a “liquid-like” organization at room temperature without any long-range periodicity compared to a crystal and a polycrystalline case. Furthermore, the middle streak of the HOPG does not disappear (Figure 3-3 (b)) for the first two films (with a nominal thickness of 1.4 nm and 2.4 nm) at low incidence angles (almost 1 degree). However, for the 3.2 nm film and higher thicknesses, only the diffuse background is imaged at room temperature, which is in good agreement with the penetration depth calculated in Table 3-2.

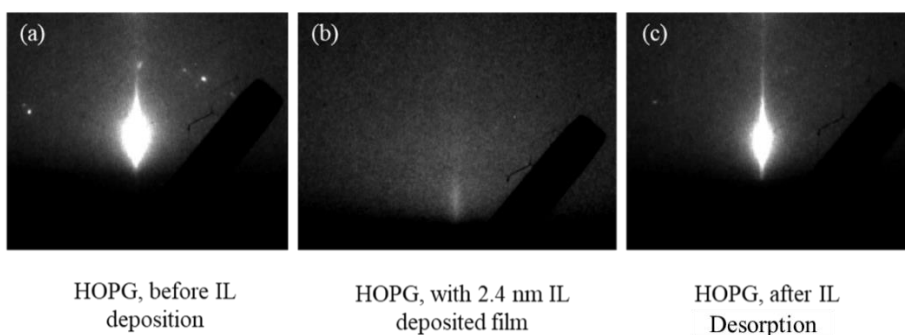


Figure 3-3 RHEED images of (a) HOPG before IL deposition (b) As-deposited IL on HOPG (c) HOPG after desorbing the IL at elevated temperatures

The same results were recorded at room temperature for all other deposited ILs with different nominal film thicknesses, from 1 nm to 21 nm, examined in this experiment. In this experiment, film thicknesses deposited on HOPG are 1.4 nm, 2.4 nm, 3.2 nm, 6 nm, 14 nm, 18 nm, and 21 nm. The HOPG was also scanned along the Z direction (shown in Figure 3-4), which shows the middle streak (sample is atomically flat), without apparent side streaks, due to the small domain sizes of the substrate. Generally, the sample surface is atomically flat where the sample is probed. The Z-scan is shown in Figure 3-7 schematically, which is perpendicular to the electron beam direction. The other direction aligned with the electron beam and perpendicular to the Z-direction is called X-scan, hereafter in this thesis.

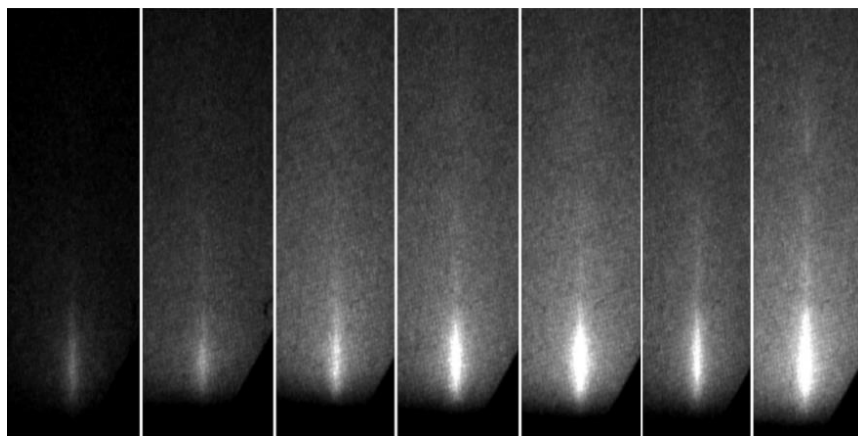


Figure 3-4 RHEED images of the HOPG substrate at different parts of the substrate (Z scan images)

### 3.3.2 Low-Temperature Structure of the IL on HOPG

Even though the IL shows no crystallization sign at room temperature, clear Bragg spots are produced when the sample temperature is sufficiently reduced (as is shown in Figure 3-5). Moreover, the same observation was produced at least two or three times for each film thickness (More than four times for the 2 nm and 3 nm films).

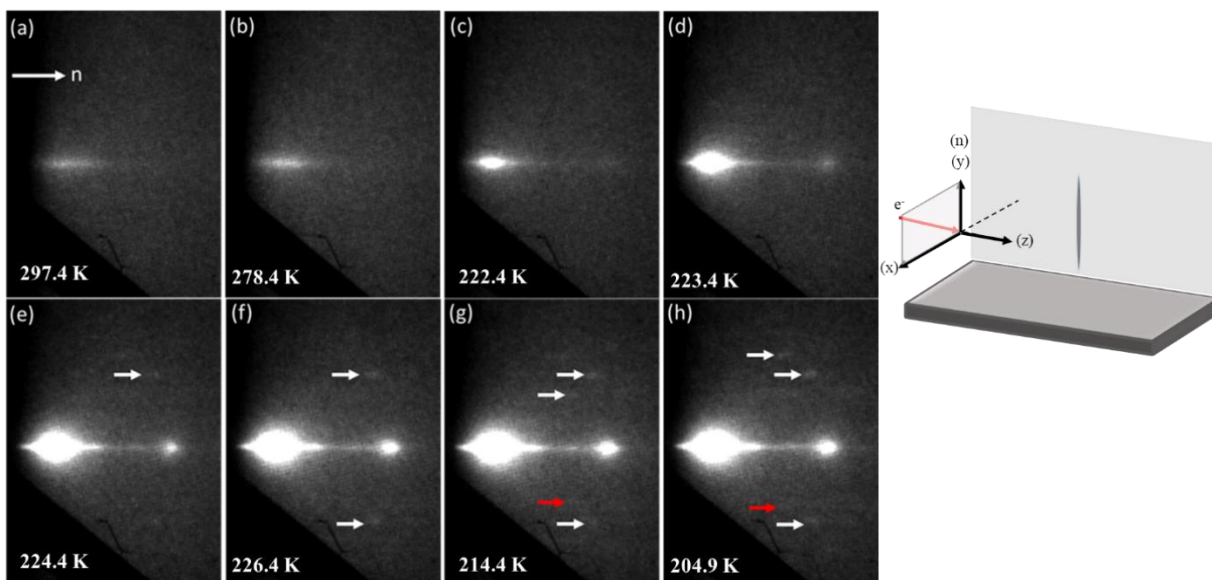


Figure 3-5 Crystallization of the 2.4 nm film IL on HOPG by lowering the temperature (from (a) to (h)). The arrows show the diffractions features at different selected temperatures. (The patterns are 90 degrees rotated (clockwise) compared to the HOPG image in Figure 3-3.

The Diffraction spots (red and white arrows) on the side streaks indicate in-plane crystallization parallel to the surface. In addition to that, the observed diffraction spots in the middle streak along the surface normal ( $\hat{n}$ ) show an excellent ordering along the surface normal (vertical ordering). A higher-quality image of the middle streak is shown in Figure 3-6 (b). Better well-defined Bragg spots along the surface normal than the side diffraction features indicate better ordering along the surface normal. The IL forms a 3-dimensional crystalline order on HOPG at low temperatures based on the horizontal and vertical ordering at low temperatures. The in-plane ordering is poor for the 2.4 nm film. However, it enhances in 3.2 nm film, as shown in Figure 3-6 (a), where the side diffraction features are sharper and extended more horizontally. It means higher orders of diffraction are apparent in the RHEED image. Moreover, the in-plane ordering is stable up to 10 nm film, while the vertical ordering is extended to 14 nm. The overall film thickness versus ordering is summarized in Table 3-3.

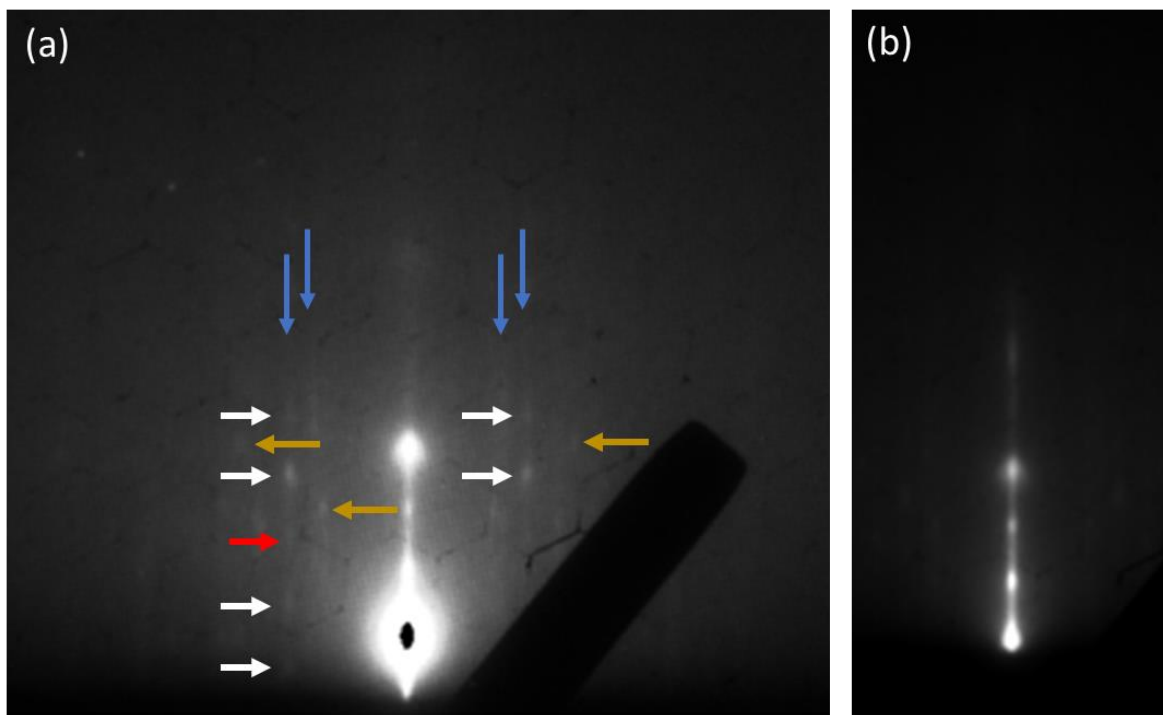


Figure 3-6 RHEED images of (a) 3.2 nm film IL on HOPG at low temperature. The horizontal features are extended to higher orders (b) Vertical ordering of 10 nm film on HOPG. Sharp diffraction spots show a high-quality ordering along the surface normal.

Table 3-3 Summarized film thicknesses, ordering horizontally and vertically for each film thickness.

IL film thickness	Horizontal ordering	Vertical ordering
Less than 2.4 nm	No Bragg Spots Observed	No Bragg Spots Observed
2.4 nm – 10 nm	Weak Bragg Spots Observed	Intense Bragg Spots Observed
10 nm – 14 nm	No Clear Bragg Spots Observed	Less Intense Bragg Spots Observed

The IL is crystallized in an azimuthally averaged condition, which means the diffraction pattern stays the same while the sample is rotating around the surface normal ( $\phi$ , Shown in Figure 3-7). Since no report has been published about crystallization of [EMIM][FSA] IL, it is essential to predict the possible crystal structure for the IL film on HOPG.

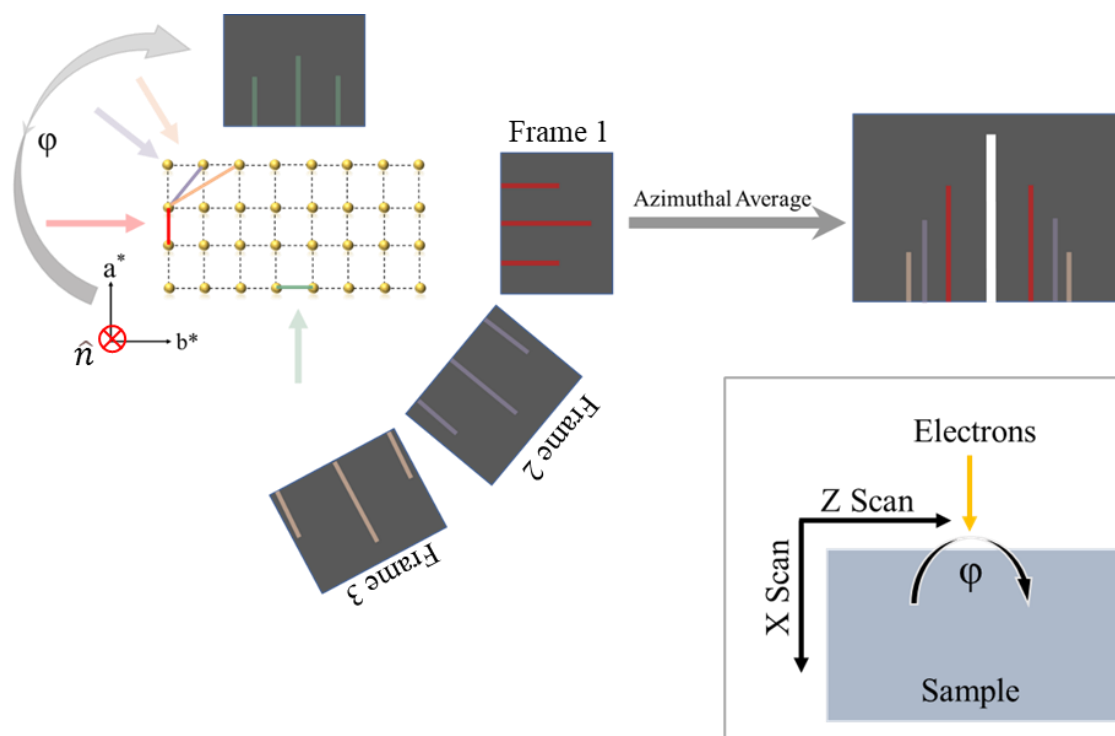


Figure 3-7 Schematic of an azimuthally averaged RHEED pattern. In this case, multiple zone axes are probed simultaneously, and one diffraction frame contains multiple streaks from different zone axes.

Generally, there are five possible 2D unit cells (shown in Figure 3-8; The rectangular case (c) is either simple or centered rectangular). Solving the structure requires considering each unit cell separately and comparing the possible streak positions with the experimental diffraction pattern. To solve the structure, the

first unit cell to consider is the square lattice. For a square lattice, the two lattice parameters are equal with a  $\theta = 90^\circ$  angle between the two lattice vectors. As a result, the reciprocal unit cell is similar to the real lattice, with  $|a^*| = |b^*|$ ,  $\theta^* = 90^\circ$ . In this case, possible diffraction streak positions are  $a^*$ ,  $a^*\sqrt{2}$ ,  $a^*\sqrt{5}$ ,  $a^*\sqrt{10}$ .

On the other hand, for a hexagonal lattice, where  $|a^*| = |b^*|$ ,  $\theta^* = 60^\circ$ , and the possible positions are  $a^*$ ,  $a^*\sqrt{3}$ ,  $a^*\sqrt{7}$ , as an example for the first three peaks. Since  $a^*$  in both cases is the smallest spacing, the first streak position is assigned to  $a^*$ . As a result, since in both of the  $a^*\sqrt{2}$  and  $a^*\sqrt{3}$  positions in the diffraction image there is a peak, both square lattice and the hexagonal lattice are ruled out. Since the square lattice cannot have a streak at  $a^*\sqrt{3}$  position, and the hexagonal lattice cannot have a streak at  $a^*\sqrt{2}$  position. In addition, the  $a^*\sqrt{10}$  and  $a^*\sqrt{7}$  streaks are missing, which further confirms the hypothesis (streak positions are summarized in Table 3-6).

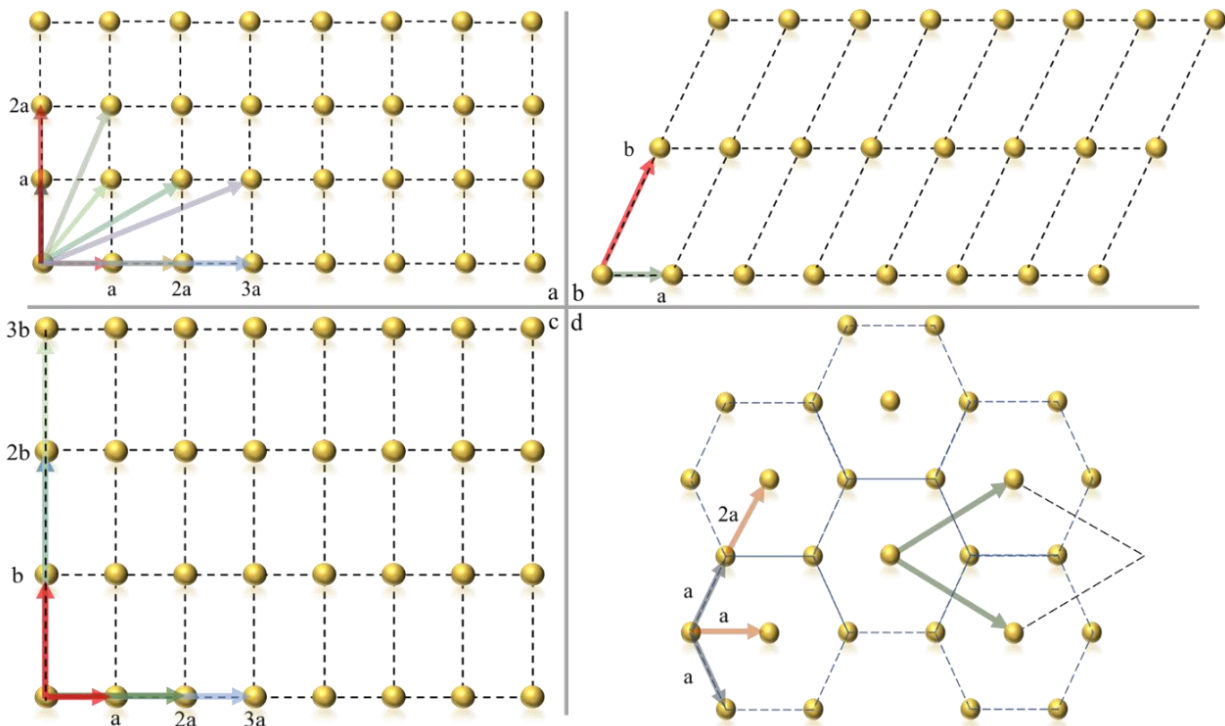


Figure 3-8 General possibility of 2-D unit cell structures of a crystal. (a) Square lattice (b) Oblique (c) Rectangular, which has a primitive and centered unit cell (The primitive is shown here) (d) Hexagonal lattice

The other possible structures are either the rectangular unit cell (Figure 3-8 (c)) or the oblique case (Figure 3-8 (b)). Since the oblique case has many possible combinations, the rectangular case is the following structure to investigate. Prior to further analysis of the crystal structure, it is beneficial to compare the crystallization of other reported RTILs.

More than 30 RTILs are listed in appendix (A), along with their CSD identification numbers. The ILs which crystallizes by  $\alpha=\beta=\gamma=90^\circ$ , are selected as shown in Table 3-4. Three main parameters are considered here to compare with the crystal structures, symmetry of the anions, relative size of the anion and cation, and finally, the chain length of the imidazolium cation. Each IL is called with the corresponding CSD file number for future references. The two possible structures are either orthorhombic ( $a \neq b \neq c$  and  $\alpha = \beta = \gamma = 90^\circ$ ) or monoclinic ( $a \neq b \neq c$  and  $\alpha = \beta = 90^\circ, \gamma \neq 90^\circ$ ). For example, the IL 614037 is [EMIM][TFSA], one of the most common and well-studied ILs, with an orthorhombic structure. Among these ILs, 28064, 28065, 614037, and 713637 have [EMIM] cation. On the other hand, 280603, 839609, 639882, and 639890 are imidazolium cations with a higher symmetry anion than the [TFSA] anion. All the ILs mentioned above have a monoclinic unit cell. Even the 701482 and 614037 ILs with the same [EMIM] cation and [TFSA] anion, and only a different symmetry of the anion (Shown in Figure 3-9 a and b) causes a change of unit cell from orthorhombic to monoclinic.

In summary, [EMIM] cation and anions of relatively the same size, such as [TFSA], crystallize most likely in orthorhombic structure. In addition, It also mainly crystallizes in monoclinic structure with the anions of much smaller relative size to the [EMIM], and higher symmetry or closer to a sphere shape such as [SbF<sub>6</sub><sup>-</sup>], [PF<sub>6</sub><sup>-</sup>], [FeCl<sub>4</sub><sup>-</sup>], or even [BF<sub>4</sub><sup>-</sup>], shown in Figure 3-10.

On the other hand, a monoclinic structure is reported for the imidazolium cations with longer chains, such as [BMIM]. Similarly, for the cations with similar chain lengths attached to nitrogen atoms, such as [MMIM] and [EEIM], which have higher symmetry vs. [EMIM]. In conclusion to this comparison, it is a

promising guess for the [EMIM][FSA] IL to crystallize in a similar structure as [EMIM][TFSA], with orthorhombic unit cell.

Table 3-4 Selected ILs – Crystallize with  $\alpha=\beta=\gamma=90^\circ$ . T (C) is crystallization temperature in Kelvin. The r values are an estimation of the longest length for each cation and anion, which is shown in the appendix (A).

File Number	a	b	c	$\alpha$	$\beta$	$\gamma$	T (C) K	r (Cation) Å	r (Anion) Å	$\frac{r(+)}{r(-)}$
116893	11.896	12.704	12.95	90	90	90	123	5.598	4.065	1.38
148580	9.894	13.846	19.856	90	90	90	150	6.962	5.863	1.19
280604	9.204	9.77	12.499	90	90	90	200	7.167	3.764	1.90
280605	9.216	9.763	12.502	90	90	90	200	7.174	3.735	1.92
614037	18.499	8.626	19.255	90	90	90	230	7.215	6.472	1.11
621179	8.28	10.788	11.998	90	90	90	93	8.483	2.06	4.12
710931	8.496	13.123	16.692	90	90	90	230	8.202	7.078	1.16
713637	27.713	7.034	15.796	90	90	90	100	7.287	7.085	1.03
824302	9.657	11.141	14.651	90	90	90	213	5.816	7.119	0.82

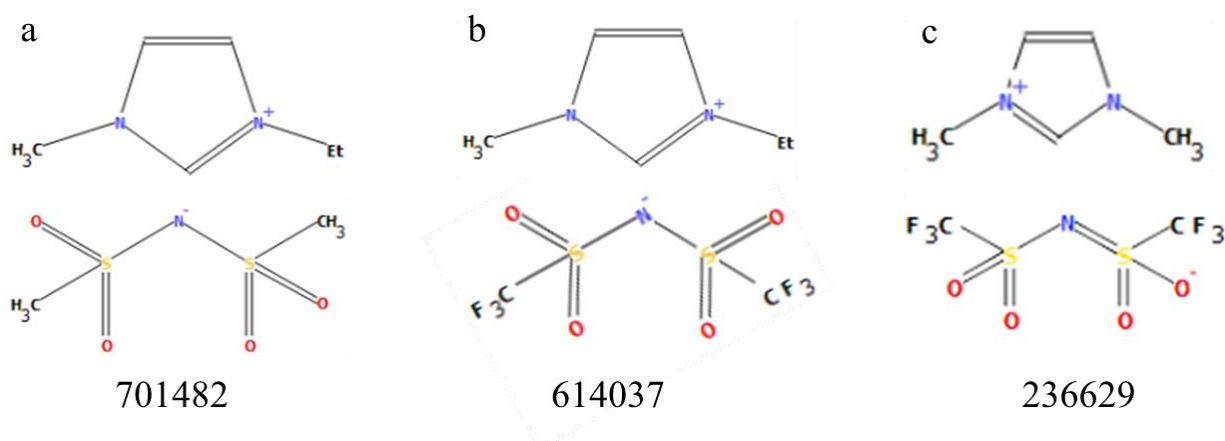


Figure 3-9 (a and b) The ILs with similar cations and anions and different anion symmetry result in different crystal structures. (c) same cation chain length on both nitrogen atoms resulting in a different crystal structure.

As a result, the in-plane structure of the IL is a rectangular shape. Since the RHEED image shows an azimuthally averaged diffraction pattern, the first streak position is the reciprocal vector related to the lattice parameters ( $a$  or  $b$ ). Here the first streak position is assigned to  $b^*$ .

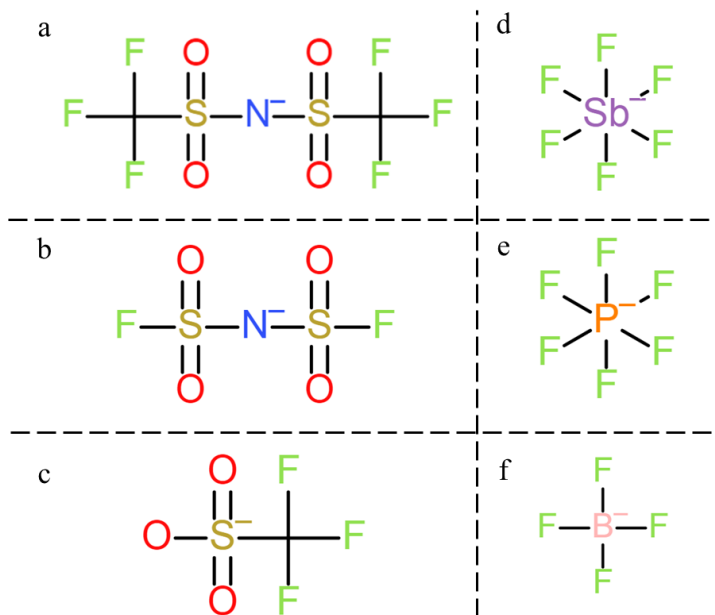


Figure 3-10 The anions of the ILs compared in the main text.

The result of the streak indexing from [EMIM][TFSA] simulation is shown in Table 3-5. The indexing is in a reasonable agreement with the streak positions within  $\pm 2\%$ . Therefore, the indexing from the simulation is a reasonable start to predict the lattice parameters of the [EMIM][FSA] IL (Details of the simulation are discussed in appendix (A)).

Table 3-5 [EMIM][TFSA] streaks indexing from simulation

$\delta_h$ (Pixel numbers)	Index	$\varphi_s$
46	(0 1)	0
42.5	(2 0)	90
49.5	(1 1)	25
62	(2 1)	43
78	(3 1)	54.4
93	(1 2)	62
96.8	(4 1)	13

### 3.3.3 Lattice Parameters Calculation for a Rectangular Unit Cell

The first streak position is assigned to  $b^*$ , which leads to the derivation of  $b=8.7 \text{ \AA}$ . The second streak position is either for (2 0) or (1 1). Since  $a \cong 2b$  in a real-space rectangular lattice, in reciprocal space  $2a^* \cong$

$b^*$ , and therefore (0 1) and (2 0) streaks overlap. An example of calculation for indexing is shown in appendix (A). According to the [EMIM][TFSA] indexing, the next streak is assigned to (1 1) zone, which as a result, the corresponding lattice parameter (assigned to “a” lattice parameter) is predicted to be 16.2 Å. It is also in good agreement with the previous assumption of  $a \cong 2b$ . To further investigate the validity of the assumptions, and predicted lattice parameters, the rest of the reciprocal vectors are predicted based on the extracted ( $a^*$ ,  $b^*$ ) from the experimental diffraction pattern of the [EMIM][FSA] IL and is then compared with the experimental streak positions (As is shown in Table 3-6). The (2 1), (3 1), and (4 1) zones are all in agreement with the experimental streak positions with less than 2% deviation. Since the (1 1) zone has a higher streak intensity, the prediction of the lattice parameters is more accurate based on the combination of (0 1) and (1 1) zones. The details of the indexing are elaborated in appendix (A).

Table 3-6 [EMIM][FSA] Experimental streaks vs. [EMIM][TFSA] simulated streaks positions.

Ruling out square and hexagonal lattices	$S_{(hk)}$ Experimental	Index	$S_{(hk)}$ Predicted	Value in Å	
0.114	0.114	(0 1)	----	b = 8.70	Predicted Lattice Parameters
	0.123	(2 0)	----	a = 16.20	
	0.131	(1 1)	0.130	0.76%	Deviation from Predicted Streak Positions
$0.114\sqrt{2} = 0.162$	0.163	(2 1)	0.166	1.80%	
$0.114\sqrt{3} = 0.199$	0.209	(3 1)	0.212	1.78%	
	----	(1 2)	0.237	----	
	0.267	(4 1)	0.271	1.77%	

It is shown in Table 3-6 that: (1) The square and hexagonal lattices are not the possible unit cell of the IL (shaded left-middle side of the table) (2) The S-vectors for [EMIM][FSA] are in close agreement with the predicted S-vectors for the rectangular unit cell (3) The a and b lattice parameters are in good agreement with the assumption of  $a \cong 2b$ , which is the reason of streaks at positions for both square and hexagonal lattices (They both have  $a = b$ )

It must be noted that the numbers in Table 3-6 are directly reported for the discussion over the similarity of the predicted 2D unit cell with a rectangular lattice ( $a \cong 2b$ ). The final reported numbers within the experimental accuracy of the RHEED setup are  $a = 8.7 \text{ \AA}$ , and  $b = 16.2 \text{ \AA}$ .

### 3.3.4 Vertical Spacing –The Rocking Curve

In addition to the in-plane lattice parameters, the vertical spacing can be extracted using the rocking curve method (Results shown in Figure 3-11). Since the RHEED patterns at a grazing incidence angle of the electrons only provide 2-D structural information, the vertical order information can be extracted by increasing the incident angle and recording the RHEED patterns at higher angles (Details are explained previously). As a result, a vertical spacing of  $12.2 \text{ \AA}$  is extracted. With the assumption of the unit cell similarity of the two ILs, the  $c$  value of the unit cell for [EMIM][FSA] might be twice this vertical spacing, which results in  $c = 24.4 \text{ \AA}$ .

At this point, it is beneficial to discuss the possible reason/reasons for the high-quality vertical ordering and low-quality in-plane ordering of this IL and compare it with other well-studied ILs, such as [EMIM][TFSA] and 1-Ethyl-3-methylimidazolium trifluoromethanesulfonate [EMIM][OTF]. Two possible reasons can be hypothesized for crystallization of the [EMIM][FSA] on HOPG; (1) vertical lattice matching (template-effect) [28], or (2) in-plane lattice matching (epitaxial growth) [52, 53]. The epitaxial effect of the ionic liquids on different gold facets is discussed with simulations. However, the systems under study are the growth of nanoparticles induced and controlled in an IL environment, and not a possible reason for the HOPG-IL case, which is discussed later.

Both cases are shown schematically in Figure 3-12, with the corresponding lattice mismatch for all lattice parameters. The diffraction patterns vs. the IL film thicknesses are generally divided into three regions. (1) less than  $\approx 2.4 \text{ nm}$ , (2)  $\approx (2.4 \text{ nm} - 14 \text{ nm})$ , (3) more than  $\approx 14 \text{ nm}$ . In the first region, there is no crystallization of the IL, even at low temperatures. It is worth noting that the minimum film thickness ( $\approx 2.4$

nm) is very close to the predicted “c” value of the unit cell (24.4 Å). In the second region, the in-plane diffraction features are stronger for the  $\approx$  (2.4 nm – 6 nm) films and less intense for  $\approx$  (6 nm – 10 nm) films. In general, the in-plane ordering is more well-defined in the lower range and worsens at higher thicknesses, while the vertical ordering is strong and extended up to  $\approx$  14 nm film, even though diffraction features are slightly weaker for 10 nm to 14 nm films.

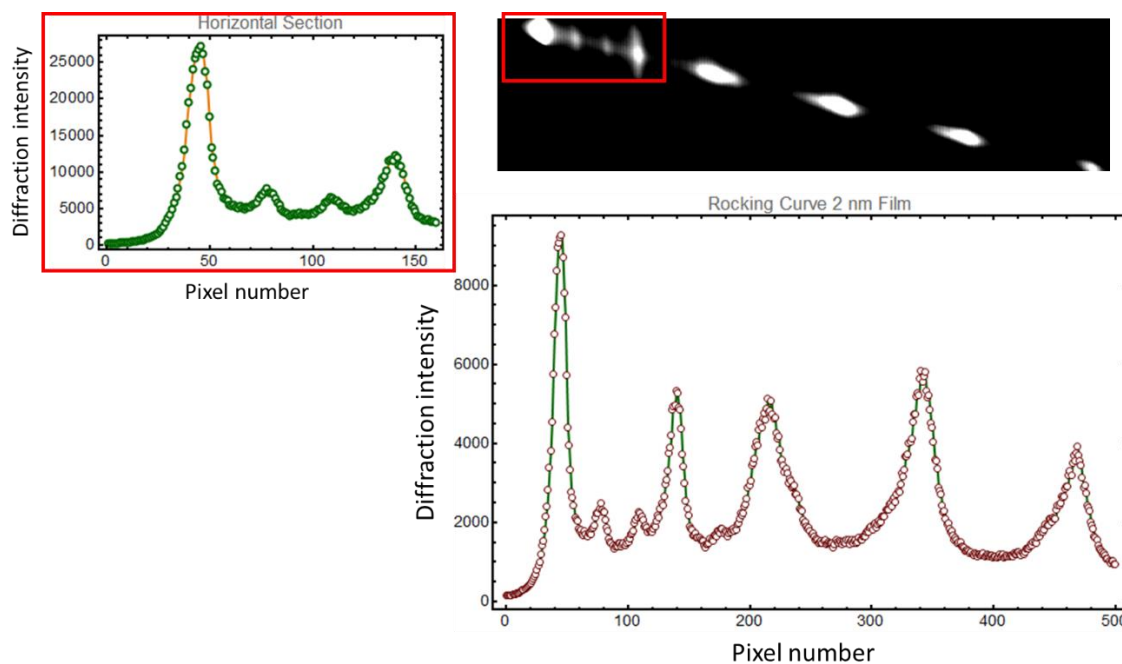


Figure 3-11 The rocking curve for [EMIM][FSA] IL. The HOPG spots with equal spacings are shown at higher angles, while at lower incident angles, smaller spots with smaller spacings are for the IL vertical ordering.

A few things here are worth discussing. (1) better in-plane diffraction features at lower thicknesses vs. the higher thickness could be related to the in-plane lattice matching (one possible in-plane lattice matching is shown schematically in Figure 3-12 (left)). However, the vertical ordering might be related to vertical lattice matching (shown on the right) of the IL unit cell and 4-layers of the terraced HOPG substrate. The vertical ordering has a much better ordering and extended to  $\approx$  14 nm films. Even though the in-plane lattice mismatch ( $\approx$  2% - 7%) is much smaller than the vertical lattice mismatch ( $\approx$  10%), the vertical ordering is much better normal to the HOPG surface than the ordering parallel HOPG substrate. Here, the vertical lattice mismatch is

calculated as  $(n \times d_{HOPG} - d_{IL})/d_{IL}$ , with  $n = 4$  for this IL, and the in-plane mismatching is calculated based on the carbon bonds in the top HOPG layer.

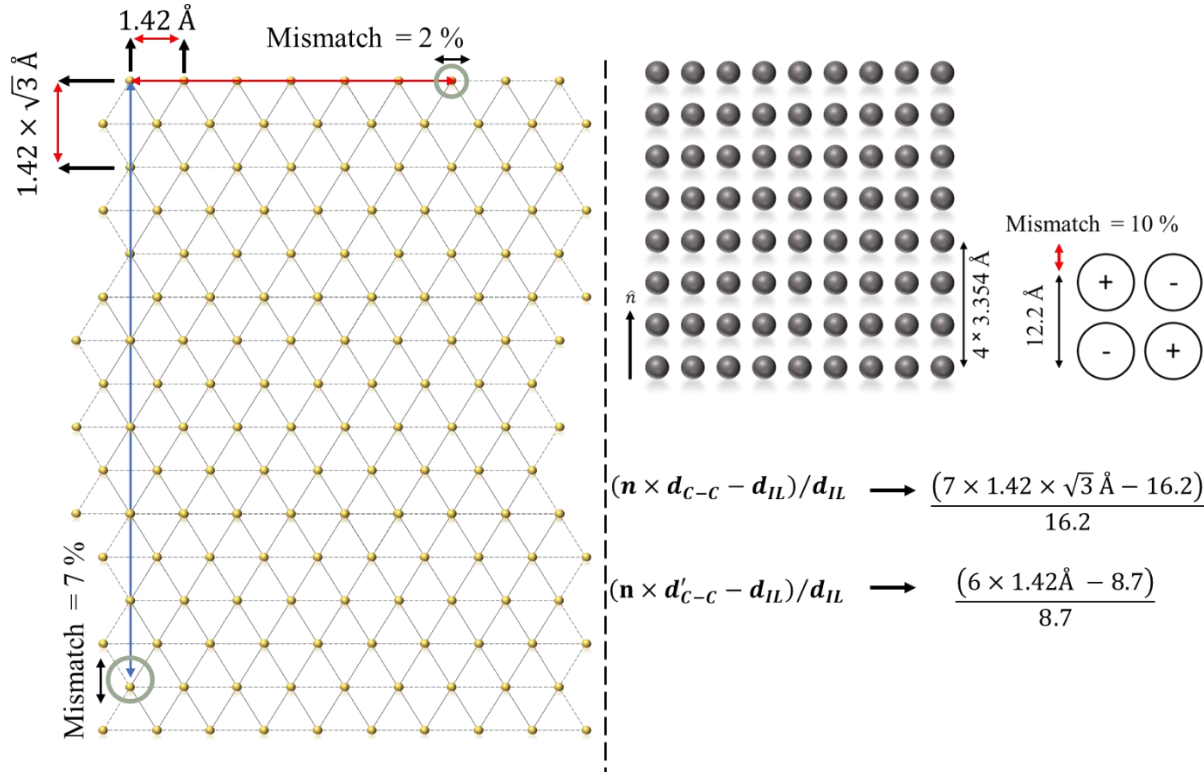


Figure 3-12 (Left) In-plane lattice mismatch for the predicted IL lattice parameters (a and b). (Right) Vertical lattice mismatch for the predicted IL lattice parameter (c). Calculation of lattice mismatch is shown on the bottom right.

This contradiction between lattice mismatching and the quality of the ordering for in-plane and normal to the surface shows that the lattice matching is not the only parameter defining the quality and the range of the ordering. In addition, the upper overlayers above the immediate interfacial layer should see mostly ILs below. Given the resembling ion sizes, it is likely that the crystallization of the overlayers is not hindered by the HOPG lattice anymore, even though there may be some interfacial structure or an excess of specific ions. This contradiction shows that the in-plane lattice matching does not play a role in the case of the HOPG-IL system. However, this is only one possible in-plane lattice matching, and there might be other situations with even better matching. Also, it is insightful to mention that the first layer which was in direct contact to

the HOPG didn't crystallize, which is an additional reason showing that the first layer matching with the substrate didn't play a role.

On the other hand, one reason for a better vertical ordering with an extended range can be assigned to the  $\pi - \pi$  interaction of the imidazolium rings. Moreover, it can be due to less steric effect than the [EMIM][TFSA] IL due to the smaller anion size. In this case, the imidazolium rings must be parallel to the substrate, which is the same situation in the reported case for [EMIM][TFSA] IL on HOPG [54]. This study concluded that for the first layer of the IL, the interaction between IL and substrates plays a significant role by comparing HOPG and Au (111) substrates. However, the ordering of the upper layers is mainly governed by the interactions of the ions, such as Coulombic interactions and hydrogen bonding. As a result, it can be concluded that the template-effect in combination with the imidazolium rings interactions are the main reasons for a better vertical ordering.

Moreover, since the vertical ordering disappears after  $\approx 14$  nm films, it is crucial to investigate the upper layer molecular orientations vs. film thickness. One possible reason is that the relative orientation of the cation rings may change at higher thicknesses. On the other hand, the template-effect (vertical lattice matching) is reduced at higher thicknesses. So, the question is, what happens to the orientation of the top layer molecules, and whether the bottom layers collapse or stay crystalized when the diffraction patterns show diffuse background by adding an additional one nm film. The answer to this question needs investigation of the molecular orientations vs. IL film thicknesses, which is the motivation for the next chapter, and developing an environment to perform the same type of experiments combining RHEED with sum-frequency generation spectroscopy (SFG) system.

It is informative to compare [EMIM][TFSA], [EMIM][OTF], [EMIM][FSA], and [BMPy][TFSA] ILs. which their crystal structures were discussed in this chapter to predict the [EMIM][FSA] IL structure. Crystallization of the other three ILs on HOPG was studied with the RHEED technique in our lab [28]. The

final data from the previous works are compared with the [EMIM][FSA] in Table 3-7. It is noticeable from this comparison that the crystallinity and the overall film quality has a clear relation with the relative size of the cation and anion and with the symmetry of the anions (since [TFSA] and [FSA] are very similar and different from [OTF]). The [EMIM] cation size is very close to the [TFSA], while the anion size decreases for [FSA] and for [OTF]. On the other hand, both [TFSA] and [FSA] cases resulted in a 3-D crystallization. Since the [FSA] and [OTF] show similar lattice mismatch and different crystallinity, the template-effect may be more responsible for the vertical ordering than the ions' relative size and symmetry. In addition, the relative size and symmetry are more likely import parameters for a 3-D crystallization. The latter is in good agreement with the [BMPy][TFSA] IL, which shows no crystallization. First, the lack of vertical ordering is mainly due to a significant lattice mismatch of 21.2%. At the same time, the relative size (bigger cation) also reduces the possibility of in-plane ordering even at lower film thicknesses.

Table 3-7 The qualitative comparisons of the four ILs' thin films on HOPG substrate with respect to the [EMIM][TFSA] film quality based on the RHEED diffraction patterns.

	[EMIM][TFSA]	[EMIM][FSA]	[EMIM][OTF]	[BMPy][TFSA]
Crystallinity	3-D	3-D	Only Vertical	N/A
Ordered range	2 – 12 nm	2.4 – 14 nm	2 – 8.3 nm	N/A
Lattice mismatch	4.4%	10%	9.9%	21.2%
Vertical order quality	High	High	Good	N/A
In-plane order quality	High	Good	Poor	N/A

Lastly, the temperature-dependent behavior of [EMIM][FSA] shows the typical hysteresis behavior in its cooling-heating curve (as is shown in Figure 3-13). While the crystallization happens at  $\approx 230$  K, the melting temperature is  $\approx 242$  K, which shows a 12 K difference. This  $\Delta T$  is almost 20 K for the [EMIM][TFSA] IL (235 K – 255 K). The crystallization temperature is very close to each other for both ILs, while the [EMIM][TFSA] melting happens at a higher temperature. This temperature is not dependent on the film thickness and shows the same behavior for all film thicknesses from 2.4 nm to 10 nm.

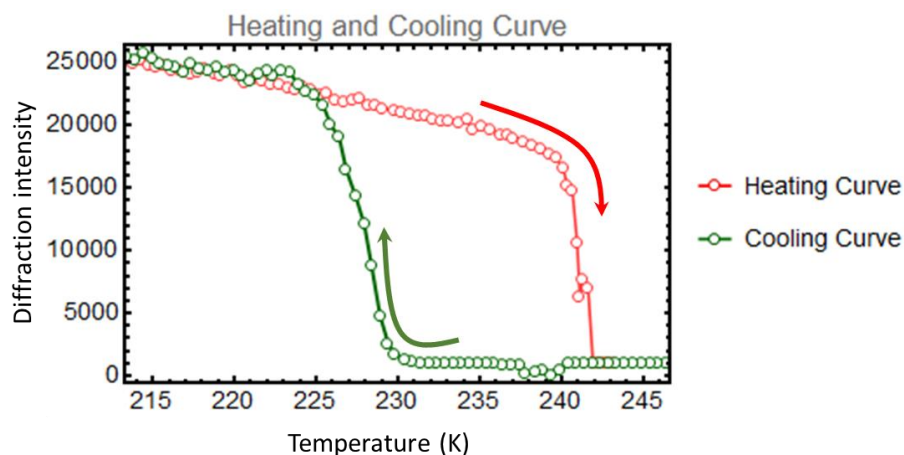


Figure 3-13 Typical intensity changes of the IL diffraction spots as a function of temperature in cooling (green) and heating (red) cycles.

### 3.4 Conclusion

In conclusion, the thickness-dependent behavior of an RTIL deposited by physical vapor deposition has been discussed. The crystal information of the IL thin film on HOPG substrate has been investigated using reflection high-energy electron diffraction. Even though the RHEED technique is not enough to calculate lattice parameters and the unit cell structure of a molecular crystal, the possibility of predicting the most likely crystal structure has been discussed. The lattice parameters are predicted ( $a = 8.70 \text{ \AA}$ ,  $b = 16.20 \text{ \AA}$ , and  $c = 24.40 \text{ \AA}$ ), which was later compared with more than 30 different ILs to discuss the validity of the prediction. The thickness-dependent behavior of the [EMIM][FSA] on HOPG substrate can be divided into two parts: the in-plane ordering and the vertical ordering. The in-plane ordering itself showed three regions for the evolution of the cation/anion ordering on HOPG. There was no ordering for IL films less than 2.4 nm and higher than 10 nm, while for the 2.4 nm – 10 nm range, the IL was crystallized in a 3-dimensional form.

On the other hand, the vertical ordering, which also shows the same three regions, showed no ordering for films less than 2.4 nm and higher than 14 nm, while the vertical ordering was well-defined in the 2.4 nm – 14 nm range. The extended and more well-defined vertical ordering can be related to the previously reported template effect from the HOPG terraces and the additional forces between the imidazolium rings that are most

likely parallel to the surface. Comparing these behaviors with three other ILs further supports the assumptions made to solve the crystal structure of the [EMIM][FSA] thin films on HOPG. It was also shown that the IL fails to crystallize after a specific film thickness, which is a general case for other ILs discussed in this chapter. Therefore, it is crucial to investigate further the effect of the top layers of the IL film on the bottom layers, which might still show some partial structural orientational ordering. This behavior is the motivation of the next chapter to develop the possibility of investigation of IL films in the ultrathin region with other orientation sensitive techniques (SFG) while the sample is under an ultraclean (UHV) environment.

### 3.5 Bibliography

- [1] N. V. Plechkova and K. R. Seddon, "Applications of ionic liquids in the chemical industry," *Chemical Society Reviews*, vol. 37, no. 1, pp. 123-150, 2008.
- [2] P. Wasserscheid and W. Keim, "Ionic liquids—new “solutions” for transition metal catalysis," *Angewandte Chemie International Edition*, vol. 39, no. 21, pp. 3772-3789, 2000.
- [3] K. Binnemans, "Ionic liquid crystals," *Chemical Reviews*, vol. 105, no. 11, pp. 4148-4204, 2005.
- [4] T. Cremer, M. Killian, J. M. Gottfried, N. Paape, P. Wasserscheid, F. Maier, and H. -P. Steinrück, "Physical vapor deposition of [EMIM][Tf<sub>2</sub>N]: a new approach to the modification of surface properties with ultrathin ionic liquid films," *ChemPhysChem*, vol. 9, no. 15, pp. 2185-2190, 2008.
- [5] C. Kolbeck, M. Killian, F. Maier, N. Paape, P. Wasserscheid, and H. P. Steinrück, "Surface characterization of functionalized imidazolium-based ionic liquids," *Langmuir*, vol. 24, no. 17, pp. 9500-9507, 2008.
- [6] P. Wasserscheid and T. Welton, *Ionic Liquids in Synthesis*. John Wiley & Sons, 2008.
- [7] H. Weingärtner, "Understanding ionic liquids at the molecular level: facts, problems, and controversies," *Angewandte Chemie International Edition*, vol. 47, no. 4, pp. 654-670, 2008.
- [8] H. Liu, Y. Liu, and J. Li, "Ionic liquids in surface electrochemistry," *Physical Chemistry Chemical Physics*, vol. 12, no. 8, pp. 1685-1697, 2010.
- [9] T. Welton, "Room-temperature ionic liquids. Solvents for synthesis and catalysis," *Chemical Reviews*, vol. 99, no. 8, pp. 2071-2084, 1999.
- [10] C. Capello, U. Fischer, and K. Hungerbühler, "What is a green solvent? A comprehensive framework for the environmental assessment of solvents," *Green Chemistry*, vol. 9, no. 9, pp. 927-934, 2007.
- [11] H. P. Steinrück, "Recent developments in the study of ionic liquid interfaces using X-ray photoelectron spectroscopy and potential future directions," *Physical Chemistry Chemical Physics*, vol. 14, no. 15, pp. 5010-5029, 2012.
- [12] S. Baldelli, "Interfacial structure of room-temperature ionic liquids at the solid-liquid interface as probed by sum-frequency generation spectroscopy," *The Journal of Physical Chemistry Letters*, vol. 4, no. 2, pp. 244-252, 2013.
- [13] C. Y. Penalber, G. A. Baker, and S. Baldelli, "Sum frequency generation spectroscopy of imidazolium-based ionic liquids with cyano-functionalized anions at the solid salt-liquid interface," *Journal of Physical Chemistry B*, vol. 117, no. 19, pp. 5939-49, May 16, 2013.
- [14] R. Hayes, G. G. Warr, and R. Atkin, "Structure and nanostructure in ionic liquids," *Chemical Reviews*, vol. 115, no. 13, pp. 6357-6426, 2015.

- [15] C. Aliaga and S. Baldelli, "A sum-frequency generation study of the room-temperature ionic liquid–titanium dioxide interface," *Journal of Physical Chemistry C*, vol. 112, no. 8, pp. 3064–3072, 2008.
- [16] S. Bovio, A. Podesta, C. Lenardi, and P. Milani, "Evidence of extended solid-like layering in [Bmim][NTf<sub>2</sub>] ionic liquid thin films at room temperature," *The Journal of Physical Chemistry B*, vol. 113, no. 19, pp. 6600–6603, 2009.
- [17] B. D. Fitchett and J. C. Conboy, "Structure of the room-temperature ionic liquid/SiO<sub>2</sub> interface studied by sum-frequency vibrational spectroscopy," *The Journal of Physical Chemistry B*, vol. 108, no. 52, pp. 20255–20262, 2004.
- [18] R. Fortunato, C. A. Afonso, J. Benavente, E. Rodriguez-Castellón, and J. Crespo, "Stability of supported ionic liquid membranes as studied by X-ray photoelectron spectroscopy," *Journal of Membrane Science*, vol. 256, no. 1–2, pp. 216–223, 2005.
- [19] J. M. Gottfried, F. Maier, J. Rossa, D. Gerhard, P. S. Schulz, P. Wasserscheid and H.-P. Steinrück, "Surface studies on the ionic liquid 1-ethyl-3-methylimidazolium ethylsulfate using X-ray photoelectron spectroscopy (XPS)," *Zeitschrift für Physikalische Chemie*, vol. 220, no. 10, pp. 1439–1453, 2006.
- [20] F. Maier, J. M. Gottfried, J. Rossa, D. Gerhard, P.S. Schulz, W. Schwiege, P. Wasserschei, H. P. Steinrück, "Surface enrichment and depletion effects of ions dissolved in an ionic liquid: An X-ray photoelectron spectroscopy study," *Angewandte Chemie International Edition*, vol. 45, no. 46, pp. 7778–7780, 2006.
- [21] K. R. J. Lovelock, C. Kolbeck, T. Cremer, N. Paape, P. S. Schulz, P. Wasserscheid, F. Maier, H.-P. Steinrück, "Influence of different substituents on the surface composition of ionic liquids studied using ARXPS," *The Journal of Physical Chemistry B*, vol. 113, no. 9, pp. 2854–2864, 2009.
- [22] Y. Z. Su, Y. C. Fu, Y. M. Wei, J. W. Yan, and B. W. Mao, "The electrode/ionic liquid interface: electric double layer and metal electrodeposition," *ChemPhysChem*, vol. 11, no. 13, pp. 2764–2778, 2010.
- [23] F. Endres, N. Borisenko, S. Z. El Abedin, R. Hayes, and R. Atkin, "The interface ionic liquid (s)/electrode (s): In situ STM and AFM measurements," *Faraday Discussions*, vol. 154, pp. 221–233, 2012.
- [24] R. Hayes, N. Borisenko, M. K. Tam, P. C. Howlett, F. Endres, and R. Atkin, "Double-layer structure of ionic liquids at the Au (111) electrode interface: an atomic force microscopy investigation," *The Journal of Physical Chemistry C*, vol. 115, no. 14, pp. 6855–6863, 2011.
- [25] Y. Yokota, H. Hara, T. Harada, A. Imanishi, T. Uemura, J. Takeya and K.-i Fukui, "Structural investigation of ionic liquid/rubrene single-crystal interfaces by using frequency-modulation atomic force microscopy," *Chemical Communications*, vol. 49, no. 90, pp. 10596–10598, 2013.
- [26] H. A. Löytty, M. W. Louie, M. R. Singh, L. Li, H. G. Sanchez Casalongue, H. Ogasawara, E. J. Crumlin, Z. Liu, A. T. Bell, A. Nilsson, D. Friebe, "Ambient-pressure XPS study of a Ni–Fe electrocatalyst for the oxygen evolution reaction," *The Journal of Physical Chemistry C*, vol. 120, no. 4, pp. 2247–2253, 2016.

- [27] P. Cheng and X. Zhan, "Stability of organic solar cells: challenges and strategies," *Chemical Society Reviews*, vol. 45, no. 9, pp. 2544-2582, 2016.
- [28] X. He, C. Wu, K. Rajagopal, N. Punpongjareorn, and D.-S. Yang, "Ordered ionic liquid structure observed at terraced graphite interfaces," *Physical Chemistry Chemical Physics*, vol. 18, no. 5, pp. 3392-3396, 2016.
- [29] P. C. Hiemenz and R. Rajagopalan, *Principles of Colloid and Surface Chemistry, revised and expanded*. CRC Press, 2016.
- [30] T. Iimori, R. Ito, and N. Ohta, "Stark spectroscopy of rubrene. II. Stark fluorescence spectroscopy and fluorescence quenching induced by an external electric field," *Journal of Physical Chemistry A*, vol. 120, no. 28, pp. 5497-503, Jul 21, 2016.
- [31] T. Ueba, T. Yamada, and T. Munakata, "Electronic excitation and relaxation dynamics of the LUMO-derived level in rubrene thin films on graphite," *Journal of Chemical Physics*, vol. 145, no. 21, p. 214703, Dec 7, 2016.
- [32] P. Vancsó, G. Z. Magda, J. Pető, J.-Y. Noh, Y.-S. Kim, C. Hwang, L. P. Biró and, L. Tapasztó, "The intrinsic defect structure of exfoliated MoS<sub>2</sub> single layers revealed by scanning tunneling microscopy," *Scientific Reports*, Article vol. 6, p. 29726, 07/22/online 2016.
- [33] H.-F. Wang, "Sum frequency generation vibrational spectroscopy (SFG-VS) for complex molecular surfaces and interfaces: Spectral line shape measurement and analysis plus some controversial issues," *Progress in Surface Science*, vol. 91, no. 4, pp. 155-182, 2016/12/01/ 2016.
- [34] D. Zheng, L. Lu, Y. Li, K. F. Kelly, and S. Baldelli, "Compressive broad-band hyperspectral sum frequency generation microscopy to study functionalized surfaces," *The Journal of Physical Chemistry Letters*, vol. 7, no. 10, pp. 1781-1787, 2016.
- [35] T. Waldmann, H. H. Huang, H. E. Hoster, O. Höfft, F. Endres, and R. J. Behm, "Imaging an ionic liquid adlayer by scanning tunneling microscopy at the solid| vacuum interface," *ChemPhysChem*, vol. 12, no. 14, pp. 2565-2567, 2011.
- [36] L. Høgstedt, J. S. Dam, A.-L. Sahlberg, Z. Li, M. Aldén, C. Pedersen, and P. T. Lichtenberg, "Low-noise mid-IR upconversion detector for improved IR-degenerate four-wave mixing gas sensing," *Optics Letters*, vol. 39, no. 18, pp. 5321-5324, 2014.
- [37] Y.-X. Zhong, J.-W. Yan, M.-G. Li, X. Zhang, D.-W. He, and B.-W. Mao, "Resolving fine structures of the electric double layer of electrochemical interfaces in ionic liquids with an AFM tip modification strategy," *Journal of the American Chemical Society*, vol. 136, no. 42, pp. 14682-14685, 2014.
- [38] Z. Brkljača, M. Klimczak, Z. Miličević, M. Weisser, N. Taccardi, P. Wasserscheid, D. M. Smith, A. Magerl, A.-S. Smith, "Complementary molecular dynamics and X-ray reflectivity study of an imidazolium-based ionic liquid at a neutral sapphire interface," *The Journal of Physical Chemistry Letters*, vol. 6, no. 3, pp. 549-555, 2015.

- [39] M. Mezger, H. Schröder, H. Reichert, S. Schramm, J. S. Okasinski, S. Schöder, V. Honkimäki, M. Deutsch, B. M. Ocko, J. Ralston, M. Rohwerder, M. Stratmann and H. Dosch, "Molecular layering of fluorinated ionic liquids at a charged sapphire (0001) surface," *Science*, vol. 322, no. 5900, pp. 424-428, 2008.
- [40] S. Baldelli, "Surface structure at the ionic liquid– electrified metal interface," *Accounts of Chemical Research*, vol. 41, no. 3, pp. 421-431, 2008.
- [41] A. Riisager, P. Wasserscheid, R. van Hal, and R. Fehrmann, "Continuous fixed-bed gas-phase hydroformylation using supported ionic liquid phase (SILP) Rh catalysts," *Journal of Catalysis*, vol. 219, no. 2, pp. 452-455, 2003.
- [42] A. J. Carmichael, C. Hardacre, J. D. Holbrey, M. Nieuwenhuyzen, and K. Seddon, "Molecular layering and local order in thin films of 1-alkyl-3-methylimidazolium ionic liquids using X-ray reflectivity," *Molecular Physics*, vol. 99, no. 10, pp. 795-800, 2001.
- [43] G. Yu, F. Zhou, W. Liu, Y. Liang, and S. Yan, "Preparation of functional ionic liquids and tribological investigation of their ultra-thin films," *Wear*, vol. 260, no. 9-10, pp. 1076-1080, 2006.
- [44] G. Yu, S. Yan, F. Zhou, X. Liu, W. Liu, and Y. Liang, "Synthesis of dicationic symmetrical and asymmetrical ionic liquids and their tribological properties as ultrathin films," *Tribology Letters*, vol. 25, no. 3, pp. 197-205, 2007.
- [45] S. Maruyama, Y. Takeyama, H. Taniguchi, H. Fukumoto, M. Itoh, H. Kumigashira, M. Oshima, T. Yamamoto, and Y. Matsumoto, "Molecular beam deposition of nanoscale ionic liquids in ultrahigh vacuum," *ACS Nano*, vol. 4, no. 10, pp. 5946-5952, 2010.
- [46] X. Gong, S. Frankert, Y. Wang, and L. Li, "Thickness-dependent molecular arrangement and topography of ultrathin ionic liquid films on a silica surface," *Chemical Communications*, vol. 49, no. 71, pp. 7803-7805, 2013.
- [47] A. Deyko, T. Cremer, F. Rietzler, S. Perkin, L. Crowhurst, T. Welton, H.-P. Steinrück, and F. Maier, "Interfacial behavior of thin ionic liquid films on mica," *The Journal of Physical Chemistry C*, vol. 117, no. 10, pp. 5101-5111, 2013.
- [48] F. Rietzler, M. Piermaier, A. Deyko, H.-P. Steinrück, and F. J. L. Maier, "Electrospray ionization deposition of ultrathin ionic liquid films: [C<sub>8</sub>C<sub>1</sub>Im] Cl and [C<sub>8</sub>C<sub>1</sub>Im] [Tf<sub>2</sub>N] on Au (111)," vol. 30, no. 4, pp. 1063-1071, 2014.
- [49] P. Nockemann, B. Thijs, S. Pittois, J. Thoen, C. Glorieux, K. V. Hecke, L. V. Meervelt, B. Kirchner, and K. Binnemans, "Task-specific ionic liquid for solubilizing metal oxides," *The Journal of Physical Chemistry B*, vol. 110, no. 42, pp. 20978-20992, 2006.
- [50] G. Sauerbrey, "Use of quartz crystals for weighing thin layers and for microweighing," *Magazine for physics*, vol. 155, no. 2, pp. 206-222, 1959.
- [51] K. R. Lovelock, A. Deyko, P. Licence, and R. G. Jones, "Vaporization of an ionic liquid near room temperature," *Physical Chemistry Chemical Physics*, vol. 12, no. 31, pp. 8893-8901, 2010.

- [52] K. C. Jha, H. Liu, M. R. Bockstaller, and H. Heinz, "Facet recognition and molecular ordering of ionic liquids on metal surfaces," *Journal of Physical Chemistry C*, vol. 117, no. 49, pp. 25969-25981, 2013.
- [53] Y. Lu, W. Chen, Y. Wang, F. Huo, L. Zhang, H. He, and S. Zhang, "A space-confined strategy toward large-area two-dimensional crystals of ionic liquid," *Physical Chemistry Chemical Physics*, vol. 22, no. 4, pp. 1820-1825, 2020.
- [54] S. Krischok, A. Ulbrich, T. Ikari, V. Kempter, M. Marschewski, O. Höfft, "Surface structure of [XMIIm] Tf<sub>2</sub>N ultrathin ionic liquid films probed by metastable He atoms and photoelectron spectroscopies (UPS and XPS)," *Nuclear Instruments and Methods in Physics Research Section B*, vol. 340, pp. 51-57, 2014.

# Chapter 4

Development of the Portable UHV Chamber

## Chapter 4: Development of the Portable UHV chamber

### 4.1 Introduction

In comparison to bulk materials, their surfaces and interfaces often exhibit different behavior. For molecular crystals, molecules in the bulk experience relatively isotropic force fields, compared to those at interfaces experiencing unbalanced forces, which results in differences in properties of bulk and surface regions. A detailed understanding of the surface phenomena of materials requires more than one technique. One of these phenomena has been discussed in Chapter 3, for an IL thin-film structural transition from an ordered nanofilm to a nonstructured one above the film thickness of  $\sim 10$  nm. It is vital to investigate the effect of additional overlayers on this structural transition for questions such as whether the additional layer causes the lower ones to lose their crystallinity or not. Studies of both sides of a nanofilm (IL/Vacuum and IL/substrate) are needed to have a better picture, which means that choosing suitable surface structural techniques is essential for detections from the top-most layer or the buried interface. A combination of different techniques is therefore advantageous for a consistent overall picture.

One of the powerful combinations to study the surface/interface structure is reflection high-energy electron diffraction (RHEED) and sum-frequency generation (SFG) spectroscopy. Both techniques are surface sensitive, while the main strength of this combination is the result of the complementary structural information, as discussed in Chapter 1. A portable UHV system is developed to bridge the two techniques instrumented in different laboratories and prevent exposure of samples to the ambient. The portable chamber is used to study the thickness-dependent structural phase transition of ILs combining the two techniques mentioned above. Although SFG is not a UHV-based technique, it is still beneficial to study samples in a UHV environment to maintain the desired experimental conditions.

Generally, there are two principal reasons in surface science to use the UHV environment. The first reason is to enable the preparation of atomically clean surfaces and maintain them in a contamination-free environment during the experiment. The second reason is to enable the possibility of using low-energy electrons- or ions-based techniques without concerns about gas-phase scattering interference. In the case of this experiment, the main reason to study the IL thickness-dependent structural transition is based on the first part; maintaining a contamination-free (or less contaminated) environment during the experiment.

One of the main factors to keep a sample clean during an experiment is the time it takes for a clean surface to get contaminated, which means, how long it takes for a certain adsorbate to build up on a specific surface. For a specific experimental condition (such as pressure and temperature), the number of incident molecules per unit area per unit time, called incident flux ( $F$ ), is estimated by a combination of ideal gas and Maxwell-Boltzmann gas velocity distribution, which leads to the Hertz-Knudsen formula

$$F = \frac{P}{\sqrt{2\pi mkT}} \text{ [molecules } m^{-2}s^{-1}\text{]}$$

With  $m$  (kg),  $k$  ( $J K^{-1}$ ),  $P$  ( $N m^{-2}$ ), and  $T$  (K) being the molecular mass, Boltzmann constant, pressure, and temperature, respectively. The molecular flux is directly proportional to the pressure. The fraction of the incident molecules on the surface that sticks to the surface is then related to the “sticking coefficient” ( $S$ ), related to many parameters, including surface coverage, temperature, and crystal facet. So now, it is possible to estimate how long it takes to cover a surface with a monolayer (ML) of an adsorbate. Some examples are shown in Table 4-1.

Table 4-1 The relation between pressure and the time a monolayer is created on a surface.

Pressure (Torr)	Gas Density (molecules $m^{-3}$ )	Time / ML (s)
760	$2 \times 10^{25}$	$10^{-9}$
$10^{-3}$	$3 \times 10^{19}$	$10^{-3}$
$10^{-6}$	$3 \times 10^{16}$	1
$10^{-10}$	$3 \times 10^{12}$	$10^4$

Most surface spectroscopy techniques can detect gas-phase molecules. In these situations, it is preferred that the number of the monolayer immediately above the surface is at least ten times the gas phase when analyzing a portion of a monolayer, which requires a minimum of  $10^{-4}$  torr. To keep a sample clean during an experiment, it is required to consider the time it takes for the surface to get contaminated and how long it takes to perform the experiment. This is one of the main motivations to perform experiments under UHV, even though the technique itself is not a UHV-based technique, such as the SFG spectroscopy for the PVD-deposited IL.

For the same reason of keeping the model sample clean during the experiment, UHV systems and high-pressure environments have been combined many times [1-3]. This combination enables the possibility of cleaning a sample surface in UHV, such as sputtering and annealing, and directly transferring the sample to another chamber to study the high-pressure conditions. The primary purpose of these studies was to bridge the gap between UHV and high-pressure environments to create a more realistic study on model catalysts, which was attempted by Somorjai and co-workers [4, 5], in which a high-pressure cell was constructed inside a UHV chamber.

It was shown in Chapter 3 that the thin film of the ILs on a solid substrate can be deposited using the physical vapor deposition (PVD) technique. Since a clean, thin-film free of contaminations needs a UHV environment, it is crucial to maintain the clean film during the transfer between different techniques. Surface vibrational spectroscopy can determine the chemical nature of adsorbates, and SFG is particularly sensitive to the adsorbate orientations. On the other hand, diffraction techniques are more potent in the determination of their crystal information. Combining these two types of techniques results in a detailed understanding of the adsorbate structures and creates the possibility of answering the question at the end of Chapter 3; Does the top layer of a molecular thin film affect the structure and orientations of the molecules underneath?

In this chapter, the details of the portable ultra-high vacuum (UHV) chamber are elaborated. What is discussed here is only the final design without discussing the failed or inefficient designs made during this project. All the materials for the portable chamber are selected to be UHV compatible since the main reason for developing this system is to maintain a UHV-level clean environment during sample transferring between different techniques. The chamber was designed in SolidWorks software, and it was made from scratch in the lab. The portable chamber has some additional accessories, including a transfer cart and an optical manipulator, briefly explained at the end of this chapter and in appendix (B).

## **4.2 Design Limitations**

Since the purpose of the portable chamber is to bridge two surface-sensitive techniques (RHEED and SFG), which are already fully developed and assembled in both labs, some pre-required parameters are restricting the chamber design. The limitations include dimension limitations, sample transfer type limitations, and many others. In this part, some of the main limitations are discussed, and the final design is elaborated.

### **4.2.1 Sample Transfer Type**

The first limitation is the type of sample transfer in the RHEED setup, the so-called “omicron-type” sample transfer. In this sample transfer mechanism, the transfer arm head, as is shown in Figure 4-1(B), has two pins and a sample plate grabber. To transfer the sample plate (Figure 4-1 (D)) to a sample receiver (Figure 4-1 (C)), as it is shown in Figure 4-1 (A), the two pins have to be inserted inside two holes to fix the transfer head. At this step, by rotating the other side of the transfer arm head, the sample plate will be disengaged from the transfer arm head and engaged on the receiver block. The omicron-type transfer mechanism made the shape of the sample receiver (sample car Figure 4-7 (A)), and the two holes for transfer arm pins engagement were necessary to consider in the design.

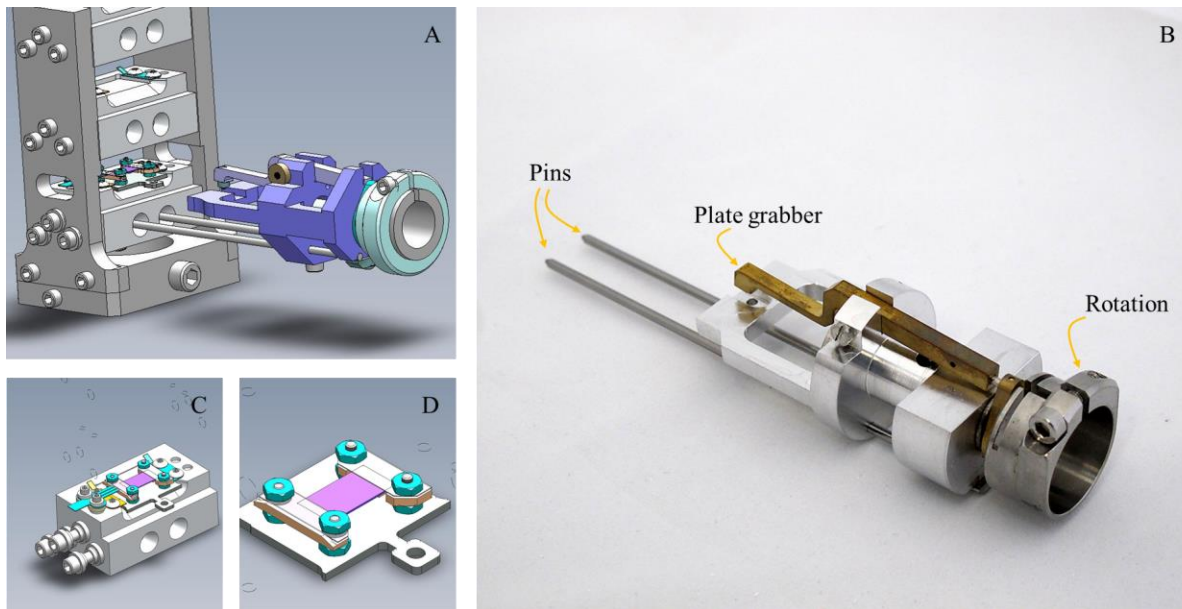


Figure 4-1 Omicron-type sample transfer (A) The commercial transfer head, the rotational sample stage/manipulator, and the two pins' engagement grab the omicron plate. (B) Three main parts of the transfer arm head (C) The sample stage block, with the omicron plate (D) The omicron plate with a sample.

### 4.2.2 SFG Optical Setup

To generate the SFG signal from the interface, two laser beams with a specific angle, as is discussed in chapter 2, must spatially and temporally overlap on the sample at a height ( $h$ ) of 6 inches, as is shown in Figure 4-2. So, from the bottom of the cell to where the sample is placed, the overall length must meet the height requirement. In addition to the height limitation, the input and output beams travel with a specific set of angles discussed previously. Due to the angle limitation, the viewports must have a minimum diameter, which is the input beams' angle difference,  $\Delta\theta$  (as shown in Figure 4-2). In addition, due to the dimensional limitations on the optical table, the portable chamber must be compact to meet all dimensional limitations.

### 4.3 Sample Transfer General Steps

In this section, an overview of the general layout of the RHEED experimental setup is presented, and the requirements enforced by the RHEED layout to the portable chamber are discussed. First, it is essential to

consider the overall steps which must be done to transfer a sample, in general, between the RHEED and SFG setups, prior to designing the portable chamber. Then, the general overview of the portable chamber and the details of each custom-made part are elaborated.

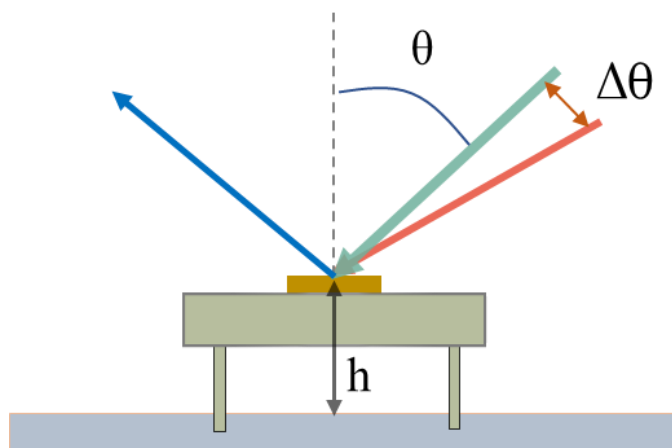


Figure 4-2 Height and angle limitation on the SFG setup. The two input beams arriving on the sample have different incident angles, and as a result, are separated from each other by more than 1 inch at the height where they reach the optical window of the chamber.

### 4.3.1 RHEED Setup

The overview of the RHEED setup is shown in Figure 4-3. It consists of three main chambers: IL deposition, LEED-Auger (sample preparation chamber), and diffraction chamber. In addition, there is a recently upgraded storage (load-lock) chamber, which is not shown here. The UHV setup facilitates the characterization of different types of materials, i.e., single crystals, polycrystalline materials, molecular thin films, and IL thin films., while the sample is still under the UHV environment. It is possible to load a sample in the UHV system quickly without breaking the vacuum of the whole system from the load-lock chamber, which is also meant for sample storage to keep up to eight samples inside the UHV setup. Generally, after a sample is assembled on the omicron plate, it is first loaded inside the UHV environment through the load-lock chamber, as is shown in Figure 4-3.

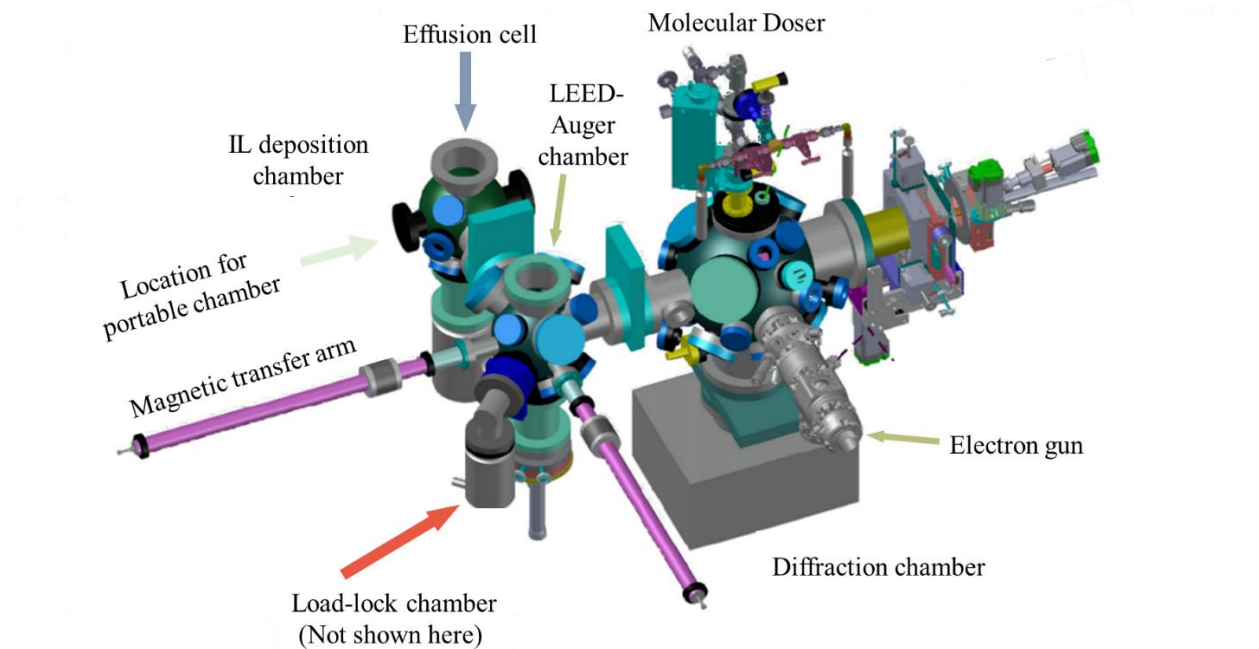


Figure 4-3 RHEED general setup and main parts. The portable chamber location is shown in the figure next to the IL chamber and 90 degrees rotated from the load-lock chamber.

The sample plate is transferred between other chambers using the omicron type transfer arm, as is discussed in Section 4.3.1. The sample can be then transferred directly to the main chamber, for the electron diffraction studies, or it can be first transferred to the ionic liquid chamber to deposit IL, and then transferred to the main chamber for further studies. In addition to the IL deposition, the RHEED setup is equipped with molecular doser, which add the possibility of depositing other molecules on solid substrates, such as water, ethanol, methanol, and acetonitrile.

#### 4.3.2 Position of the Portable Chamber

The only available port to transfer the sample to a portable chamber is on the IL chamber. The port is shown with the green arrow in Figure 4-3, which is another limitation for the portable chamber design enforced by the RHEED setup. Based on this configuration, as shown in Figure 4-4 (B), The sample must be transferred to the portable chamber through the ionic liquid chamber.

In an omicron-type transfer system, whenever one sample is transferred between two transfer arms (same as transfer arms 1 and 2 shown in Figure 4-5), there should be one place first to park the sample, rotate the sample to the other transfer arm. This parking stage is the same as the stage shown in Figure 4-1 (A).

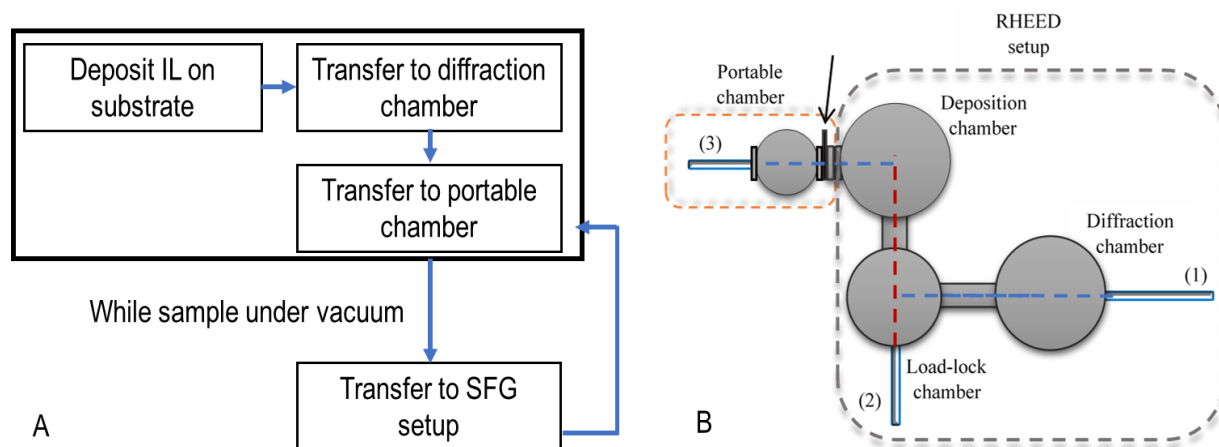


Figure 4-4 The position of the detachable portable chamber. The sequence of transferring a sample between the two setups is shown. Depending on the materials under study, the molecule is first deposited either in the main chamber or in the IL chamber. Then it is transferred to the main chamber for the desired experiments. Next, it is transferred to the portable chamber, which then the portable chamber is detached and transferred to SFG setup, and so on.

As a result of the abovementioned transfer steps, transferring the sample from the ionic liquid chamber to the portable chamber requires two transfer arms. In addition, one parking stage with the possibility of rotation is required. It was a critical limitation in the sample transfer design, and the rotatable parking stage had to be avoided for the following reasons. First, a rotatable stage like that is expensive, which is against the idea of making the design affordable for any lab. Moreover, adding a rotatable stage to the ionic liquid chamber was almost impossible since the design was not compatible with an additional bulky stage in the middle of the chamber. As a result, a new UHV transfer system compatible with the Omicron-type transfer head was developed. For this purpose, a custom-made detachable sample transfer car was designed, which at the same time has all the requirements to receive the sample from an omicron type transfer head (As is shown in Figure 4-7. The details are discussed in the next section.

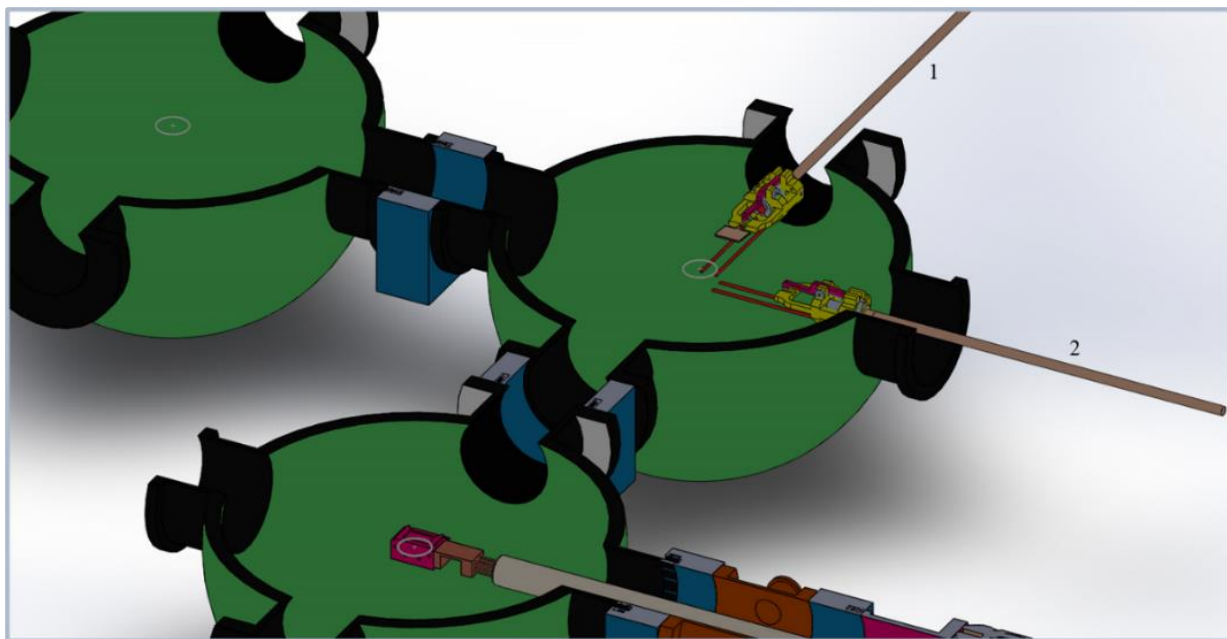


Figure 4-5 Sample transfer between two chambers with two separate transfer arms

#### 4.4 Portable Chamber Design

Figure 4-6 shows the schematic of the general layout of the portable chamber, the magnetic transfer arm, and the IL chamber altogether. The chamber design is composed of custom-made parts, personally designed, and made from scratch in the lab, which some of the main parts are discussed in this section. Among the custom parts, a new sample transfer method by modifying a bayonet-type locking, a custom-made sample transfer car, a custom-made viewport, and a custom-made sample receiver is designed, which is explained in detail in this section. The design is relatively simple to make in the lab, affordable, and compact, with heating, cooling, temperature measurement on the sample plate, and gas introduction. The chamber is pumped with a turbopump (Pfeiffer) in series with a mechanical pump to reach the pressures of  $2 \times 10^{-8}$  torr, while it is separated from the IL chamber, and  $5 \times 10^{-9}$  torr, when coupled with the IL chamber (Since the IL chamber base pressure is  $6 \times 10^{-10}$  torr). In addition, it is possible to purge the chamber with ultrapure  $N_2(g)$  to keep the sample under an inert gas environment during a sample transfer if required. In addition, the chamber is

equipped with a residual gas analyzer (RGA200), which is a powerful part to check a leak test, to be used for adsorbate purities, and in some cases for temperature-programmed desorption (TPD) measurements.

#### 4.4.1 Fully Assembled Portable Chamber

The actual portable chamber, assembled next to the IL chamber, is shown in appendix (B). To make a clear step-by-step explanation of the design, a schematic of the portable chamber while it is connected to the ionic liquid chamber is shown in Figure 4-6. Sample transfer from other chambers to the portable chamber is discussed in the next section.

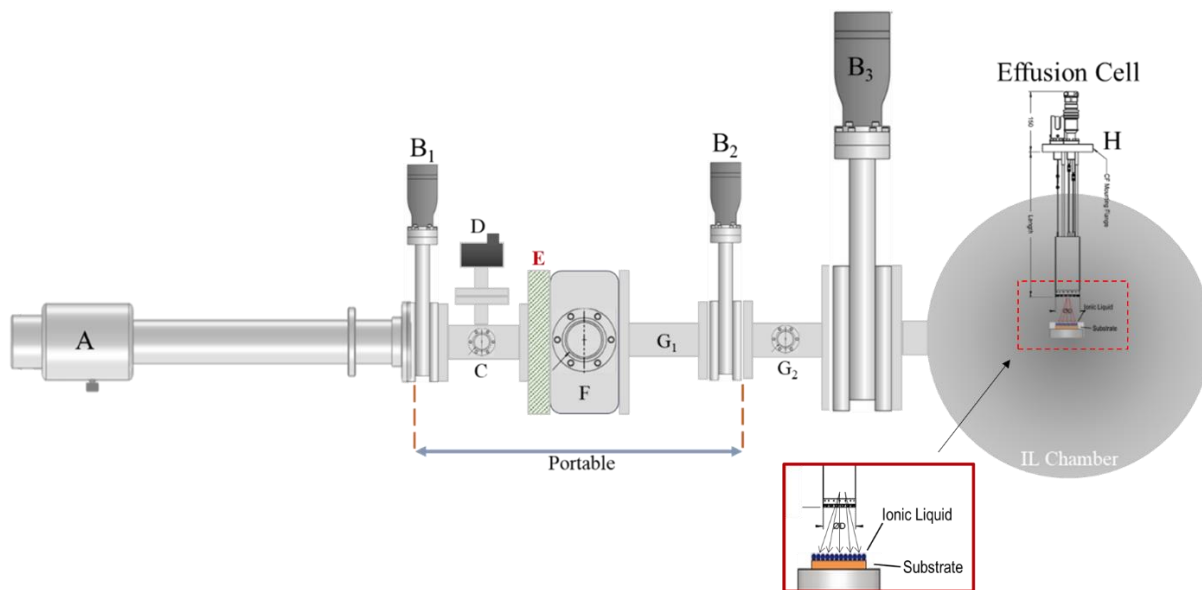


Figure 4-6 Schematic side view of the portable chamber assembled on the ionic liquid chamber including (A) magnetic coupled transfer arm, (B1) and (B2) 2.75" gate valve, (B3) 4.5" gate valve, (C) custom-made Tee, (D) residual gas analyzer (RGA), (E) custom-made sample receiver, (F) spherical compact chamber with 4-2.75" ports, (G1) and (G2) reducer nipples, (H) Effusion cell and relative position with the sample inside the IL chamber.

#### 4.4.2 Step-by-Step Sample Transfer

After the deposition of the ionic liquid on the substrate, or other molecules using molecular doser setup, the sample is transferred to the portable chamber using the custom-designed sample transfer head (Figure 4-7 (D)) and sample car (Figure 4-7 (A)). The details are explained in the next section.

To transfer the sample (which is assembled on the omicron plate - Figure 4-1 (D)) from the IL chamber to the portable chamber, first the omicron plate containing the sample is transferred to the sample car using transfer arm 1 shown in Figure 4-5. while the omicron plate is transferred to the sample car, the other transfer arm which carries the sample car is retracted back (as is shown in Figure 4-8) inside the portable chamber. Then, when the sample car is on the custom-made sample receiver position (Figure 4-6 (E)), it is disengaged by a rotation from the transfer arm head and engaged on the sample receiver, as is shown in Figure 4-8 schematically.

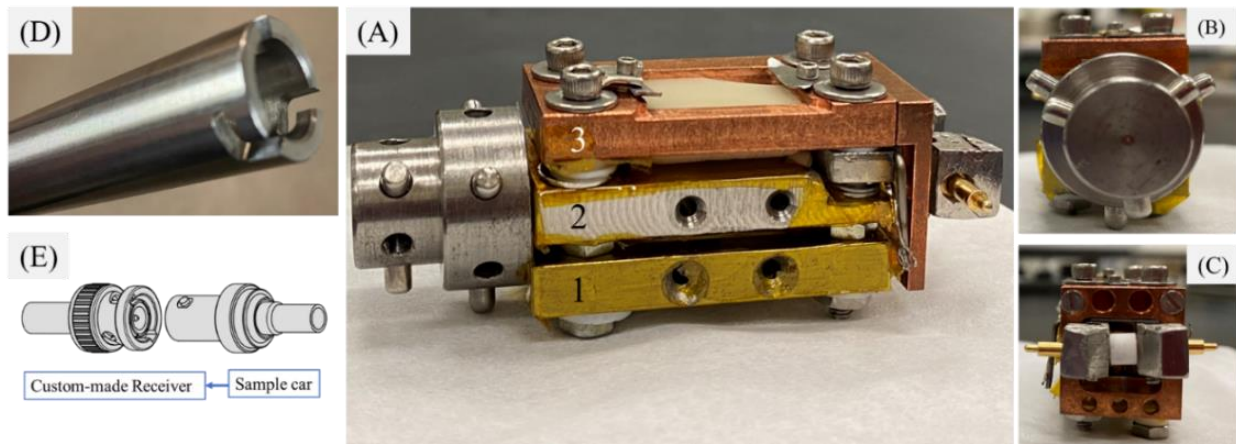


Figure 4-7 Sample car design and the transfer arm head. (A) Fully assembled sample car. (B) back view of the sample car with three pins on each cylindrical section for engagement to the custom-made sample receiver, as is discussed in section 1212. (C) front view of the sample car with the two spring-loaded pins for electrical connections. (D) The transfer arm's head is designed corresponding to the sample car pins, shown in the back view of the sample car in part (B) of this image. (E) The Bayonet type cable connection, which is the origin of the idea of the sample transfer.

As a result of this procedure, the sample car carrying the sample is engaged on the sample receiver, and the transfer arm is disengaged from the sample car. At this step, after disconnecting the transfer arm, the gate valves  $B_1$  and  $B_2$  are closed, keeping the portable part under vacuum. The details of the purging steps are discussed in appendix (B).

### 4.4.3 Sample Car Bayonet Connection

The sample car (sample holder) is the most complex and crucial part of the chamber design. In any complex UHV system, the sample transfer must be smooth and relatively fast between different systems. In addition, it is also essential to design the sample holder in a way that the sample transfer is repeatable.

In addition to the abovementioned requirements for a sample holder/sample car, there are other requirements specified in designing the sample car for the portable chamber to be compatible with the RHEED sample transfer design. The idea of engagement and disengagement of the sample car is based on a modification of bayonet-type cable connections (as is shown in Figure 4-7 (E)). A bayonet-type cable connection is a locking mechanism including a male part with a small radial pin and a female part with a spring-loaded L-shaped receptor which locks the two parts by a rotation and a force from the springs.

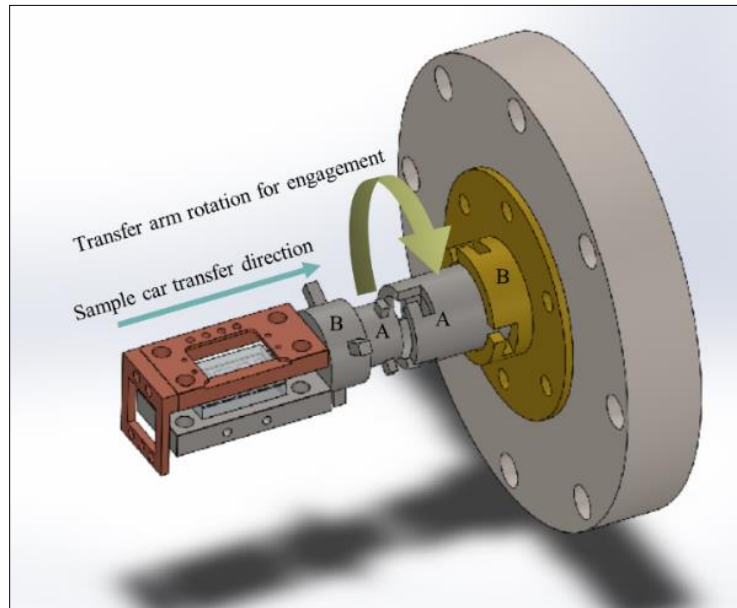


Figure 4-8 Sample car engagement. The B-B section: the two parts which engage and disengage for transferring the sample car to the sample receiver. The A-A section: the two parts which engage and disengage for transferring the sample car to the IL chamber and on the transfer arm head.

The sample car transfer and the engagement/disengagement procedure are designed by modifying the bayonet locking principle, which the overall layout is shown in Figure 4-7 (A, B, and C). The back view

of the transfer car (Figure 4-7 (B)) shows two concentric cylindrical sections, with three pins on each cylinder. For each set of the pins on one cylinder, there is a corresponding L-shaped receptor on the custom-made sample receiver (Which is placed on position E, as is shown in Figure 4-6 (E), and the actual image is shown in appendix (B)). The smaller diameter cylinder is for the engagement of the sample car to the transfer arm head (A-A connection in Figure 4-8), and the bigger diameter cylinder is for the engagement of the sample car to the sample receiver (B-B connection in Figure 4-8). A simple rotation is involved in each engagement/disengagement step, which is an effective and easy method embedded in this design. As a result, by first rotation, the A-A section is disengaged, and then the B-B section is engaged, leaving the sample car attached to the sample receiver and transfer arm detached from the sample receiver. Then the reverse procedure results in the engagement of the sample car to the transfer arm and disengagement from the sample receiver. The transfer arm can then be used to transfer the sample back into the RHEED setup.

#### **4.4.4 Sample Car Details**

The sample car itself is designed with accurate dimensions to match multiple parts during the engagement-disengagement procedure, including electrical connections, thermal connections to the cold finger, and the thermocouple connection for temperature measurements. In addition to the bayonet-type connection, the sample car has three primary levels, as is shown in Figure 4-7 (A) with numbers 1 to 3. The first level is the base, which everything else is assembled on it. The second level is the height adjustment level to align the two holes level with the transfer arm pins for engagement of pins. Finally, the topmost level is where the omicron plate slides in. The top-level is made from copper for its high thermal conductivity for better temperature control. Each level is entirely isolated electrically and thermally from each other and the chamber body with ceramics. The schematic of each layer of the sample car is shown in Figure 4-9. (More details in appendix (B)).

The choice of sample heating for the sample car is resistive heating since it is easier to modify for a moveable heater. The heating stage, embedded between the topmost and second layers, comprises a gauge 28 nichrome wire with  $2.6 \Omega$  resistivity inserted inside a Macor ceramic. The ceramic thermally and electrically isolates the heater from the rest of the parts except the top surface, which is mechanically in contact with the Omicron plate. The top surface is made from boron nitride ceramic, which has good thermal conductivity and acts as the heating stage in contact with the omicron plate. The calibration curves for the resistive heater are shown in Figure 4-10.

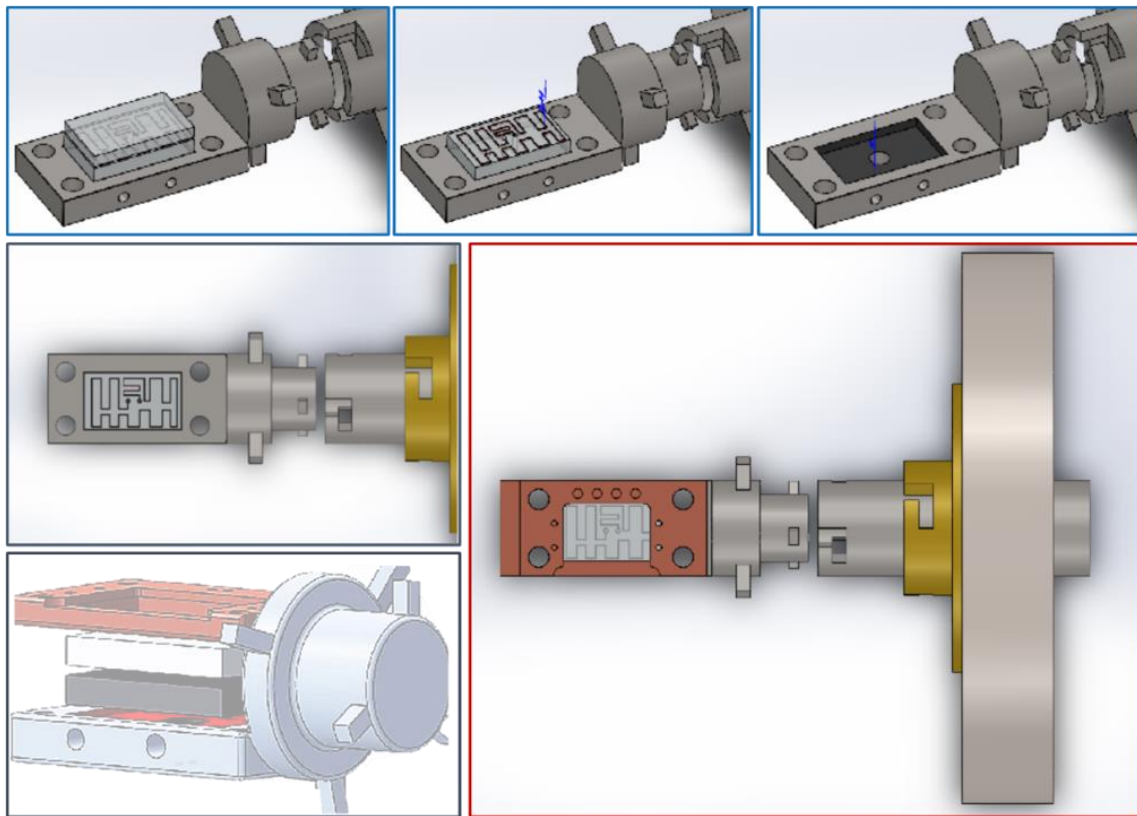


Figure 4-9 The overview of the sample car layers.

The temperature of the sample is measured by a K-type thermocouple which is in contact with the omicron plate. Some examples of the heating rates are shown in Figure 4-11. The heater is tested up to 700 °C. The cooling rate on the sample plate is slow, as is shown in Figure 4-12, for two major issues. First, from the cold finger to the sample plate, there are two mechanical connections, one from the cold finger to the

spring-loaded copper connection, connected using a braided copper. The second step is from the spring-loaded copper to the omicron plate. Two mechanical connection dramatically reduces the cooling rate. The third reason is that the cross-section of the spring-loaded copper part and the sample plate copper section, and the cold finger itself are small, almost 5 mm by 10 mm rectangular section. A bigger cold finger and a direct connection from the cold finger to the sample stage copper section can improve the cooling rate.

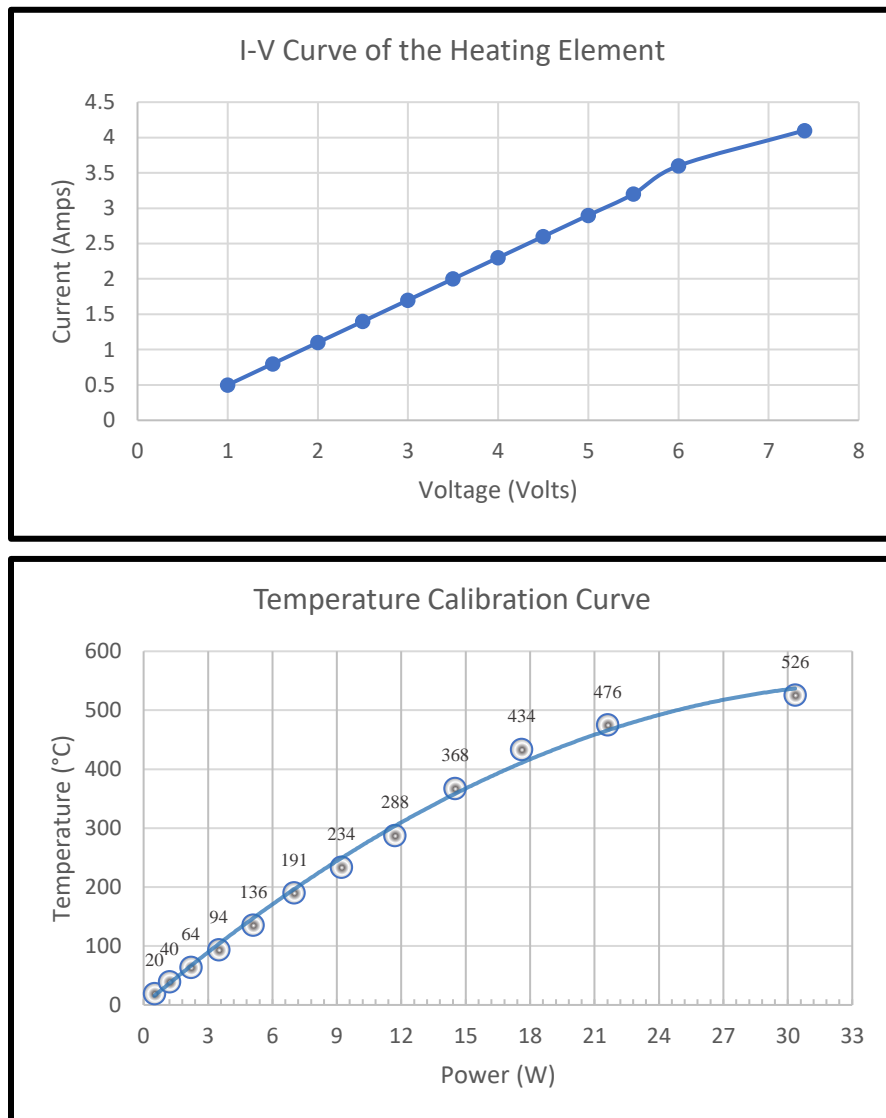


Figure 4-10 Calibration curves for the resistive heater.

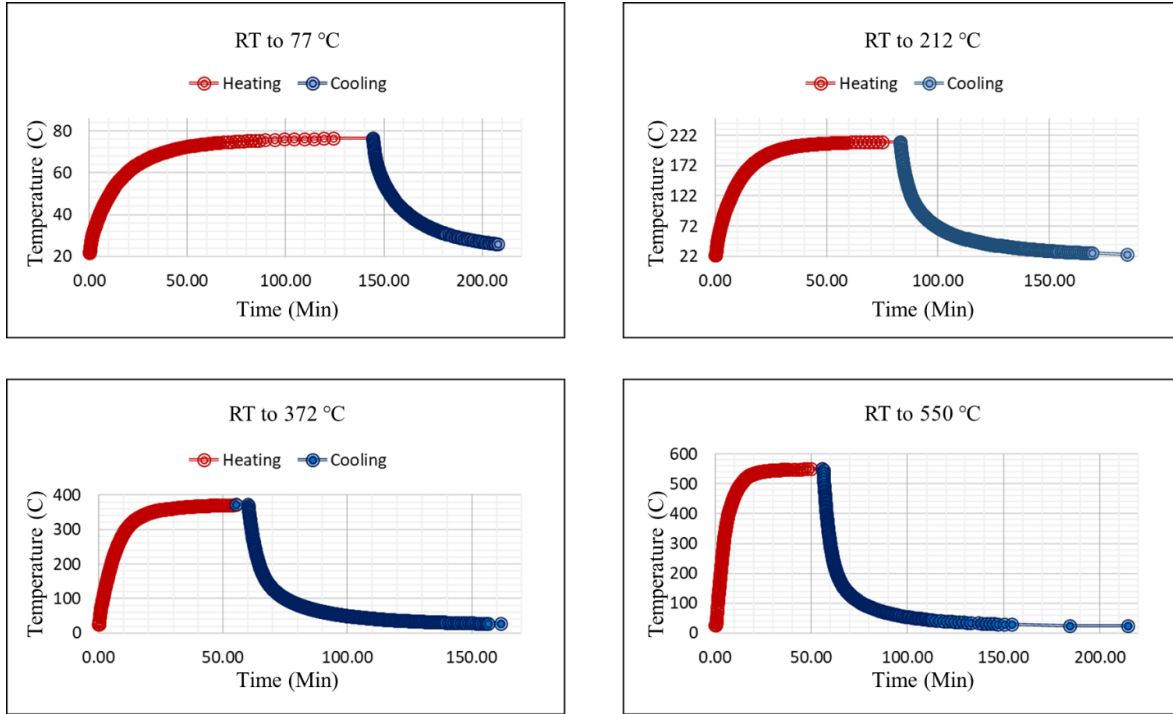


Figure 4-11 Heating and natural cooling curves

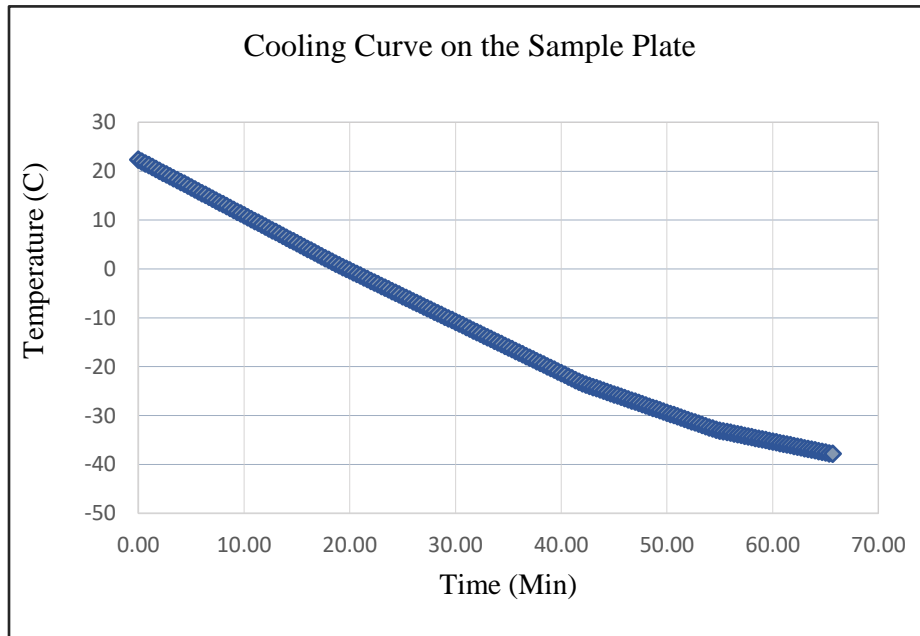


Figure 4-12 The cooling rate of the sample plate for the portable chamber.

#### **4.4.5 Custom-Made Sample Receiver**

The sample car, discussed in Section 4.4.4, is parked on the custom-made sample receiver, which is located on a 4.5" CF flange on the portable chamber. The port containing the sample receiver is located on a flange shown in Figure 4-6 with a dashed green color line and is labeled with a red color letter E. The sample receiver is the corresponding bayonet-type female connection of the sample car's bayonet male connection. The sample car has a male-type bayonet shape, while the sample receiver has a female-type bayonet connection. It is schematically shown in Figure 4-8 and Figure 4-9 with a yellow color. The actual part is shown in appendix (B). The female bayonet sample receiver is the fixed part of the transfer system, and the sample car which carries the sample is the moveable part.

#### **4.4.6 Optical Window Design**

When the sample car is transferred to the portable chamber, the three gate valves B<sub>1</sub>, B<sub>2</sub>, and B<sub>3</sub> are closed (Shown in Figure 4-6), and the portable chamber is transferred to the SFG optical setup.

One of the parameters enforced by the SFG setup was the angle of the two incident beams and the output SFG beam. Unfortunately, the commercial optical windows were not suitable for the angle difference between the two input beams. As a result, a custom-made window was designed and built in the lab to solve the problem. Figure 4-14 shows the optical window, which was designed for the portable chamber, consisting of 5 pieces, as shown in the top-left of the image. The layers are: (1) the base of the window, with a groove (red section) inside for the Viton O-ring, (2) the Viton O-ring seal (3) CaF<sub>2</sub> window (4) second Viton O-ring (5) the top stainless steel to sandwich all parts together.

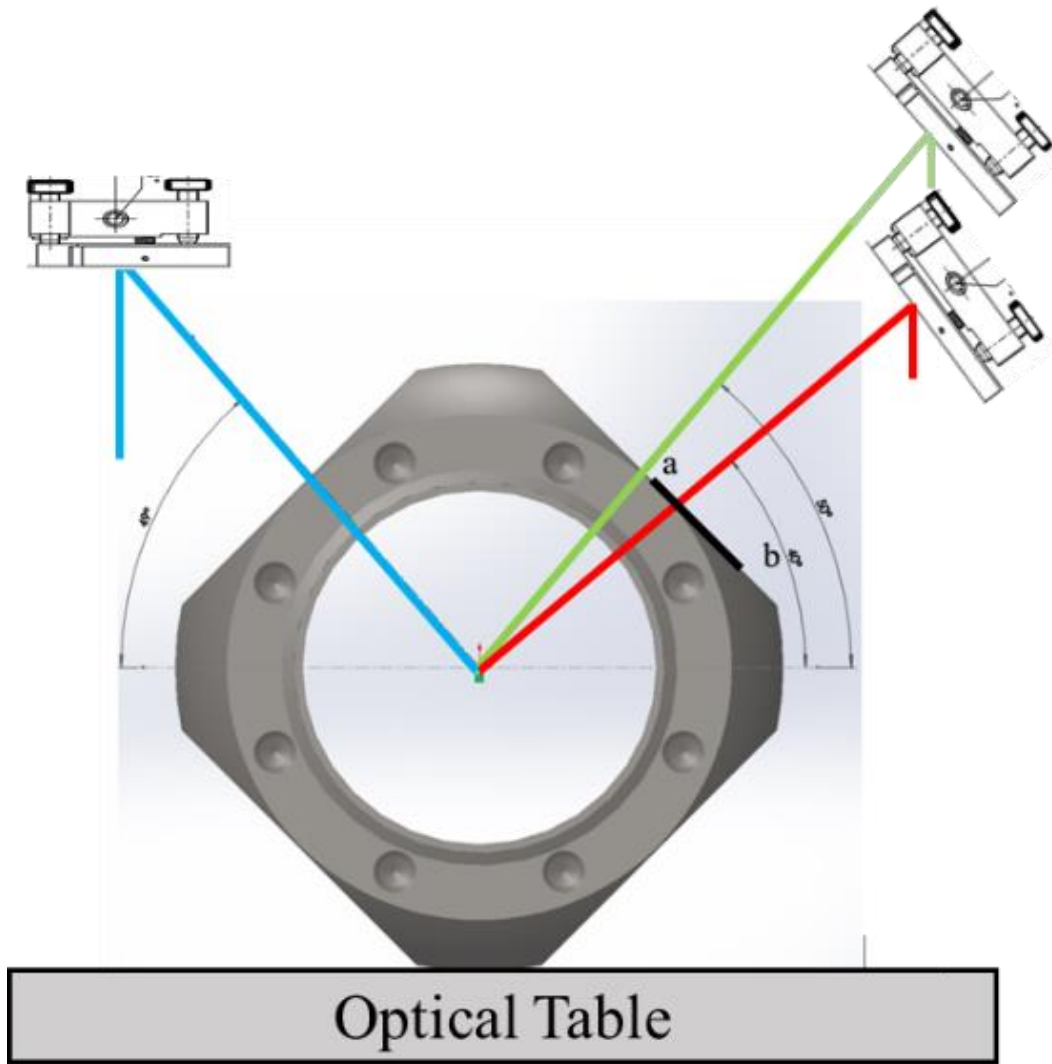


Figure 4-13 The portable chamber side view with the two input laser beams and the SFG output beam

The two cross-sections from Figure 4-14 (d) are shown in parts (e) and (f). It is shown along section a-a of the window. The holes are tapped holes to assemble the top layer on the base of the window, while section b-b of the window shows through holes meant to assemble the whole optical window on the portable chamber port. In addition, the CaF<sub>2</sub> window sits on the Viton O-ring, which is shown with a green and red color. The 3D view of part (e) is shown in part (b) and for the part (f) in part (c) for better visualization of the design.

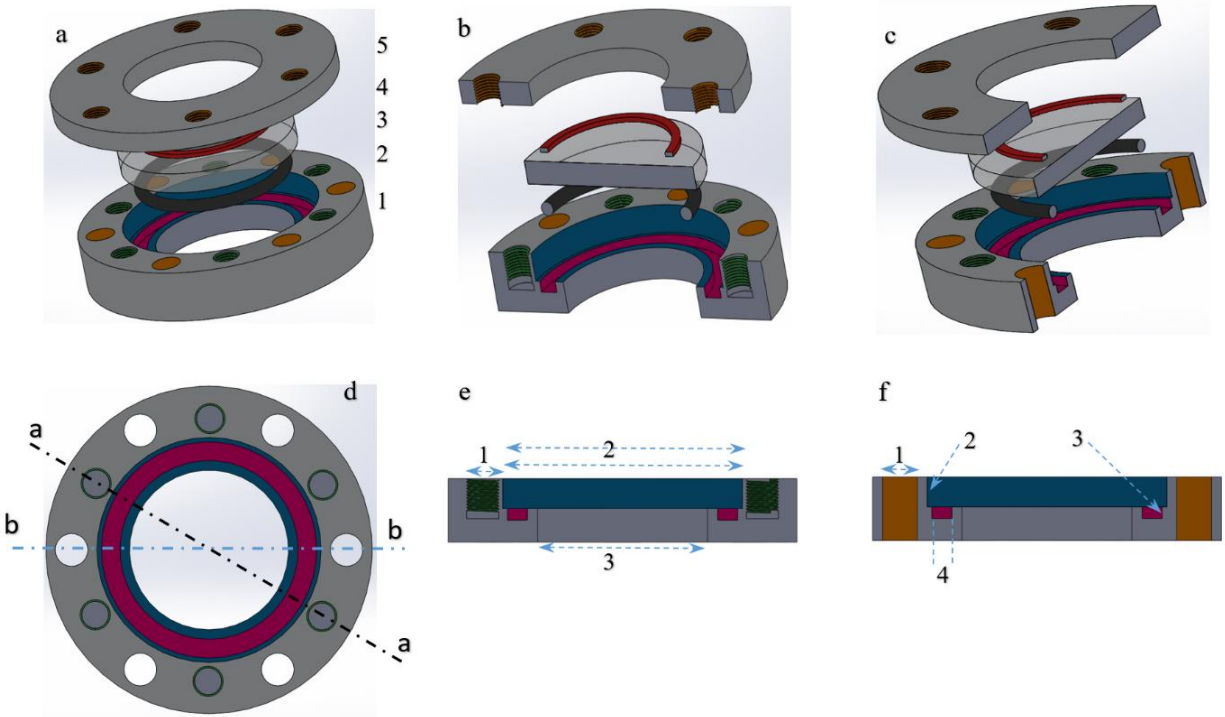


Figure 4-14 The layout of the custom-made viewport for the portable chamber

## 4.5 Conclusion

In this chapter, the details of a portable chamber were discussed. The chamber consists of many other versions, useable for future developments, which have not been shown or discussed here. The possibility for future experiments with bridging SFG and RHEED is now possible.

## 4.6 Bibliography

- [1] S. Liu, A.-a. Liu, R. Zhang, and Z. Ren, "Compact ultrahigh vacuum/high-pressure system for broadband infrared sum frequency generation vibrational spectroscopy studies," *Review of Scientific Instruments*, vol. 87, no. 4, p. 044101, 2016.
- [2] M. Morkel, G. Rupprechter, and H.-J. Freund, "Ultrahigh vacuum and high-pressure coadsorption of CO and H<sub>2</sub> on Pd (111): A combined SFG, TDS, and LEED study," *The Journal of Chemical Physics*, vol. 119, no. 20, pp. 10853-10866, 2003.
- [3] H. Unterhalt, G. Rupprechter, and H.-J. Freund, "Vibrational sum-frequency spectroscopy on Pd (111) and supported Pd nanoparticles: CO adsorption from ultrahigh vacuum to atmospheric pressure," *The Journal of Physical Chemistry B*, vol. 106, no. 2, pp. 356-367, 2002.
- [4] G. A. Somorjai, "Modern surface science and surface technologies: an introduction," *Chemical Reviews*, vol. 96, no. 4, pp. 1223-1236, 1996.
- [5] D. Blakely, E. Kozak, B. Sexton, and G. Somorjai, "New instrumentation and techniques to monitor chemical surface reactions on single crystals over a wide pressure range ( $10^{-8}$ – $10^5$  Torr) in the same apparatus," *Journal of Vacuum Science and Technology*, vol. 13, no. 5, pp. 1091-1096, 1976.

# Chapter 5

Rubrene

## Chapter 5: Surface Structure Analysis of Rubrene Single Crystals

This chapter is collaborative research with my labmate, Alamdar Shah. Some parts of the SFG analysis section are added from his Ph.D. thesis with his permission for clarity and consistency since the chapter aims to combine RHEED and SFG experiments. All other SFG parts of the chapter were conducted with equal contribution.

### 5.1 Introduction

Rubrene is one of the leading organic semiconductors in scientific and industrial research, showing good conductivities and utilities in devices such as LED displays [1-10] and organic field-effect transistors [11-15]. In these applications, the rubrene crystals are often in contact with ionic liquids and other materials. Consequently, their surface properties and interfacial interactions influence the device's performance. Although rubrene has been extensively studied with multiple structure characterization techniques, a complete description of molecular orientation and arrangement for rubrene single-crystal surfaces remains elusive. This study focuses on analyzing molecular orientation and arrangement on the surface of rubrene single crystals with Sum Frequency Generation (SFG) spectroscopy and Reflection High-Energy Electron Diffraction (RHEED), respectively.

Organic semiconductors have gained special attention as the key materials for developing innovative scientific and industrial applications, such as flexible displays, electronics, and wearable devices [1-5]. Rubrene (5,6,11,12-tetraphenylnaphthacene), is one of the main components of high performance organic field-effect transistors (OFETs), photovoltaics [6-10], and light-emitting diodes [11-14, 16, 17]. Furthermore, its high fluorescence quantum yield makes it favorable for constructing organic light-emitting diodes. The high carrier mobility exhibited by good quality rubrene single crystals, with orthorhombic structure, has made this material an efficient and attractive component for many transistor-based systems [18, 19]. As a result,

rubrene single crystals have been the subject of multiple scientific studies, which have characterized their atomic, molecular, and electronic structures and optical qualities [18-28].

Multiple surface-sensitive applications of the rubrene crystals, such as photovoltaics and transistors, necessitates the importance of surface structure in device performances. Surfaces usually have unique properties compared to their bulk. Complex applications, such as the OFET devices, are extensively attached to the fundamental knowledge about the material properties, including their surface properties, where surface characterization becomes essential. For example, in field-effect transistors (FETs), rubrene single crystal is often in contact with dielectrics such as Ionic Liquids (ILs). The complex interaction between the IL and the rubrene crystal surface can affect the charge transfer, thus influencing the device's performance [29].

However, despite tremendous academic and industrial interest, the surface molecular orientation and arrangement of rubrene single crystals are not well understood. The studies have either been surface selective such as atomic-force microscopy (AFM), scanning tunneling microscopy (STM), and X-Ray diffraction (XRD) [30-34]; or chemically sensitive (XPS, IR, Raman) [35-39]. Therefore, the surface characterization of rubrene single crystals with chemically sensitive and surface selective techniques is beneficial.

In this chapter, two complementary surface-specific techniques, sum-frequency generation (SFG) and reflection high-energy electron diffraction (RHEED), have been used to understand the rubrene single crystal's interface structure without bulk contributions. Using these two techniques makes it possible to have more detailed knowledge about the arrangement (RHEED data) and orientation (SFG data) of the molecules, specifically on the surface.

## **5.2 Experimental**

### **5.2.1 Rubrene Single Crystal**

The rubrene molecule is a centrosymmetric molecule with a  $C_{2h}$  symmetry group [40]. It consists of a tetracene backbone and four phenyl rings attached to each side of the two central rings of the backbone, as

is shown in Figure 5-1, with the molecular axis L, M, and N [40]. The N axis is perpendicular to the tetracene plane.

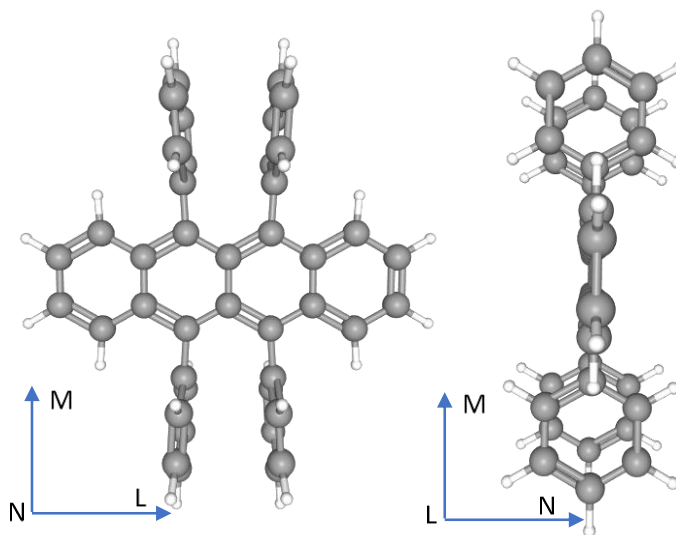


Figure 5-1 Molecular structure of rubrene. L, M, and N represent the three molecular axes.

The samples provided by Dr. Okaue Daijiro, from Surface-Interface Lab, Fukui Group, Osaka University, were prepared by a vapor-transport method. In this process, high-quality rubrene is placed on one side of a two-zone furnace, and the vaporized rubrene is then transferred to the cooler side by an inert gas flowing from the hot side to the cooler side of the furnace. The flow rate and temperature gradient along the two zones are essential for a high-quality crystal. The condensed crystal is then made with a reddish-orange or color, with orthorhombic symmetry [41], with the b axis being the longest crystal growth (fastest) and the c axis the shortest (slowest). In the ab-plane, the molecules are packed in a herringbone pattern [42, 43]. The actual rubrene single crystal is shown in Figure 5-2 on the right.

The sample thickness was about 20  $\mu\text{m}$ , with a 2.5 mm  $\times$  1.5 mm semi-rectangular surface. To identify the a- and b-axis of the sample, a light-polarized UV-vis spectroscopy was performed while the sample was azimuthally rotated from the shorter in-plane length to the longest in-plane dimension of the crystal. The absorption along the three-axis follows  $A_a > A_b > A_c$ ; therefore, the a- and b-axis are assigned based

on reported data about the crystal [40]. The absorption profiles shown in Figure 5-2 indicate the direction of the a and b molecular axis with the actual dimensions of the crystal, which is also shown in Figure 5-6 (right) [40-44].

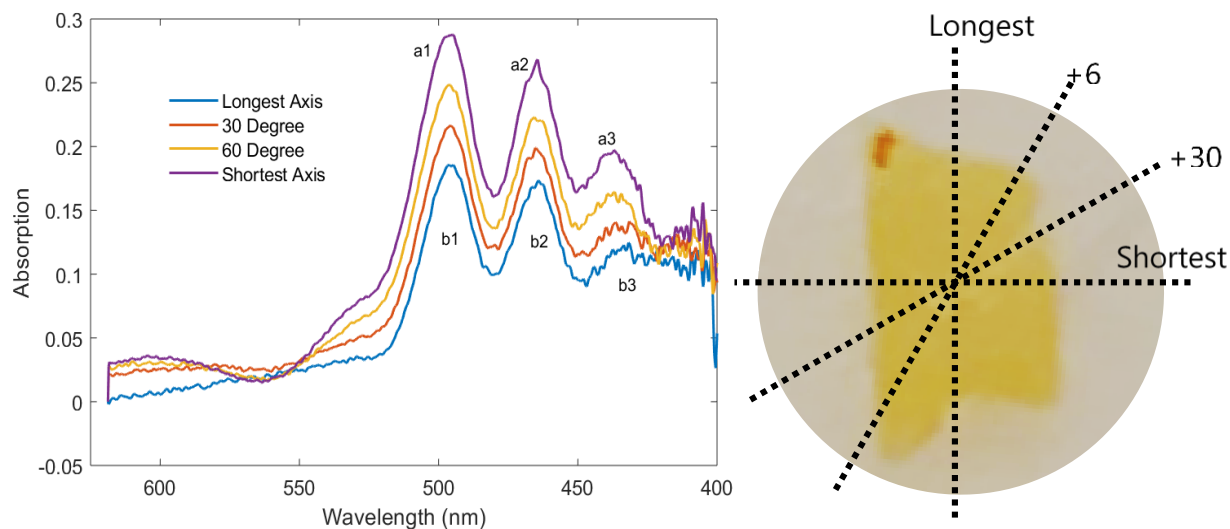


Figure 5-2 Rubrene single crystal and its absorption spectrum along 4 different dotted lines.

## 5.3 RHEED and SFG Data

### 5.3.1 RHEED Data

To study the molecular orientations of the molecules with SFG, it is required to understand the relative relation of the molecular coordinates and the lab-coordinate systems, which is one of the early steps of SFG data analysis. In this study, to link the molecular orientation of the surface molecules to the unit cell parameters of the rubrene single crystal, the sample is studied first by RHEED to create a relation between unit cell parameters and the lab-coordinate system. As a result, it is possible to create a complete relation between the unit cell parameters, molecular orientations, and the lab-coordinate system. Furthermore, the RHEED data provide a precise surface structure, making it possible to look for any surface reconstruction. In the case of the rubrene samples in this work, no surface reconstruction was observed.

The diffraction patterns were recorded at grazing incidence angle ( $\sim 1^\circ$ ) with respect to the (001) surface of the rubrene single crystal, with the azimuthal rotation of  $60^\circ$ . Six symmetric patterns were recorded in the first azimuthal range of the experiment, as shown in Figure 5-3, corresponding to different zones of the (001) surface of the crystal. All peaks are fitted to the Lorentzian function, and the vertical/horizontal distances are calculated using the best-fit parameters of all peaks. The main features of the diffraction pattern giving the in-plane lattice parameters are in good agreement with the previously reported values. The distances and corresponding planes are indexed as shown in Figure 5-3, and Table 5-1.

Table 5-1: RHEED analysis of the single crystal rubrene surface performed along different surface indices

$(hk)$ in-plane Index	(31)	(21)	(32)	(11)	(23)	(13)
From fitting ( $\text{\AA}$ )	3.98	5.19	2.88	6.36	2.26	2.33
Theoretical ( $\text{\AA}$ )	3.99	5.09	2.86	6.44	2.27	2.36
Deviation %	+0.2	-1.9	+0.7	+1.2	+0.4	+1.3

The values of the fitted peaks are in good agreement with the theoretical values, giving in-plane lattice parameters of  $a = 7.1 \text{ \AA}$  and  $b = 14.4 \text{ \AA}$  by using the diffraction patterns with well-defined streaks. (Using the (32) planes, the values will be slightly different,  $a = 7.21 \text{ \AA}$  and  $b = 14.37 \text{ \AA}$ ).

As a result of the initial analysis of the RHEED data, the a-b plane (in-plane) is parallel to the lab-coordinate X-Y plane. In addition, the c axis of the crystal is along the surface normal, parallel to the Z-axis of the lab-coordinate system (the (001) surface of the crystal is probed). The rocking curve analysis is used to measure the vertical lattice parameter (c axis), which is discussed in detail in Chapter 2. To avoid any surface property, like surface potential, affecting the vertical peak positions, the higher orders, shown by yellow arrows, were selected, and fitted with Lorentzian peak shape to get the horizontal spacings.

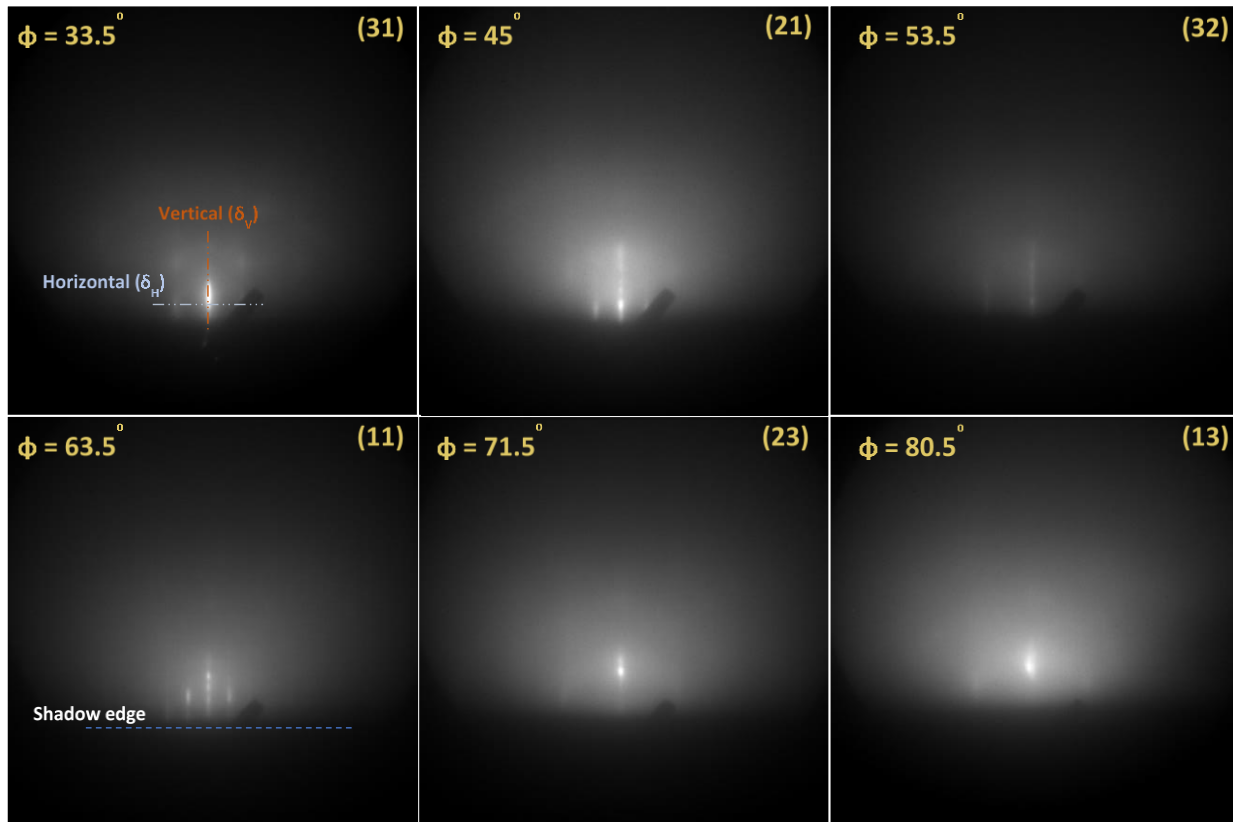


Figure 5-3 RHEED patterns of six selected zone axes to determine the surface arrangement of the molecules. The first step of the SFG analysis for orientation determination requires a good understanding of the relation between unit cell parameters ( $a$   $b$   $c$ ) and the lab coordinates ( $X$   $Y$   $Z$ ) determined by the RHEED technique.

From the best parameters, a value of  $13.41 \pm 0.065 \text{ \AA}$  is measured. As shown in Figure 5-4, this spacing is related to  $c/2$  spacing, corresponding to (002) planes, which results in a vertical lattice parameter of  $26.82 \text{ \AA}$ , which is also in good agreement with previously reported values [42, 43].

It is worth noting that the streak-like diffraction patterns are a sign of smooth surface, atomically flat, or steps with large surfaces, ordered in  $a$ - $b$  plane. However, transmission-like diffraction spots along the surface normal [001] of the crystal can be a result of 3D-crystals, with nanometer size, or the step layers growing along the vertical direction.

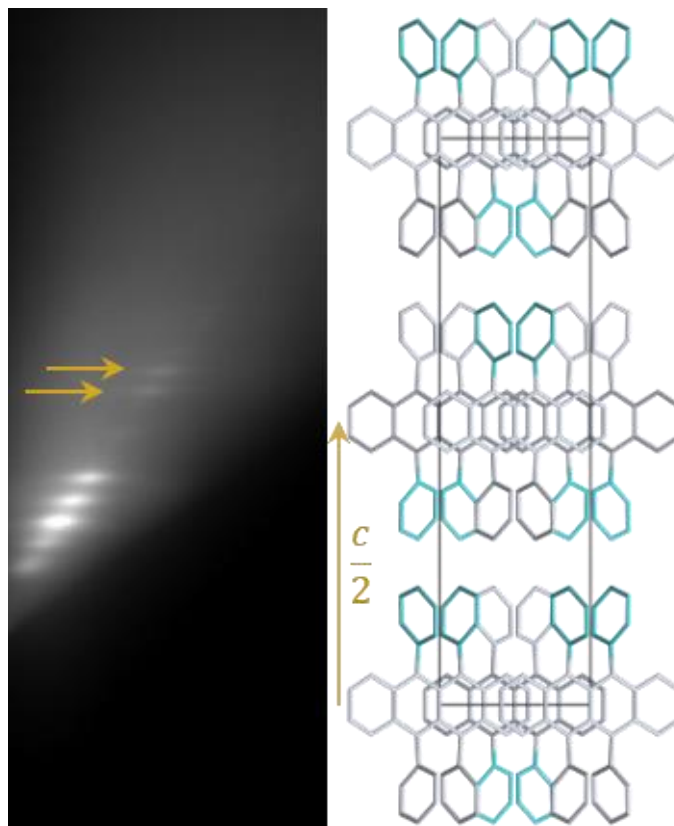


Figure 5-4 Rocking curve of the rubrene crystal. The vertical lattice parameter corresponds to (002) planes, giving  $c/2$  spacing. The two different sets of peaks show slightly different values due to surface properties affecting the incident electrons along the vertical axis.

AFM studies reported stepwise packing along the vertical direction for rubrene crystals. In the rubrene crystal in this experiment, with a new crystallization procedure, the steps are also observed in AFM [33]. Different scenarios, including one molecular layer, two molecular layers, one-molecule steps with different domain sizes, are considered and simulated to find the relation of the crystal structure along the  $c$ -direction (vertical direction) with the chopped streak pattern observed in the diffraction patterns.

The results of the diffraction simulation for two azimuthal angles and three scenarios are compared with the corresponding actual diffraction pattern, as is shown in Figure 5-5. The simulation results resemble case b, which shows diffraction from a stepwise rubrene, confirming the stepwise layers of the rubrene sample.

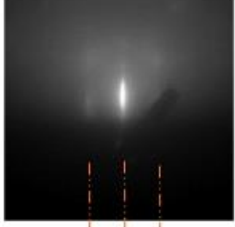
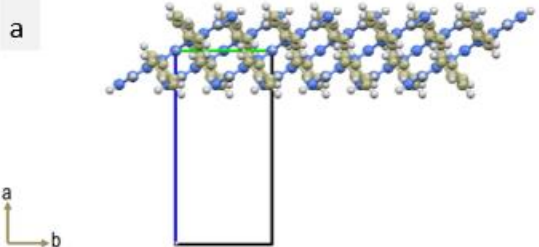
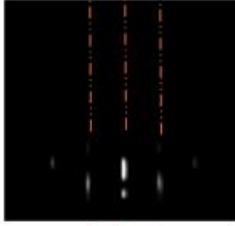
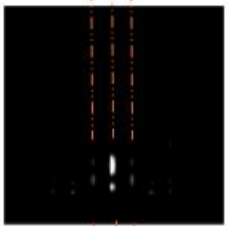
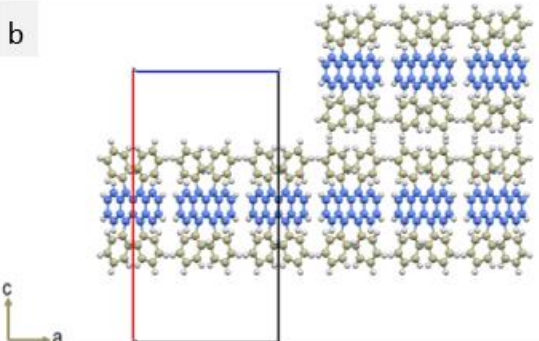
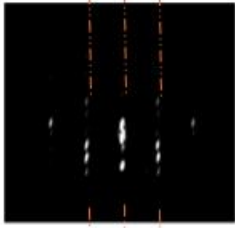
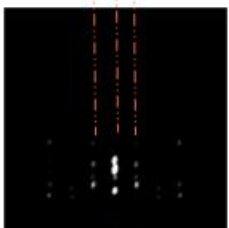
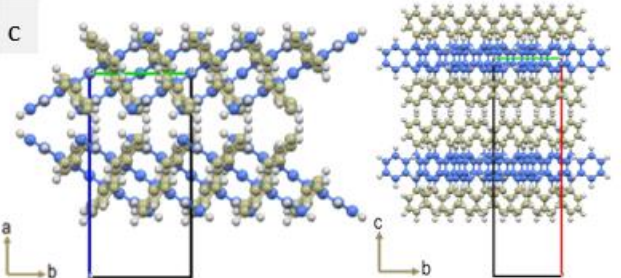
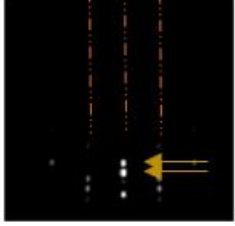
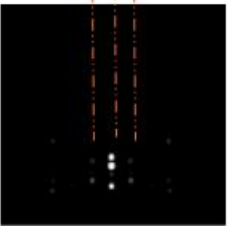
Crystal structure considered in simulations	Simulation (31) $\phi = 33.5^\circ$	Simulation (11) $\phi = 63.5^\circ$
		
<p>a</p> 		
<p>b</p> 		
<p>c</p> 		

Figure 5-5 The three scenarios of the rubrene single crystal surface and their corresponding diffraction features. Case b with a stepwise surface is similar to the actual diffraction patterns in two randomly selected azimuthal angles.

So, the surface of the rubrene crystal does not show surface reconstruction, the lattice parameters are measured, and the orientation of the unit cell is now defined with respect to the SFG laboratory system, which is required to make more quantitative analysis on the SFG results to get molecular information about the surface of the rubrene single crystals.

### 5.3.2 SFG Data

The rubrene crystal was placed in a Teflon cell sandwiched with a 1 inch diameter, 1 mm thick calcium fluoride window, shown in Figure 5-6, to purge the cell with ultrapure nitrogen, and the intensity of the visible beam was kept at a minimum to prevent rubrene photo-oxidation [45, 46]. Also, the rubrene sample can be azimuthally rotated in the sample plane with 1° precision.

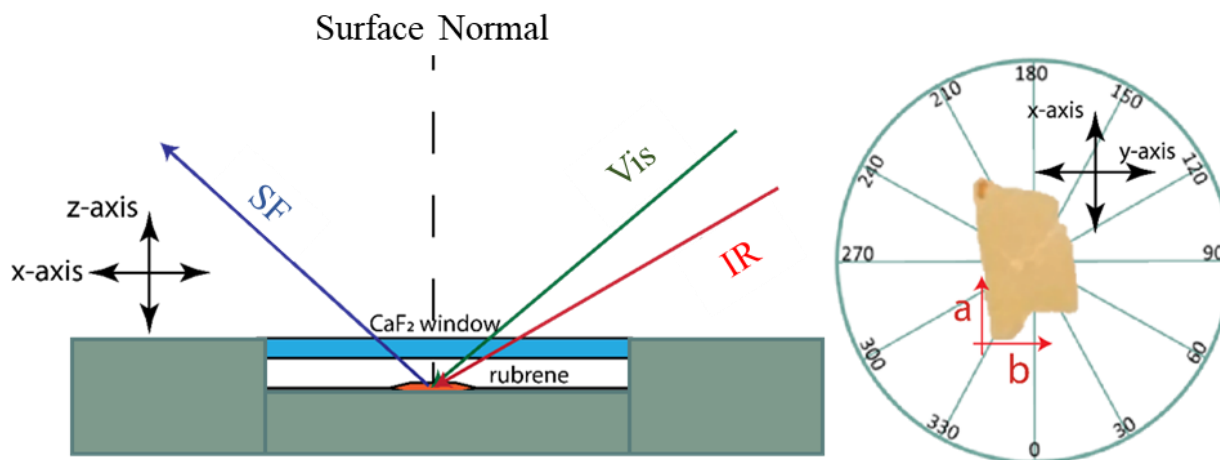


Figure 5-6 Experimental cell and SFG arrangement for rubrene single crystal. (A) Side view, showing sections of the cell, sample, and incident laser beams in laboratory x-z plane. (B) Top view with the sample in laboratory x-y plane. Furthermore, the crystalline a and b axis are shown along with the azimuthal rotation scale in lab coordinates.

SFG spectra were acquired with azimuthal angles from 0° to 360° in 30° steps, with PPP and SSP polarization configurations for each angle. The polarizations indicate the electric field polarization of the SF, visible, and IR beams, respectively. P-polarization electric field vector is in the plane of incidence (i.e., laboratory x-z plane), and S-polarization electric field vector is perpendicular to the plane of incidence. These configurations were selected because of the insufficient SF signal for the surface phenyl groups in all other combinations [47]. The azimuthal angle sequence in the x-y plane was selected randomly as 0°, 30°, 60°, 90°, 150°, 240°, 330°, 120°, 210°, 300°, 180°, 270°, and 360°, to avoid any systematic artifact.

The SFG spectra are shown in Figure 5-7 and Figure 5-8 for PPP and SSP configurations, respectively. Every spectrum in these two sets is an average of five scans. The non-resonant background in PPP spectra is not fixed and displays a broad profile, which changes with sample rotation. While, in SSP spectra, the non-resonant signal is very low. A main resonance peak/dip is observed around  $3058\text{ cm}^{-1}$ , for both PPP and SSP configurations.

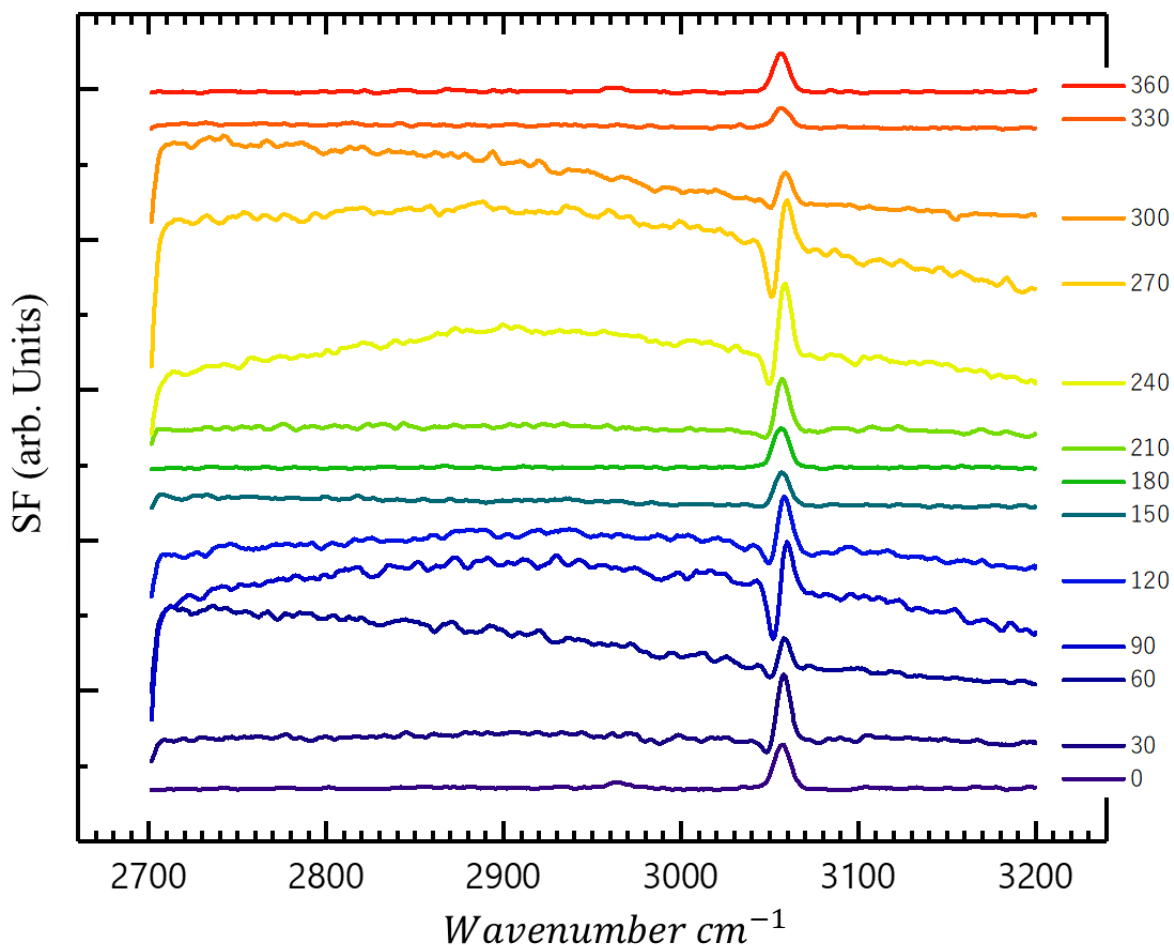


Figure 5-7 Rubrene SFG for PPP polarization combination. Each one of these spectra was collected at different azimuthal angles in the laboratory frame. The corresponding azimuthal angle is given on the right of each spectrum. The sudden fall in the non-resonant SF at the start is due to the cutoff of the signal detector.

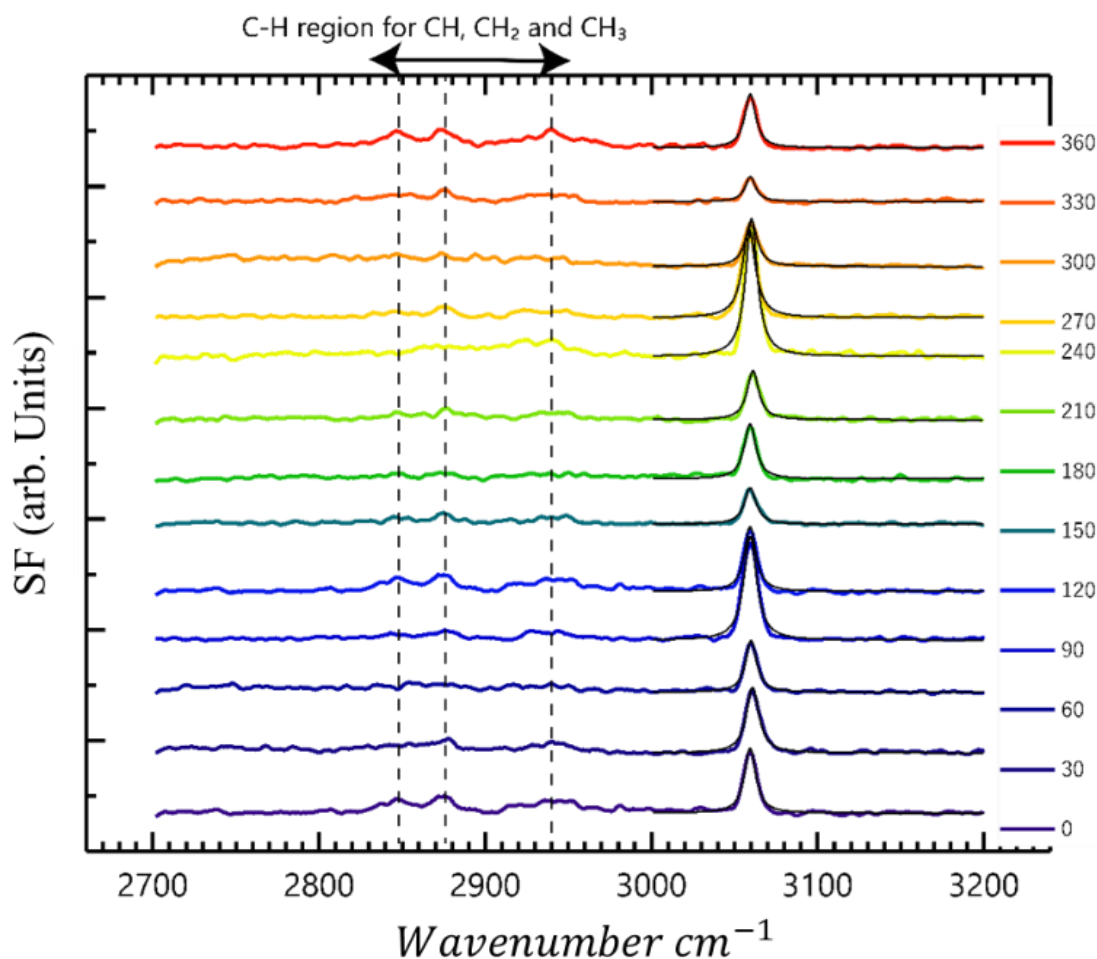


Figure 5-8 Rubrene SFG for SSP polarization combination. Each one of these spectra was collected at different azimuthal angle in the laboratory frame. The corresponding azimuthal angle is given on the right of each spectrum. The dashed lines represent the peaks found in C-H stretch region for CH, CH<sub>2</sub>, and CH<sub>3</sub> groups.

## 5.4 Analysis and Discussion

The SFG analysis section is based on Alamdar Shah Ph.D. thesis to clarify the power of combining the two techniques. More details can be found in his Ph.D. thesis [48].

The herringbone arrangement for the rubrene molecules on the surface is shown in Figure 5-9. The orientation of the phenyl rings on the surface can be obtained from the SFG response since the bulk and the molecular structure of rubrene shows a centrosymmetric system. No SF signal is detected except from the top layer of the phenyl groups [49-51]. Two phenyl groups on one side of the backbone from each rubrene

molecule protrude out from the surface The M axis is perpendicular to the surface plane along the crystalline c axis.

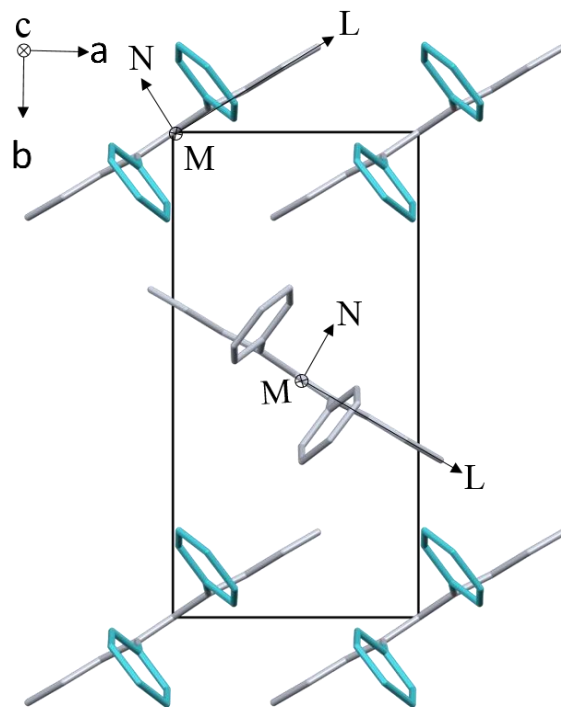


Figure 5-9 The herringbone structure of the rubrene molecules, the unit cell axis (a,b,c), and the molecular axis (L,M,N)

In the absorption spectra,  $a_2$ ,  $a_3$ ,  $b_2$ , and  $b_3$  peaks are due to the molecular transitions with transition dipole predominantly along the molecular L-axis [40]. The refractive indices for the three crystallographic axes are reported as  $n_a \sim 1.7 < n_b \sim 1.9 < n_c \sim 2.0$ . The angle  $\alpha$  between the molecular L-axis and the crystalline a-axis is extracted from the absorption ratio between peaks  $a_2$  and  $b_2$  peaks or  $a_3$  and  $b_3$  by [40]

$$\frac{A_a}{A_b} = \cot^2 \alpha$$

Which results in  $\alpha=38.8^\circ$ , and  $\alpha=38.2^\circ$ , respectively, and an average value of  $38.5^\circ$ , which is close to the literature value ( $37^\circ$ ) [40]. On the other hand, the orientation of the phenyl rings, which project out of the surface, remains unknown, while this orientation can be extracted from SFG spectra.

First, a relation between lab coordinates, crystal axis, molecular coordinates, and the surface phenyl groups are generated, with three angles for the surface phenyl groups. These relations are shown in Figure 5-10 and Figure 5-11. In Figure 5-10, the axis of the phenyl ring plane is presented with respect to the crystal axis. Furthermore, the relation of molecular, crystal, and laboratory axis are illustrated in Figure 5-11. The crystal frame is now related to the laboratory frame through simple azimuthal rotation about laboratory  $z$ - or crystalline  $c$ -axis.

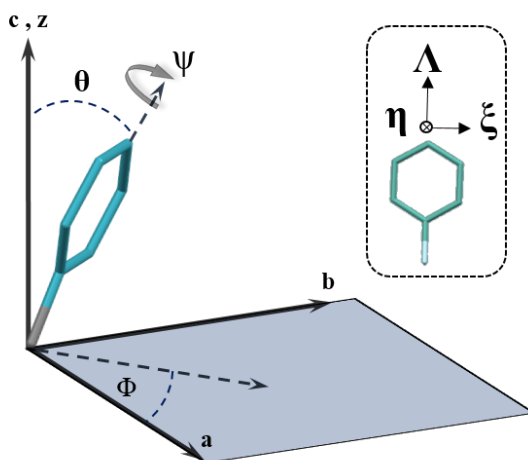


Figure 5-10 The phenyl ring on the surface of the rubrene crystal, the rotation angle, the tilt angle, and azimuthal angle, and their relation to (a,b,c) axis.

The fitted peaks for the PPP and SSP polarizations was compared to the simulated values, to determine the orientation of the phenyl rings ( $\theta$ ,  $\psi$ , and  $\phi$ ). The main step is to define the simulation model. The orientation distributions of  $\theta$ ,  $\psi$ , and  $\phi$  for the surface phenyl rings were modeled by delta functions. Since the two phenyl groups on the surface are the mirror of each other with an equal angle, two angles are defined, one with  $\phi$  clockwise and the other with  $\phi$  anticlockwise from the crystalline  $a$ -axis. In the next step, the azimuthal behaviors of  $\chi_{eff,ppp}^{(2)}$  and  $\chi_{eff,ssp}^{(2)}$  simulations and the experimental results are presented in Figure 5-12. The results are summarized in Table 5-2. The details of the simulation are discussed somewhere else. The best parameters matching the experimental fittings are presented in Table 5-2.

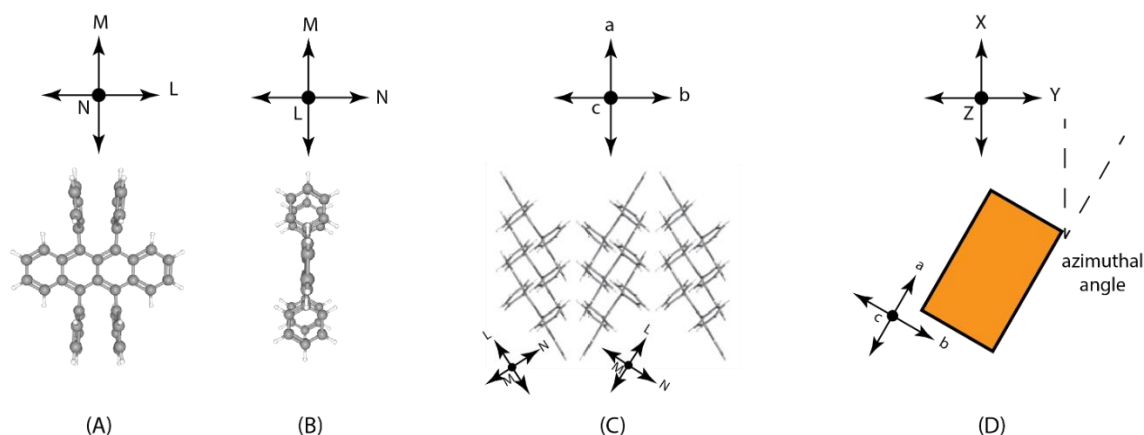


Figure 5-11 Orientational relation between three types of coordinates (crystallographic, molecular, and lab). When the azimuthal angle is zero, the a-axis is aligned with the x-axis in the lab [48].

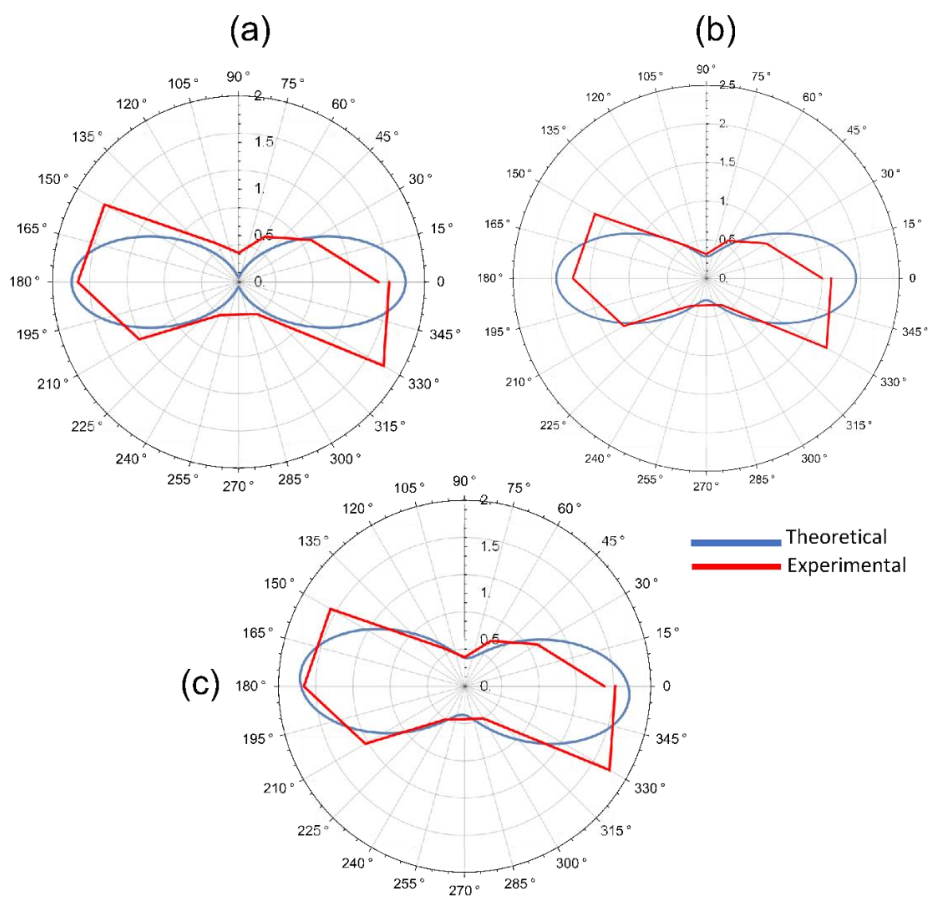


Figure 5-12 Three different angle combinations of the phenyl ring. The results of the azimuthal amplitude ratios from experiments vs. the simulated values. Plots (a), (b), and (c) show the progression of the fitting process with the final fit achieved in the plot (c). In plot (a)  $\theta = 0^\circ$ ,  $\psi = 0^\circ$ , and  $\phi = 32^\circ$ . In plot (b)  $\theta = 45^\circ$ ,  $\psi = 0^\circ$ , and  $\phi = 32^\circ$ . Finally, in the plot (c)  $\theta = 45^\circ$ ,  $\psi = 7^\circ$ , and  $\phi = 32^\circ$ .

Table 5-2 Orientational parameters for the orientational analysis of the phenyl groups of the rubrene on the surface.

Parameter	Value	Standard error $\pm$
$\theta$	29°	10°
$\psi$	8°	8°
$\phi$	35°	3°

In this chapter, multiple techniques were used to characterize the surface of the rubrene single crystal. Using RHEED and the diffraction simulations, the molecular arrangement, crystal structure, and orientation were confirmed. The orientational information of the phenyl group on the surface of the molecule was determined by linking three different coordinates, namely crystallographic, molecular, and lab coordinates. A 27-degree tilt angle was extracted from the resonant SFG peak for the C-H symmetric stretch of the phenyl rings. Even though the combination of the SFG and RHEED techniques in this experiment is not unique, and other methods could be capable of the same output, it is still a clear example of the power of this combination for future research directions.

## 5.5 Bibliography

- [1] Y. Kijima, N. Asai, and S.-i. Tamura, "A blue organic light-emitting diode," *Japanese Journal of Applied Physics*, vol. 38, no. 9R, p. 5274, 1999.
- [2] B. Geffroy, P. Le Roy, and C. Prat, "Organic light-emitting diode (OLED) technology: materials, devices and display technologies," *Polymer International*, vol. 55, no. 6, pp. 572-582, 2006.
- [3] B. C. Krummamera, V.-E. Choong, M. K. Mathai, S. A. Choulis, and F. So, "Highly efficient white organic light-emitting diode," *Applied Physics Letters*, vol. 88, no. 11, p. 113506, 2006.
- [4] T. Sekitani, H. Nakajima, H. Maeda, T. Fukushima, T. Aida, K. Hata, and T. Someya, "Stretchable active-matrix organic light-emitting diode display using printable elastic conductors," *Nature Materials*, vol. 8, no. 6, pp. 494-499, 2009.
- [5] H.-W. Chen, J.-H. Lee, B.-Y. Lin, S. Chen, and S.-T. Wu, "Liquid crystal display and organic light-emitting diode display: present status and future perspectives," *Light Science Applications*, vol. 7, no. 3, pp. 17168-17168, 2018.
- [6] D. Wöhrle and D. Meissner, "Organic solar cells," *Advanced Materials*, vol. 3, no. 3, pp. 129-138, 1991.
- [7] H. Hoppe and N. S. Sariciftci, "Organic solar cells: An overview," *Journal of Materials Research*, vol. 19, no. 7, pp. 1924-1945, 2004.
- [8] J. Wu, H. A. Becerril, Z. Bao, Z. Liu, Y. Chen, and P. Peumans, "Organic solar cells with solution-processed graphene transparent electrodes," *Applied Physics Letters*, vol. 92, no. 26, p. 237, 2008.
- [9] M. Kaltenbrunner *et al.*, "Ultrathin and lightweight organic solar cells with high flexibility," *Nature Communications*, vol. 3, no. 1, pp. 1-7, 2012.
- [10] P. Cheng and X. Zhan, "Stability of organic solar cells: challenges and strategies," *Chemical Society Reviews*, vol. 45, no. 9, pp. 2544-2582, 2016.
- [11] H. Murata, C. D. Merritt, and Z. H. Kafafi, "Emission mechanism in rubrene-doped molecular organic light-emitting diodes: direct carrier recombination at luminescent centers," *IEEE Journal of Selected Topics in Quantum Electronics*, vol. 4, no. 1, pp. 119-124, 1998.
- [12] H. Aziz and Z. D. Popovic, "Study of organic light-emitting devices with a 5, 6, 11, 12-tetraphenylnaphthacene (rubrene)-doped hole transport layer," *Applied Physics Letters*, vol. 80, no. 12, pp. 2180-2182, 2002.
- [13] V. Podzorov, V. Pudalov, and M. Gershenson, "Field-effect transistors on rubrene single crystals with parylene gate insulator," *Applied Physics Letters*, vol. 82, no. 11, pp. 1739-1741, 2003.

- [14] W. Xie, M. Meng, C. Li, Y. Zhao, and S. Liu, "High-efficiency simple structure white organic light-emitting devices based on rubrene ultrathin layer," *Optical and Quantum Electronics*, vol. 37, no. 10, pp. 943-948, 2005/08/01 2005.
- [15] A. K. Pandey and J.-M. Nunzi, "Rubrene/Fullerene heterostructures with a half-gap electroluminescence threshold and large photovoltage," *Advanced Materials*, vol. 19, no. 21, pp. 3613-3617, 2007.
- [16] A. K. Pandey and J.-M. Nunzi, "Upconversion injection in rubrene/perylene-diimide-heterostructure electroluminescent diodes," *Applied Physics Letters*, vol. 90, no. 26, p. 263508, 2007.
- [17] R. W. I. de Boer, M. Gershenson, A. Morpurgo, and V. Podzorov, "Organic single-crystal field-effect transistors," *Physica Status Solidi (a)*, vol. 201, no. 6, pp. 1302-1331, 2004.
- [18] J. Takeya *et al.*, "Very high-mobility organic single-crystal transistors with in-crystal conduction channels," *Applied Physics Letters*, vol. 90, no. 10, p. 102120, 2007.
- [19] W. Xie, K. A. McGarry, F. Liu, Y. Wu, P. P. Ruden, C. J. Douglas, and C. D. Frisbie, "High-mobility transistors based on single crystals of isotopically substituted rubrene-d 28," *The Journal of Physical Chemistry C*, vol. 117, no. 22, pp. 11522-11529, 2013.
- [20] J. Nitta, K. Miwa, N. Komiyama, E. Annese, J. Fujii, S. Ono, and K. Sakamoto, "The actual electronic band structure of a rubrene single crystal," *Scientific Reports*, vol. 9, no. 1, p. 9645, Jul 4, 2019.
- [21] T. Iimori, R. Ito, and N. Ohta, "Stark spectroscopy of rubrene. II. Stark fluorescence spectroscopy and fluorescence quenching induced by an external electric field," *Journal of Physical Chemistry A*, vol. 120, no. 28, pp. 5497-503, Jul 21, 2016.
- [22] J. J. Kim *et al.*, "Correlating crystal thickness, surface morphology, and charge transport in pristine and doped rubrene single crystals," *ACS Applied Materials & Interfaces*, vol. 10, no. 31, pp. 26745-26751, Aug 8, 2018.
- [23] W. Li, M. Fronk, H. Kupfer, S. Schulze, M. Hietschold, D. R. T. Zahn, and G. Salvan, "Aging of rubrene layers in Ni/rubrene heterostructures studied by magneto-optical Kerr effect spectroscopy," *Journal of the American Chemical Society*, vol. 132, no. 16, pp. 5687-92, Apr 28, 2010.
- [24] S. W. Park, J. M. Choi, K. H. Lee, H. W. Yeom, S. Im, and Y. K. Lee, "Amorphous-to-crystalline phase transformation of thin-film rubrene," *Journal of Physical Chemistry B*, vol. 114, no. 17, pp. 5661-5, May 6, 2010.
- [25] X. Ren, C. D. Frisbie, and C. Leighton, "Anomalous cooling-rate-dependent charge transport in electrolyte-gated rubrene crystals," *Journal of Physical Chemistry Letters*, vol. 9, no. 17, pp. 4828-4833, Sep 6, 2018.
- [26] K. Sun, M. Lan, and J. Z. Wang, "Absolute configuration and chiral self-assembly of rubrene on Bi (111)," *Phys Chem Chem Phys*, vol. 17, no. 39, pp. 26220-4, Oct 21, 2015.

- [27] S. Tao, N. Ohtani, R. Uchida, T. Miyamoto, Y. Matsui, H. Yada, H. Uemura, H. Matsuzaki, T. Uemura, J. Takeya, and H. Okamoto, "Relaxation dynamics of photoexcited excitons in rubrene single crystals using femtosecond absorption spectroscopy," *Physical Review Letters*, vol. 109, no. 9, p. 097403, Aug 31, 2012.
- [28] T. Ueba, T. Yamada, and T. Munakata, "Electronic excitation and relaxation dynamics of the LUMO-derived level in rubrene thin films on graphite," *Journal of Chemical Physics*, vol. 145, no. 21, p. 214703, Dec 7, 2016.
- [29] D. Okaue, I. Tanabe, S. Ono, K. Sakamoto, T. Sato, A. Imanishi, Y. Morikawa, J. Takeya, and K.-i. Fukui, "Ionic-liquid-originated carrier trapping dynamics at the interface in electric double layer organic FET revealed by operando interfacial analyses," *The Journal of Physical Chemistry C*, vol. 124, no. 4, pp. 2543-2552, 2020.
- [30] J.-Z. Wang, M. Lan, T.-N. Shao, G.-Q. Li, Y. Zhang, C.-Z. Huang, Z.-H. Xiong, X.-C. Ma, J.-F. Jia, and Q.-K. Xue, "STM study of a rubrene monolayer on Bi (001): Structural modulations," *Physical Review B*, vol. 83, no. 23, p. 235433, 2011.
- [31] M.-C. BLÜM, "Supramolecular assembly, chirality, and electronic properties of rubrene studied by STM and STS," *Swiss Federal Institute of Technology Lausanne*, 2006.
- [32] J. Miwa, F. Cicoira, J. Lipton-Duffin, D. Perepichka, C. Santato, and F. Rosei, "Self-assembly of rubrene on Cu (111)," *Nanotechnology*, vol. 19, no. 42, p. 424021, 2008.
- [33] T. Minato, H. Aoki, H. Fukidome, T. Wagner, and K. Itaya, "High-resolution molecular images of rubrene single crystals obtained by frequency modulation atomic force microscopy," *Applied Physics Letters*, vol. 95, no. 9, p. 221, 2009.
- [34] Y. Yokota, Hisaya Hara, T. Harada, A. Imanishi, T. Uemura, J. Takeya, and K.-i. Fukui, "Structural investigation of ionic liquid/rubrene single-crystal interfaces by using frequency-modulation atomic force microscopy," *Chemical Communications*, vol. 49, no. 90, pp. 10596-10598, 2013.
- [35] S. Sinha, C.-H. Wang, M. Mukherjee, T. Mukherjee, and Y.-W. Yang, "Oxidation of rubrene thin films: an electronic structure study," *Langmuir*, vol. 30, no. 51, pp. 15433-15441, 2014.
- [36] C.-Q. LENG, H.-R. LI, Y. LI, and P.-J. GAO, "Surface and interface analysis of Rubrene/TPD using AFM and XPS," *Journal of Functional Materials*, p. S2, 2010.
- [37] G. Ji, G. Zheng, B. Zhao, F. Song, X. Zhang, K. Shen, Y. Yang, Y. Xiong, X. Gao, L. Cao, and D.-C. Qi, "Interfacial electronic structures revealed at the rubrene/CH<sub>3</sub>NH<sub>3</sub>PbI<sub>3</sub> interface," *Physical Chemistry Chemical Physics*, vol. 19, no. 9, pp. 6546-6553, Mar 1, 2017.
- [38] H. H. Choi, H. T. Yi, J. Tsurumi, J. J. Kim, A. L. Briseno, S. Watanabe, J. Takeya, K. Cho, V. Podzorov, "A large anisotropic enhancement of the charge carrier mobility of flexible organic transistors with strain: a hall effect and Raman study.," *Advanced Science*, vol. 7, no. 1, p. 1901824, Jan 2020.

- [39] K. Bera, C. J. Douglas, and R. R. Frontiera, "Femtosecond Raman microscopy reveals structural dynamics leading to triplet separation in rubrene singlet fission," *Journal of Physical Chemistry Letters*, vol. 8, no. 23, pp. 5929-5934, Dec 7, 2017.
- [40] S. Tavazzi, A. Borghesi, A. Papagni, P. Spearman, L. Silvestri, A. Yassar, A. Camposeo, M. Polo, and D. Pisignano, "Optical response and emission waveguiding in rubrene crystals," *Physical Review B*, vol. 75, no. 24, p. 245416, 2007.
- [41] H. Jiang and C. Kloc, "Single-crystal growth of organic semiconductors," *MRS Bulletin*, vol. 38, no. 1, pp. 28-33, 2013.
- [42] O. D. Jurchescu, A. Meetsma, and T. T. Palstra, "Low-temperature structure of rubrene single crystals grown by vapor transport," *Acta Crystallographica Section B: Structural Science*, vol. 62, no. 2, pp. 330-334, 2006.
- [43] D. Käfer, L. Ruppel, G. Witte, and C. Wöll, "Role of molecular conformations in rubrene thin film growth," *Physical Review Letters*, vol. 95, no. 16, p. 166602, 2005.
- [44] P. Irkhin and I. Biaggio, "Two-photon absorption spectroscopy of rubrene single crystals," *Physical Review B*, vol. 89, no. 20, p. 201202, 2014.
- [45] L. Raimondo, S. Trabattoni, M. Moret, N. Masciocchi, M. Masino, and A. Sassella, "Oxidation of crystalline rubrene films: evidence of an epitaxial native oxide layer," *Advanced Materials Interfaces*, vol. 4, no. 23, p. 1700670, 2017.
- [46] J. T. Ly *et al.*, "Oxidation of rubrene, and implications for device stability," *Journal of Materials Chemistry C*, vol. 6, no. 14, pp. 3757-3761, 2018.
- [47] M. Oh-e, S.-C. Hong, and Y. R. Shen, "Orientations of phenyl side groups and liquid crystal molecules on a rubbed polystyrene surface," *Applied Physics Letters*, vol. 80, no. 5, pp. 784-786, 2002.
- [48] S. A. H. Shah, "Super-resolution imaging, orientation analysis, and image processing with machine learning in sum frequency generation spectroscopy" *Doctor of Philosophy Chemistry*, University of Houston, Department of Chemistry, College of Natural Sciences and Mathematics, 2020.
- [49] H.-F. Wang, L. Velarde, W. Gan, and L. Fu, "Quantitative sum-frequency generation vibrational spectroscopy of molecular surfaces and interfaces: line-shape, polarization, and orientation," *Annual Review of Physical Chemistry*, vol. 66, no. 1, pp. 189-216, 2015/04/01 2015.
- [50] G. R. Bell, "Orientation of benzoate ions bound to a monolayer of a cationic surfactant at the surface of water," *Molecular Physics*, vol. 88, no. 1, pp. 269-280, 1996.
- [51] D. C. Duffy, P. B. Davies, and C. D. Bain, "Surface vibrational spectroscopy of organic counterions bound to a surfactant monolayer," *The Journal of Physical Chemistry*, vol. 99, no. 41, pp. 15241-15246, 1995.

# Chapter 6

Low-Temperature Study of Self-Assemble Monolayers on Gold

# Chapter 6: Low-Temperature Study of Self-Assemble Monolayers on Gold

In this chapter, the behavior of the three different alkanethiols (R-SH) of different chain lengths deposited on gold thin films is studied at temperatures from 300 K down to 85 K, using sum-frequency generation (SFG), under high vacuum conditions. A high-vacuum chamber is designed and made in the lab to open the possibility of high-vacuum studies for SFG spectroscopy and imaging. The high vacuum (HV) chamber details are elaborated, and the results are discussed at the end.

## 6.1 Introduction

One of the powerful methods of preparing thin films with molecular orientation is the self-assembled monolayer (SAM). The SAMs can be prepared either by immersing the substrate in a solution containing the active surfactant or deposition in a vacuum. Several types of SAMs have been studied in detail, including organosilicon on oxidized substrate, dialkyl sulfides and dialkyl disulfide on Au, and alkanethiols on Au [1]. Thiol SAMs on a gold substrate have been studied extensively since 1983, after their discovery by Nuzzo and Allara [2], for phenomena such as bonding, friction, lubrication, interfacial electron transfer, and catalysis [3-9].

Self-assembled monolayers are organic molecules chemisorbed on a surface, held together by non-covalent bonds, such as van der Waals interaction, the  $\pi$ - $\pi$  interaction, and hydrogen bonds [10]. They are composed of three main parts, as is shown in Figure 6-1. The part in contact with the substrate is called the molecule "headgroup," with a strong chemical affinity to the surface. The "tail group" is the part on the other end of the molecule oriented away from the surface. Finally, the part connecting them is called the "spacers," which are mainly alkyl chains. By varying each of these three sections of the molecule, it is possible to control the properties of the molecule for different applications [11-18].

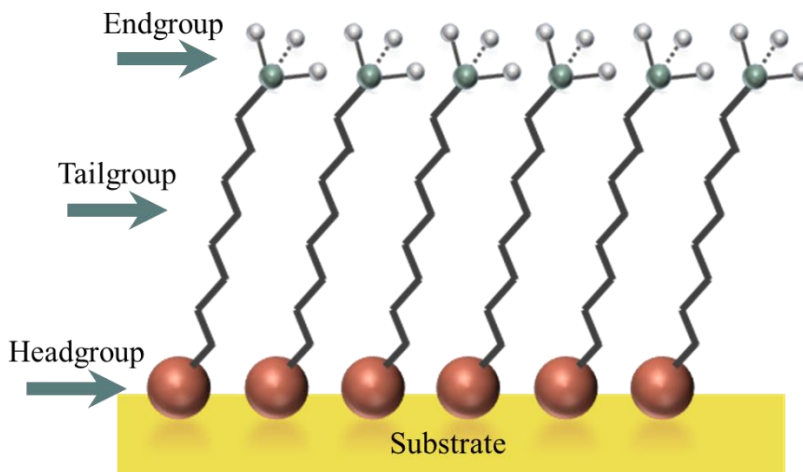


Figure 6-1 Schematic of an n-Alkanethiol SAM on a gold substrate and the three main parts of the molecule.

## 6.2 Gold Substrate and SAM Sample Preparation

Gold surface is the most common substrate for thiol SAMs deposition. Gold surfaces can be prepared usually by physical vapor deposition under a high vacuum, growing on a silicon wafer, and chromium layer for enhanced adhesion. The as-deposited gold usually has small grains of 40 – 60 nm, which can be enhanced by flame annealing.

SAMs can be prepared by directly dipping the gold substrate in a solution of thiols with an organic solvent for 12 – 48 h. In this experiment, 1 – 2 mM thiol solutions in ethanol solvent were used to deposit the thiols on gold substrate [19].

The thiol SAMs have been extensively studied in different experimental conditions by varying parameters such as dipping time, concentration, and temperature effect at high temperatures. [20-23]. However, there is not too much study for the effect of temperature on the orientation of the SAMs at low temperatures, especially no vibrational spectroscopy studies under UHV conditions. For example, annealing SAMs in solution for a short time, less than 1 h, is reported to increase the domain size of the assembled monolayer from a few nm at room temperature to 100 nm or higher at temperatures of about 100 °C [24]. Annealing at higher temperatures could negatively affect the film quality [25, 26].

In this experiment, the effect of cooling on SAMs has been studied by sum-frequency generation (SFG) spectroscopy for thiols with different chain lengths under high-vacuum conditions. The experiment results show an unreported situation at low temperatures; however, it requires a systematic study to investigate further the phenomena resulting from such observations in the SFG experiment. The rest of this chapter discusses the development of the high-vacuum setup, the initial results, and future directions.

### 6.3 High-Vacuum Setup

The design of the high-vacuum cell is based on the SFG imaging setup to minimize the traveling path of the laser beams inside the vacuum before hitting the sample. As a result, the cell is designed like a birdhouse for an optimized total length (Figure 6-2).

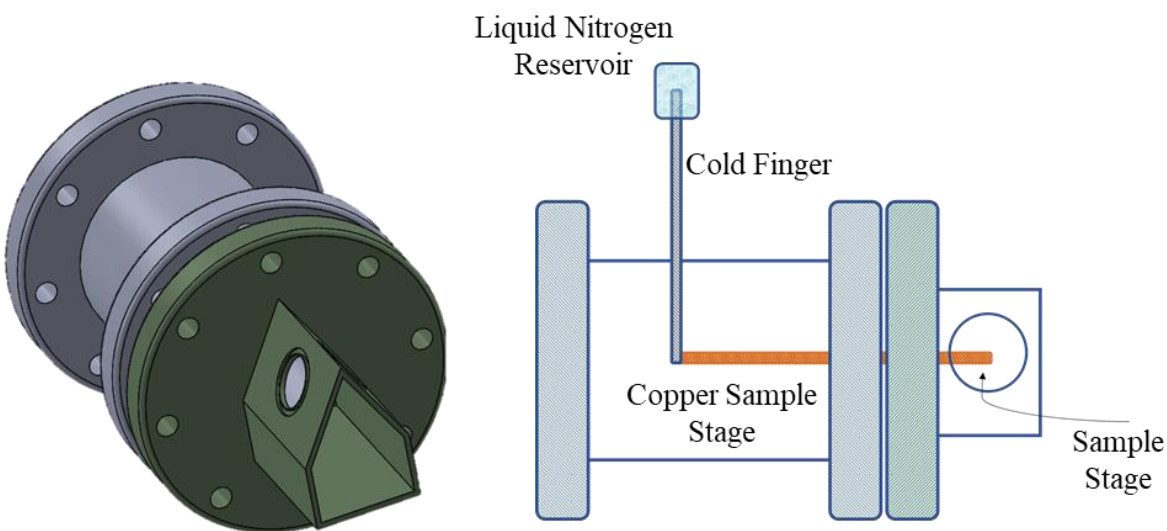


Figure 6-2 The birdhouse shape cell (Green part) with two optical windows as input and output of the laser beam.

The chamber is composed of a cold finger, which transfers the liquid nitrogen to the copper sample holder, a sample holder in contact with the cold finger with a tight physical contact, and two optical windows for input and output beams. The glasses are  $\text{CaF}_2$  and quartz, respectively.

The sample is cooled down to 85 K using liquid nitrogen. Then, the cold finger transfers the liquid nitrogen directly to the copper sample stage, which as a result, the sample stage cools down to 88 K in less than 30 min (As shown in Figure 6-3).

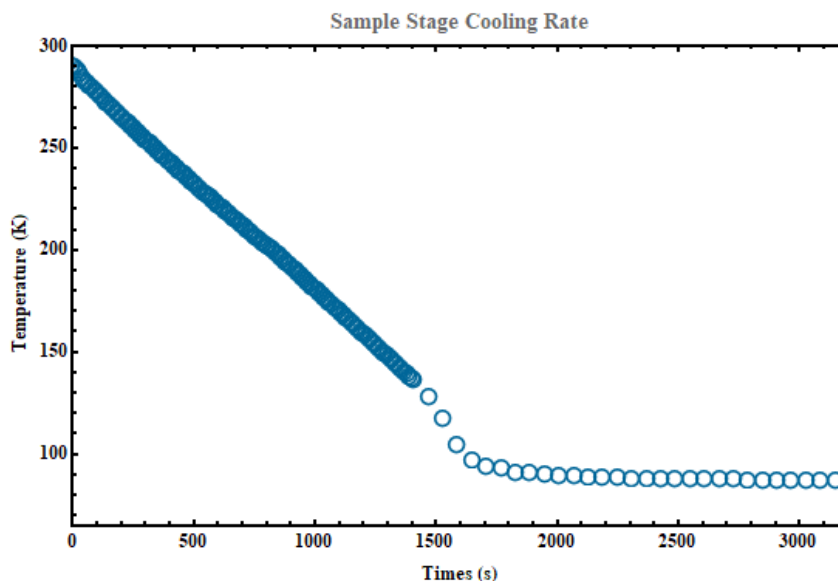


Figure 6-3 The cooling rate of the sample stage with liquid nitrogen

In addition to sample cooling, it is possible to heat the sample with either resistive heating or electron bombardment heating, using a home-built heating stage for each type. The resistive heater controls temperatures from 500 K to 88 K. In case of the requirements for high temperature, the electron bombardment must be used to reach temperatures of 1000 K or higher.

The fully assembled chamber is shown in Figure 6-4 on the SFG optical table. The image on the left shows the main components of the system outside the high-vacuum environment, including an LN<sub>2</sub> reservoir to keep liquid nitrogen during the experiment, which is made in the lab using Styrofoam and shaped into a cylinder. Other components are thermocouple feedthrough, electrical feedthrough, and pumping tube connection to the turbopump. The chamber is assembled on a manipulator, made in the lab to adjust the sample for the SFG spectroscopy experiment. On the right side, the top view of the chamber is shown, with the two input laser beams and the SFG output beam from the two optical windows.

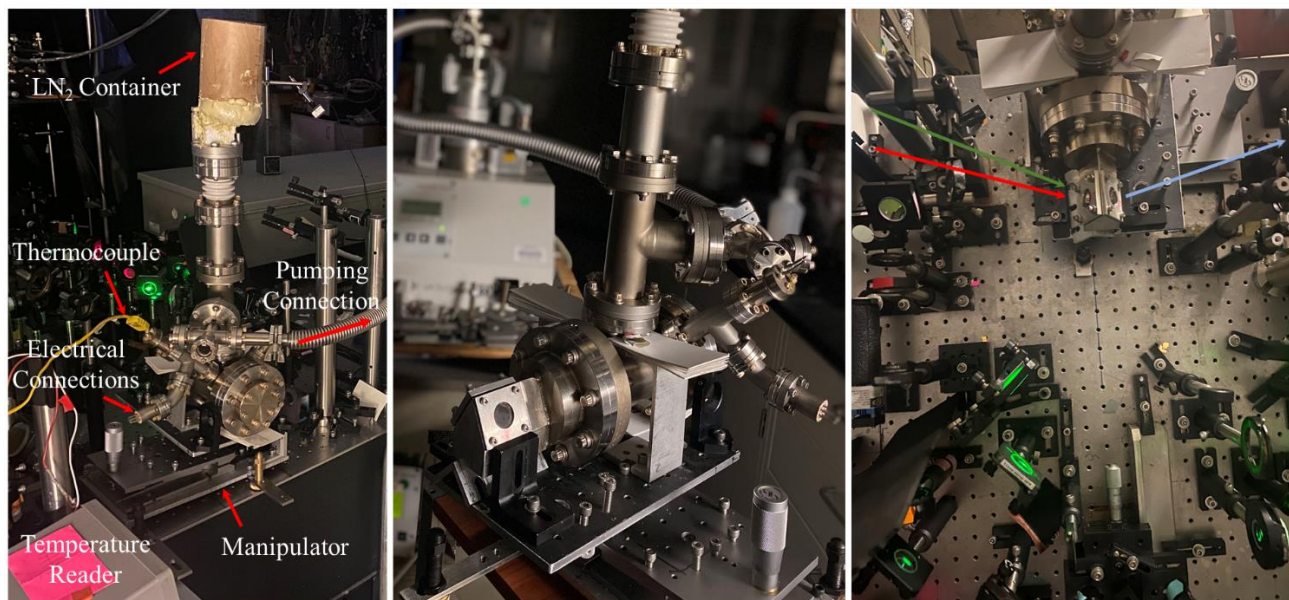


Figure 6-4 The bird cell on the SFG optical table, with all connections, including pumping, electrical, and thermocouple connections.

The  $\text{LN}_2$  reservoir is the container to transfer the nitrogen to the cold finger, which is in contact with a copper part, which acts as the sample holder. The actual part is shown in Figure 6-5, and the schematic diagram is shown in Figure 6-6 for better visualization.

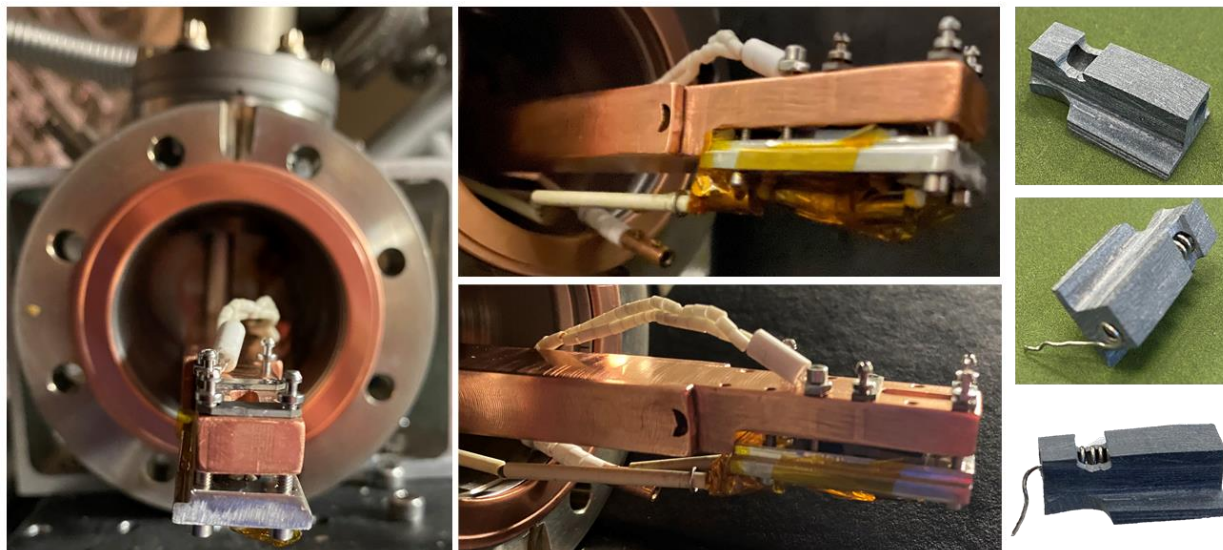


Figure 6-5 Inside the bird cell, with a resistive heater, thermocouple connection, and the custom-made resistive heater consists of a nichrome wire embedded inside an alumina ceramic.

The sample stage is shown in detail in Figure 6-6, which shows (a) the heating element for either resistive heating or electron bombardment, (b) the heating assembly with the bottom part of the heating assembly made from stainless steel, (c) the whole copper block with the cold finger, the sample, and the hole for electron beam heating from the back of the sample.

For the case of resistive heating, the heating element is embedded inside an alumina ceramic to insulate the heater electrically from the copper part. The heating element for the resistive heating is shown in Figure 6-5, on the right side, with the ceramic part on the top-right of the image, and the imbedded resistive heater on the bottom.

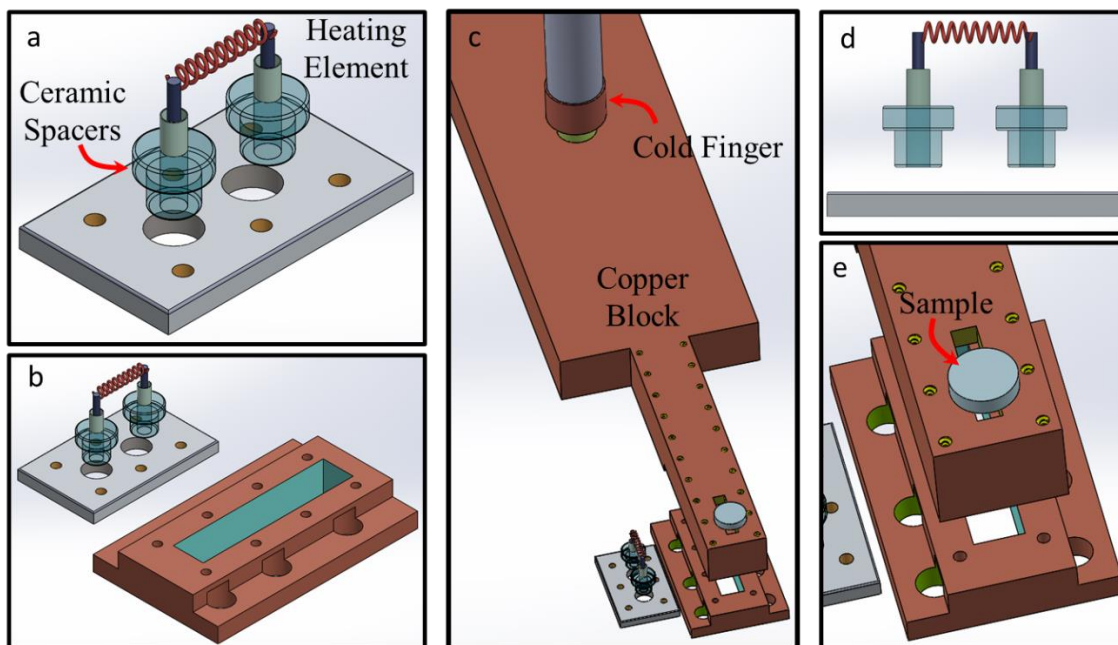


Figure 6-6 The schematic outline of the assembly of the heating and cooling parts of the sample stage.

To use the e-beam heating, the sample must be electrically grounded and thermally in contact with the copper, which in this case, sapphire sheets with the size of 5 mm by 5 mm are placed between the sample and the copper block. Due to the temperature-dependent properties of the sapphire, at high temperatures, the heat mainly stays inside the sample since sapphire is not good conductive material. In contrast, the heat can be transferred from the copper block to the sample with a reasonable heat transfer at low temperatures. As a

result, sapphire creates the possibility of improving heat transfer at low temperatures and decreasing heat transfer at high temperatures. The two types of heating setups are shown in Figure 6-7. As a result, the e-beam heating can heat the sample locally to 800 °C in a couple of seconds. On the other hand, resistive heating can heat the sample to 400 °C, with much lower rates (1 – 10 °C/min), which is a better option to control the temperature of the sample at temperatures lower than room temperature.

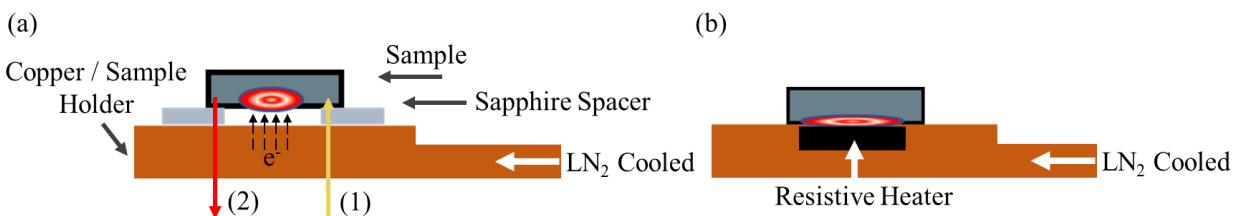


Figure 6-7 Two types of possible heating for the bird cell heater (a) Heating the sample with electron bombardment, with sapphire spacers for controlled heating and cooling. (b) The resistive heater is in direct contact with the sample.

The vacuum chamber operates at  $10^{-6}$  torr, can heat, and cool the sample, and purge different types of gases, to study phenomena like corrosion, or gas adsorption. The main advantage is the vast new possibilities that come true by studying those phenomena in a more localized area on the sample using SFG imaging, which is the primary goal of designing this cell.

## 6.4 Low-Temperature SFG of n-Alkanethiol Monolayers on Gold

In this experiment, temperature-dependent SFG studies on three thiols deposited on a gold substrate in solution have been conducted and repeated three times for each molecule, starting with a new freshly deposited sample and an additional test with a different concentration (2 mM or 4 mM). The results of all concentrations were the same.

The variable in the thiols studied in this experiment is their chain length. However, the observed results have never been reported to the best of our knowledge. As a result, many systematic experiments can be designed to elucidate the mechanism or mechanisms involved in this experiment.

1 mM and 2 mM solutions of 1-octadecanethiol ( $\text{CH}_3(\text{CH}_2)_{17}\text{SH}$ ), 1-decanethiol ( $\text{CH}_3(\text{CH}_2)_9\text{SH}$ ), and 1-octanethiol ( $\text{CH}_3(\text{CH}_2)_7\text{SH}$ ), called  $\text{C}_{18}$  or ODT,  $\text{C}_{10}$  or DT, and  $\text{C}_8$  or OT hereafter, has been prepared in ethanol solvent at room temperature and was deposited on gold wafers by simply immersing the gold substrate in each solution for 48 h. Each freshly deposited sample was transferred into the high-vacuum (HV) cell immediately after the sample was dried by nitrogen gas and pumped down to  $10^{-6}$  torr in less than 20 min. The first stage of pumping takes about 10 min to reach  $10^{-5}$  torr. In this stage, each sample was kept under vacuum for 24 h to reach the base pressure of the cell, which is almost  $7 \times 10^{-7}$  torr, before starting the temperature. Finally, each sample was cut in half to perform the SFG experiment outside the HV cell for reference and inside the HV cell for temperature-dependent studies.

Sample temperatures were controlled with 0.5 K accuracy for each temperature using a combination of  $\text{LN}_2$  cooling and resistive heating. The cooling rate of the cell is almost linear, as is shown in Figure 6-3, which is about 7 K/min. By controlling the applied voltage on the resistive heater, the temperature can be kept stable when the heating and cooling rate are the same. In addition, for each data set, the SFG signal of a clean and fresh gold substrate is recorded for additional reference of any signal drop due to the window thickness or other cell-induced changes. Next, two additional steps were performed to ensure there was no artificial effect induced by the cell. (1) a gold substrate was recorded outside and inside the cell and compared. (2) an ODT on gold was recorded outside and inside the cell and compared, which shows no changes in peak shapes and positions, even though the total signal level drops. Since the relative intensities are the main parameters for further investigations, the signal level drop is not affecting the analysis, even though multiple references have been considered to normalize the data sets for more quantitative analysis if required.

Two polarization configurations (SSP and PPP) are recorded for each sample, which shows the polarization of the SFG, green, and IR beams, respectively. As an example, SSP polarization means S-polarized SFG, S-polarized green, and P-polarized IR beam.

## 6.5 SFG Experimental Data and Discussion

Figure 6-8 shows the SFG data, with PPP polarization configuration, for three thiols monolayers on gold substrates with different chain length at room temperature (RT), lowest reachable temperature (88 K), and one temperature in the middle, with an offset for each spectrum to visually separate them.

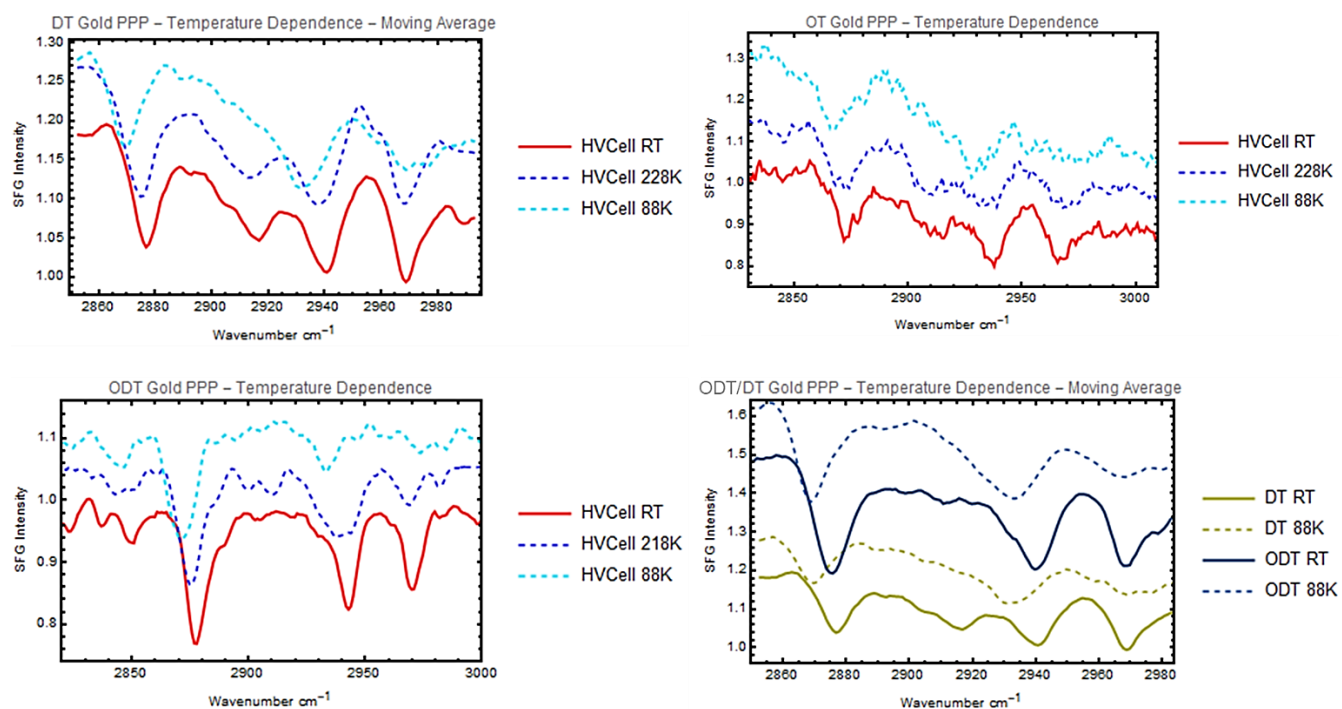


Figure 6-8 The PPP polarization configuration for three samples with different chain lengths and three temperatures. (top-left) C<sub>10</sub> sample (top-right) C<sub>8</sub> sample (bottom-left) C<sub>18</sub> sample (bottom-right) Comparison of C<sub>10</sub> and C<sub>18</sub>

Also, the SSP polarization configuration data is shown in Figure 6-9. First, the labeling logic is discussed, and the data is later explained. Each plot shows the SF intensity vs. the IR wavenumber, which was scanned for each data set. The PPP polarization data set is averaged over three scans. The SSP data set is averaged over six scans since the SSP signal is weaker than the PPP configuration data.

In addition, each plot is labeled with a couple of abbreviated names, which are explained in Table 6-1. Generally, the labels show whether the data is for the high vacuum cell (HV) or in an ambient environment. It also shows the polarization configuration and the molecule under study.

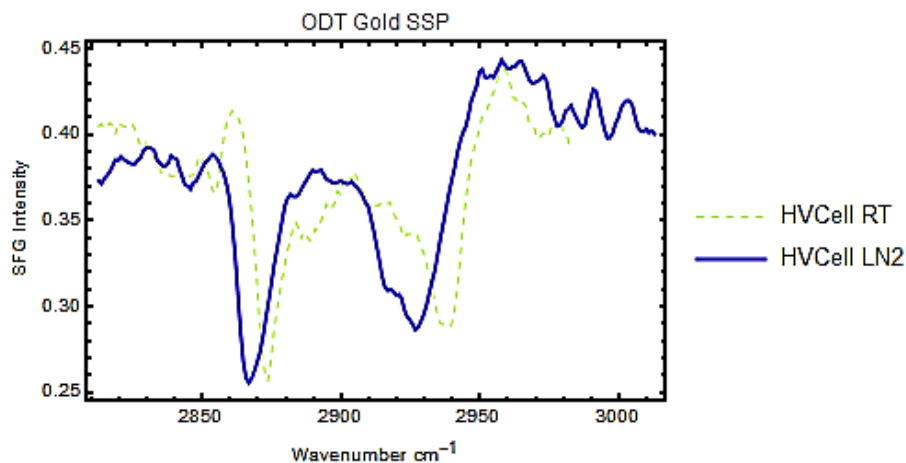


Figure 6-9 The SSP configuration data for C<sub>18</sub> sample at room temperature and lowest possible temperature (85 K)

Table 6-1 Abbreviations for labeling the plots and their definition

Abbreviation	Definition	Abbreviation	Definition
PPP	(SFG)(Green)(IR) polarizations	RT	Room Temperature
SSP	(SFG)(Green)(IR) polarizations	LN <sub>2</sub>	Lowest possible Temperature (85 K)
HVCeIl	Data is recorded inside the cell	NoCell	Data is recorded outside the cell

A couple of changes are noticeable in all data sets, which has never been reported previously for the SAM samples, even though the thiols SAMs have been studied extensively. First, both PPP and SSP spectra are red-shifted by decreasing the temperature from room temperature to 85 K for almost eight wavenumbers for both. On the other hand, while the SSP only shows the change in peak positions, the PPP spectrum shows a gradual peak disappearance, around 2970 cm<sup>-1</sup>, observed for all three chain lengths.

To confirm that the observed phenomenon is real, the experiment was repeated more than three times, and each time a fresh sample was used. In addition, to ensure the peak disappearance is not a laser-induced effect, the sample was scanned at one single point 25 times, and the first, 10<sup>th</sup>, and 25<sup>th</sup> scans were compared, as shown in Figure 6-10. There is no peak shape change, while there is a minimal intensity change. Since the

actual data set is only from three scans, the total time the sample is exposed to the laser is short, and the intensity change is not considered in this experiment.

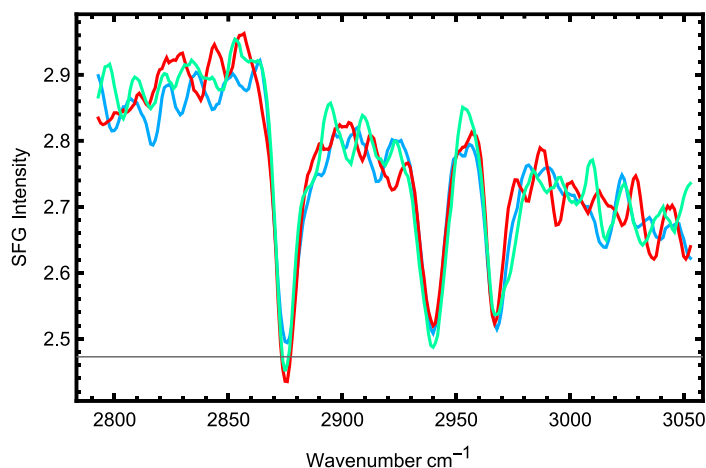


Figure 6-10 PPP data for C<sub>18</sub> sample for three selected scans for a 25 scans experiment.

In addition, the effect of the high vacuum cell itself was checked by recording the data of the same sample cut in half from the same batch, inside the high vacuum cell and outside the cell, exposed to air, as is shown in Figure 6-11. The data were recorded for three different samples, and three random points on the sample for each sample. It is obvious from these data sets that the observed phenomena is not an artifact, and is confirmed to be a real phenomenon for the SAM samples on gold.

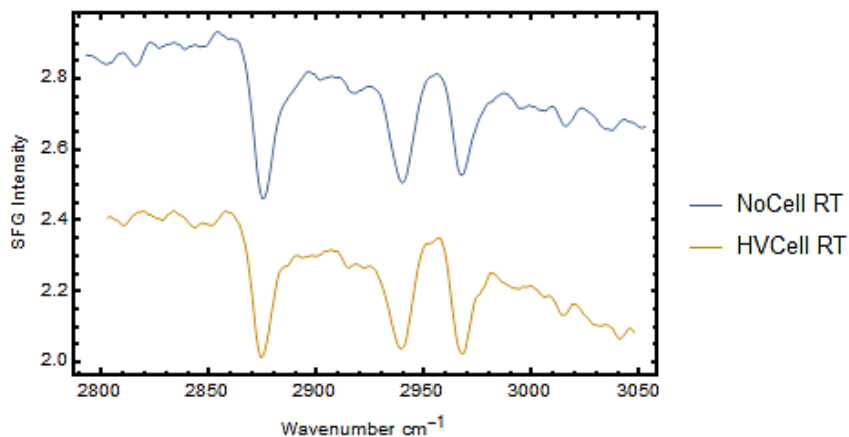


Figure 6-11 The PPP configuration data of the same sample, outside and inside the high vacuum cell, to compare the effect of the cell on the spectrum.

In addition, the samples were checked after they naturally went back to room temperature, which are shown in Figure 6-12 and Figure 6-13. Here, the peak's positions return to the room temperature case for both PPP and SSP data sets in all samples. Interestingly, the disappeared peak around 2970  $\text{cm}^{-1}$  also appears again at room temperature, which means the observed phenomena are naturally reversible.

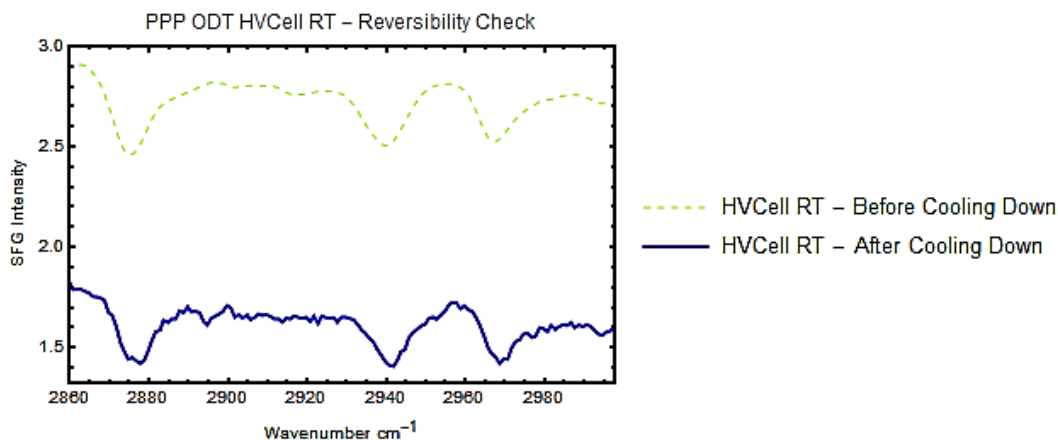


Figure 6-12 Reversibility check of the PPP peaks before and after cooling. Both spectra are at room temperature, with one of them before cooling the sample and the other one after cooling, naturally going back to room temperature.

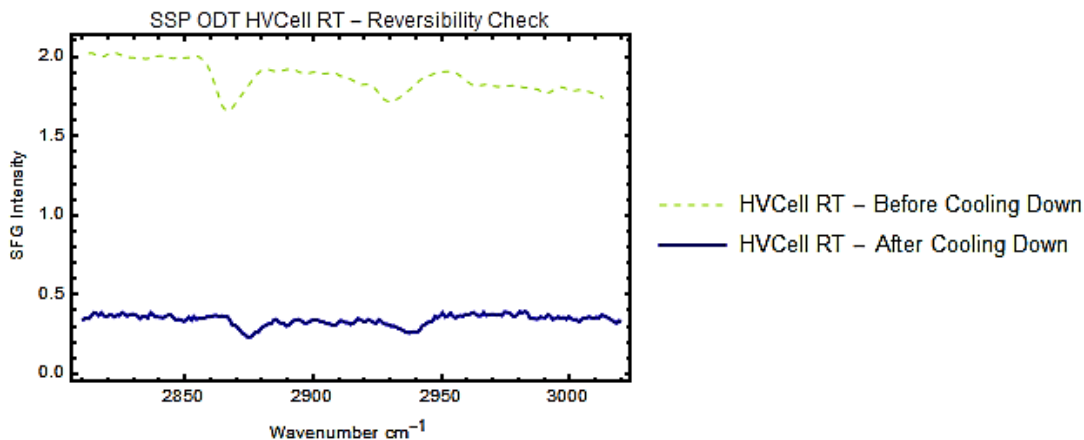


Figure 6-13 Reversibility check of the SSP peaks before and after cooling. Both spectra are at room temperature, with one of them before cooling the sample and the other one after cooling, naturally going back to room temperature.

## 6.6 Future Work

The analysis of these data sets requires additional information and a hypothesis to explain these observations. In addition, the same set of experiments on different substrates, including the single-crystalline gold, and comparing the observations are required for a clear understanding of these phenomena. In this section, one possible reason for this observation is briefly discussed. However, more analysis is required to validate this hypothesis.

Before discussing the temperature-dependent behavior of the thiol films in Figure 6-8, the SFG spectrum of the ODT ( $C_{18}$ ) on gold in the HV cell with the peak's assignments is discussed to better compare the peak changes at low temperatures.

ODT SFG spectrum, as is shown in Figure 6-14, consists of six resonant vibrations, assigned as methylene symmetric stretch ( $d^+$ ), methylene adjacent to methyl symmetric stretch ( $d_t^+$ ), methyl symmetric stretch ( $r^+$ ), methyl Fermi resonance ( $r_{FR}^+$ ), methyl out-of-plane antisymmetric stretch ( $r_{op}^-$ ), and methyl in-plane antisymmetric stretch ( $r_{ip}^-$ ) vibration, respectively.

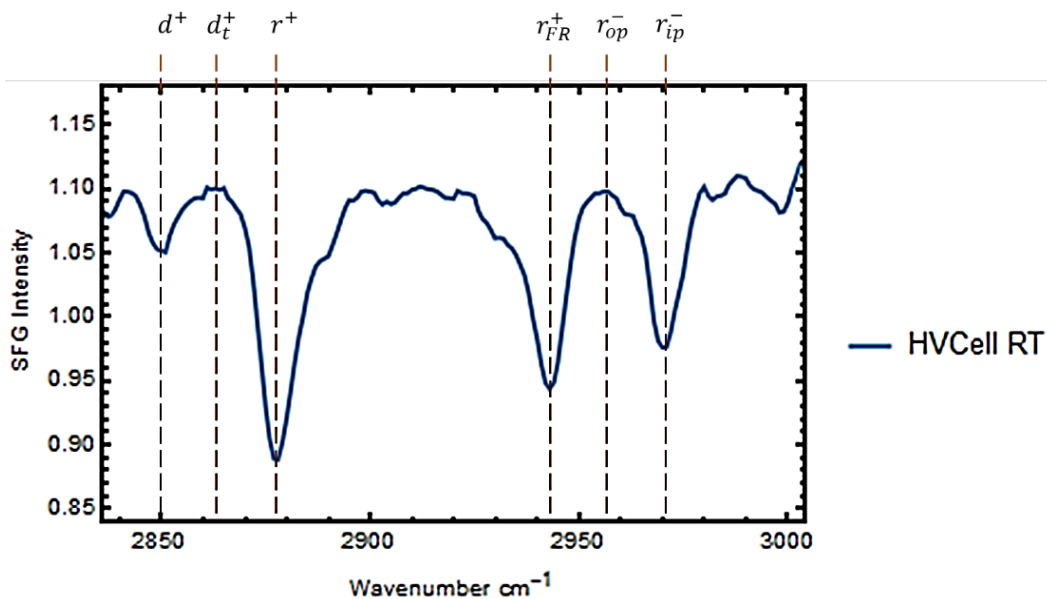


Figure 6-14 Decomposition of the C-H stretching region of ODT SFG data on gold.

These spectra are well fitted by the six resonances mentioned, and the fitting is shown in Figure 6-15.

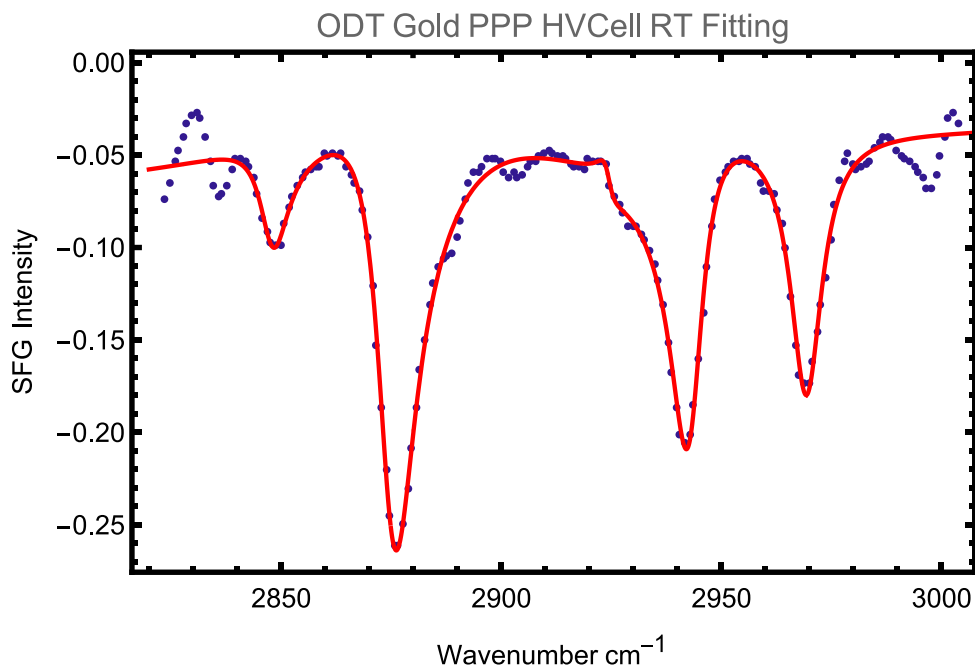


Figure 6-15 The PPP SFG data for ODT on a gold wafer and the fitting with six resonances.

It is hypothesized that the peak disappearance for the asymmetric C-H stretch mode is due to the reorientation of the methyl endgroup by decreasing the temperature. The asymmetric C-H stretching mode is composed of two modes: the in-plane asymmetric mode and the out-of-plane asymmetric mode. These two cases are shown schematically in Figure 6-16.

By following the intensity ratio and the wavenumber ratio of the two abovementioned modes, in comparison to the symmetric stretching mode, it might be observed that two modes cancel each other while the methyl endgroup is reorienting itself. Since there is no reported phase transition for SAMs at low temperatures, reorientation of the molecule is one of the highest possibilities for this observation. Further analysis is required to understand this phenomenon better, which is the future work direction to answer the newly unexpected observation in this experiment.

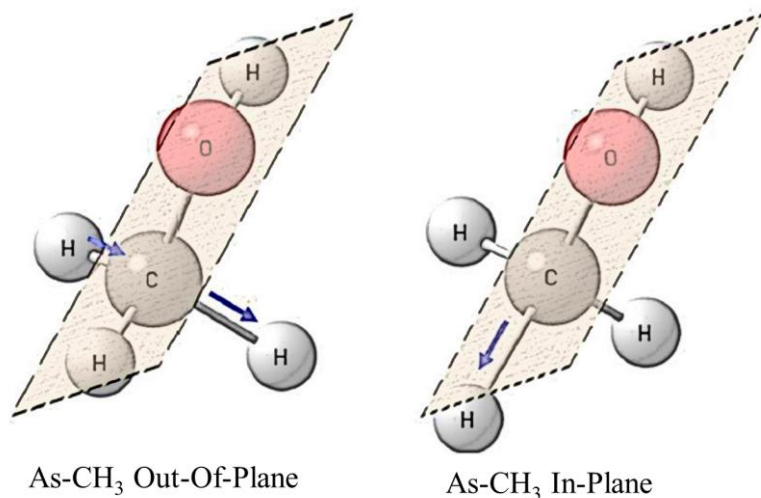


Figure 6-16 The Two in-plane and out-of-plane modes for asymmetric CH<sub>3</sub>

## 6.7 Conclusion

This chapter discusses an unexpected observation for a well-studied sample, showing the vast possibilities of high-vacuum or ultrahigh-vacuum experiments combined with the SFG technique. Future experiments on this sample and similar samples are required for a better understanding of the system.

## 6.8 Bibliography

- [1] H. Sellers, A. Ulman, Y. Shnidman, and J. E. Eilers, "Structure and binding of alkanethiolates on gold and silver surfaces: implications for self-assembled monolayers," *Journal of the American Chemical Society*, vol. 115, no. 21, pp. 9389-9401, 1993.
- [2] R. G. Nuzzo and D. L. Allara, "Adsorption of bifunctional organic disulfides on gold surfaces," *Journal of the American Chemical Society*, vol. 105, no. 13, pp. 4481-4483, 1983.
- [3] S. Kidoaki and T. Matsuda, "Adhesion forces of the blood plasma proteins on self-assembled monolayer surfaces of alkanethiolates with different functional groups measured by an atomic force microscope," *Langmuir*, vol. 15, no. 22, pp. 7639-7646, 1999.
- [4] A. Ulman, S. D. Evans, Y. Shnidman, R. Sharma, J. E. Eilers, and J. C. Chang, "Concentration-driven surface transition in the wetting of mixed alkanethiol monolayers on gold," *Journal of the American Chemical Society*, vol. 113, no. 5, pp. 1499-1506, 1991.
- [5] M. A. Reed, C. Zhou, C. Muller, T. Burgin, and J. Tour, "Conductance of a molecular junction," *Science*, vol. 278, no. 5336, pp. 252-254, 1997.
- [6] L. Bumm, J. Arnold, T. Dunbar, D. Allara, and P. Weiss, "Electron transfer through organic molecules," *The Journal of Physical Chemistry B*, vol. 103, no. 38, pp. 8122-8127, 1999.
- [7] J. Gooding, V. Praig, and E. Hall, "Platinum-catalyzed enzyme electrodes immobilized on gold using self-assembled layers," *Analytical Chemistry*, vol. 70, no. 11, pp. 2396-2402, 1998.
- [8] J. P. Folkers, P. E. Laibinis, and G. M. Whitesides, "Self-assembled monolayers of alkanethiols on gold: comparisons of monolayers containing mixtures of short- and long-chain constituents with methyl and hydroxymethyl terminal groups," *Langmuir*, vol. 8, no. 5, pp. 1330-1341, 1992.
- [9] H. Schönherr and H. Ringsdorf, "Self-assembled monolayers of symmetrical and mixed alkyl fluoroalkyl disulfides on gold. 1. Synthesis of disulfides and investigation of monolayer properties," *Langmuir*, vol. 12, no. 16, pp. 3891-3897, 1996.
- [10] G. M. Whitesides and B. Grzybowski, "Self-assembly at all scales," *Science*, vol. 295, no. 5564, pp. 2418-2421, 2002.
- [11] C. D. Bain, E. B. Troughton, Y. T. Tao, J. Evall, G. M. Whitesides, and R. G. Nuzzo, "Formation of monolayer films by the spontaneous assembly of organic thiols from solution onto gold," *Journal of the American Chemical Society*, vol. 111, no. 1, pp. 321-335, 1989.
- [12] R. G. Nuzzo, L. H. Dubois, and D. L. Allara, "Fundamental studies of microscopic wetting on organic surfaces. 1. Formation and structural characterization of a self-consistent series of polyfunctional organic monolayers," *Journal of the American Chemical Society*, vol. 112, no. 2, pp. 558-569, 1990.

- [13] Y.-S. Shon, R. Colorado, C. T. Williams, C. D. Bain, and T. R. Lee, "Low-density self-assembled monolayers on gold derived from chelating 2-monoalkylpropane-1, 3-dithiols," *Langmuir*, vol. 16, no. 2, pp. 541-548, 2000.
- [14] I. Wenzl, C. M. Yam, D. Barriet, and T. R. Lee, "Structure and wettability of methoxy-terminated self-assembled monolayers on gold," *Langmuir*, vol. 19, no. 24, pp. 10217-10224, 2003.
- [15] S. Lee *et al.*, "Structure, wettability, and frictional properties of phenyl-terminated self-assembled monolayers on gold," *Langmuir*, vol. 17, no. 23, pp. 7364-7370, 2001.
- [16] K. Cimatu, H. J. Moore, D. Barriet, P. Chinwangso, T. R. Lee, and S. Baldelli, "Sum frequency generation imaging microscopy of patterned self-assembled monolayers with terminal- CH<sub>3</sub>, - OCH<sub>3</sub>, - CF<sub>2</sub>CF<sub>3</sub>, - C = C, - Phenyl, and - Cyclopropyl Groups," *The Journal of Physical Chemistry C*, vol. 112, no. 37, pp. 14529-14537, 2008.
- [17] J.-S. Park, A. N. Vo, D. Barriet, Y.-S. Shon, and T. R. Lee, "Systematic control of the packing density of self-assembled monolayers using bidentate and tridentate chelating alkanethiols," *Langmuir*, vol. 21, no. 7, pp. 2902-2911, 2005.
- [18] R. Colorado and T. R. Lee, "Wettabilities of self-assembled monolayers on gold generated from progressively fluorinated alkanethiols," *Langmuir*, vol. 19, no. 8, pp. 3288-3296, 2003.
- [19] J. C. Love, L. A. Estroff, J. K. Kriebel, R. G. Nuzzo, and G. M. Whitesides, "Self-assembled monolayers of thiolates on metals as a form of nanotechnology," *Chemical Reviews*, vol. 105, no. 4, pp. 1103-1170, 2005.
- [20] Y. Han and K. Uosaki, "Effects of concentration and temperature on the formation process of decanethiol self-assembled monolayer on Au (1 1 1) followed by electrochemical reductive desorption," *Electrochimica acta*, vol. 53, no. 21, pp. 6196-6201, 2008.
- [21] D. H. Kim, J. G. No, H. Masahiko, and H. W. Lee, "An adsorption process study on the self-assembled monolayer formation of octadecanethiol chemisorbed on gold surface," *Bulletin of the Korean Chemical Society*, vol. 22, no. 3, pp. 276-280, 2001.
- [22] N. Nishida, M. Hara, H. Sasabe, and W. Knoll, "Thermal desorption spectroscopy of alkanethiol self-assembled monolayer on Au (111)," *Japanese Journal of Applied Physics*, vol. 35, no. 11R, p. 5866, 1996.
- [23] R. Yamada, H. Wano, and K. Uosaki, "Effect of temperature on structure of the self-assembled monolayer of decanethiol on Au (111) surface," *Langmuir*, vol. 16, no. 13, pp. 5523-5525, 2000.
- [24] J.-P. Bucher, L. Santesson, and K. Kern, "Thermal healing of self-assembled organic monolayers: hexane-and octadecanethiol on Au (111) and Ag (111)," *Langmuir*, vol. 10, no. 4, pp. 979-983, 1994.
- [25] E. Delamarche, B. Michel, H. Kang, and C. Gerber, "Thermal stability of self-assembled monolayers," *Langmuir*, vol. 10, no. 11, pp. 4103-4108, 1994.

[26] C. Vericat, M. Vela, G. Benitez, P. Carro, and R. Salvarezza, "Self-assembled monolayers of thiols and dithiols on gold: new challenges for a well-known system," *Chemical Society Reviews*, vol. 39, no. 5, pp. 1805-1834, 2010.

# Appendices

## Appendix A.1 Reported crystal structures of the ILs

Reported crystal structures of the ILs for prediction of the [EMIM][FSA] IL

File Number	Space Group	a	b	c	$\alpha$	$\beta$	$\gamma$
108042	P 2 <sub>1</sub>	5.378	10.383	11.316	90	91.72	90
116893	P b c a	11.896	12.704	12.950	90	90	90
148580	P n m a	9.894	13.846	19.856	90	90	90
217827	P 2 <sub>1</sub> /c	8.942	9.390	13.849	90	101.68	90
236629	P 1-	8.535	12.681	13.502	88.059	80.181	79.768
280603	P 2 <sub>1</sub> /c	8.653	9.285	13.217	90	121.358	90
280604	P 2 <sub>1</sub> 2 <sub>1</sub> 2 <sub>1</sub>	9.204	9.770	12.499	90	90	90
280605	P 2 <sub>1</sub> 2 <sub>1</sub> 2 <sub>1</sub>	9.216	9.763	12.502	90	90	90
293511	P 2 <sub>1</sub> /n	8.761	9.396	11.424	90	98.7	90
293513	P 2 <sub>1</sub> /n	10.222	12.534	22.541	90	93.28	90
614037	P c a 2 <sub>1</sub>	18.499	8.626	19.255	90	90	90
621179	P 2 <sub>1</sub> 2 <sub>1</sub> 2 <sub>1</sub>	8.28	10.788	11.998	90	90	90
629560	P 1-	9.374	13.016	14.992	107.23	99.859	93.312
639882	C c	14.090	9.719	17.167	90	107.356	90
639890	P 2 <sub>1</sub> /a	14.074	9.648	17.917	90	108.156	90
646908	P 1-	10.845	12.866	13.237	90.366	90.689	114.836
655868	P 2 <sub>1</sub> /c	8.624	20.820	7.967	90	113.38	90
701482	P 2 <sub>1</sub>	6.213	13.744	7.835	90	106.172	90
710931	P 2 <sub>1</sub> 2 <sub>1</sub> 2 <sub>1</sub>	8.496	13.123	16.692	90	90	90
713637	P n a 2 <sub>1</sub>	27.713	7.034	15.796	90	90	90
713639	P 1-	8.8314	9.985	12.040	99.53	99.581	106.367
715668	P 2 <sub>1</sub> /c	9.178	34.444	10.022	90	91.711	90
752344	P 2 <sub>1</sub> /c	12.036	12.480	19.024	90	105.6	90
769705	P 1-	10.307	16.172	25.595	73.875	87.515	87.742
794463	P 2 <sub>1</sub> /c	17.679	11.067	17.041	90	113.73	90
824302	P n a 2 <sub>1</sub>	9.657	11.141	14.651	90	90	90
824766	P 2 <sub>1</sub> /n	11.289	12.249	12.409	90	97.027	90
824768	P 2 <sub>1</sub> /n	11.516	12.279	12.507	90	96.726	90
824769	P 1-	8.212	8.684	12.621	98.692	104.289	104.167
835946	P 2 <sub>1</sub> /n	7.320	17.244	8.344	90	104.372	90
839609	P 2 <sub>1</sub> /c	9.412	14.654	12.444	90	129.841	90
869551	P 2 <sub>1</sub> /c	15.228	8.945	18.033	90	114.034	90
1100455	P 2 <sub>1</sub> /c	4.529	9.306	14.299	90	95.75	90
1138289	P 2 <sub>1</sub> /m	3.973	7.921	9.371	90	92.97	90
1270247	P 2 <sub>1</sub> /c	10.119	8.870	7.754	90	97.556	90
713638	P 2 <sub>1</sub> /n	12.124	8.4849	34.132	90	93.021	90

**Table A.1 continued**

File Number	T (C) K	T (m) K	r (Cation) Å	r (Anion) Å	$\frac{r (+)}{r (-)}$
108042	123	302	4.213	3.136	1.34
116893	123	246	5.598	4.065	1.38
148580	150		6.962	5.863	1.19
217827	200	283	7.268	3.667	1.98
236629	173	295	5.910	6.402	0.92
280603	100		7.212	2.278	3.17
280604	200		7.167	3.764	1.90
280605	200		7.174	3.735	1.92
293511	173	271.7	7.259	2.275	3.19
293513	200	279.7	7.982	3.748	2.13
614037	230	247.3	7.215	6.472	1.12
621179	93	270	8.483	2.060	4.12
629560	173	302	8.087	7.161	1.13
639882	113	296	9.170	4.041	2.27
639890	203	278	8.117	5.545	1.46
646908	193	302	7.556	7.250	1.04
655868	173		8.245	4.374	1.88
701482	123		7.160	5.969	1.20
710931	230		8.202	7.078	1.16
713637	100		7.287	7.085	1.03
713639	120		9.996	6.527	1.53
715668	173		7.285	7.477	0.97
752344	173		8.162	8.275	0.99
769705	193		19.647	12.547	1.57
794463	100	285	8.225	9.794	0.84
824302	213		5.816	7.119	0.82
824766	100		9.009	7.224	1.25
824768	100		9.615	6.618	1.46
824769	100		6.645	7.142	0.93
835946	173		7.767	2.920	2.66
839609	293		7.405	3.671	2.02
869551	100	308	14.25	6.519	2.19
1100455	231	270	4.018	3.004	1.34
1138289	163	272	4.633	2.325	1.99
1270247	225	267	3.466	3.694	0.94
713638	120		8.440	6.608	1.28

## Appendix A.2 Example of the reciprocal lattice vectors calculation:

Example of the calculation of the reciprocal lattice vectors of the [EMIM][TFSA]. Data is extracted from the simulation based on reported crystal structure for this IL. Because of its similarity to the IL studied in this thesis, the indexing is then used to compare with the [EMIM][FSA] IL.

$$S = \frac{\text{Pixle numbers} \times \text{Pixle Size}}{\text{Camera Length} \times \text{Wavelength}} \quad , \quad \varphi(xy) = \tan^{-1}\left(\frac{x \times a^*}{y \times b^*}\right)$$

$$S(01) = \frac{46 \times 29.6\mu\text{m}}{167 \text{ mm} \times 0.0697\text{\AA}} = 0.116 \text{ \AA}^{-1} \rightarrow b = 8.585 \text{ \AA} \quad , \quad \varphi = 0^\circ$$

$$S(20) = \frac{42.5 \times 29.6\mu\text{m}}{167 \text{ mm} \times 0.0697\text{\AA}} = 0.108 \text{ \AA}^{-1} \rightarrow \frac{a}{2} = 9.259 \text{ \AA} \rightarrow a = 18.518 \quad , \quad \varphi = 90^\circ$$

$$S(11) = \frac{49.5 \times 29.6\mu\text{m}}{167 \text{ mm} \times 0.0697\text{\AA}} = 0.125 \text{ \AA}^{-1} \rightarrow \sqrt{a^{*2} + b^{*2}} \quad , \quad \varphi = 25^\circ$$

$$S(21) = \frac{62 \times 29.6\mu\text{m}}{167 \text{ mm} \times 0.0697\text{\AA}} = 0.157 \text{ \AA}^{-1} \rightarrow \sqrt{(2a^*)^2 + b^{*2}} \quad , \quad \varphi = 43^\circ$$

$$S(31) = \frac{78 \times 29.6\mu\text{m}}{167 \text{ mm} \times 0.0697\text{\AA}} = 0.198 \text{ \AA}^{-1} \rightarrow \sqrt{(3a^*)^2 + b^{*2}} \quad , \quad \varphi = 54^\circ$$

$$S(41) = \frac{96.8 \times 29.6\mu\text{m}}{167 \text{ mm} \times 0.0697\text{\AA}} = 0.245 \text{ \AA}^{-1} \rightarrow \sqrt{(3a^*)^2 + b^{*2}} \quad , \quad \varphi = 62^\circ$$

$$S(12) = \frac{93 \times 29.6\mu\text{m}}{167 \text{ mm} \times 0.0697\text{\AA}} = 0.235 \text{ \AA}^{-1} \rightarrow \sqrt{a^{*2} + (2b^*)^2} \quad , \quad \varphi = 13^\circ$$

## Appendix A.3 Simulation Details

### Details of the crystal structure prediction of [EMIM][FSA]

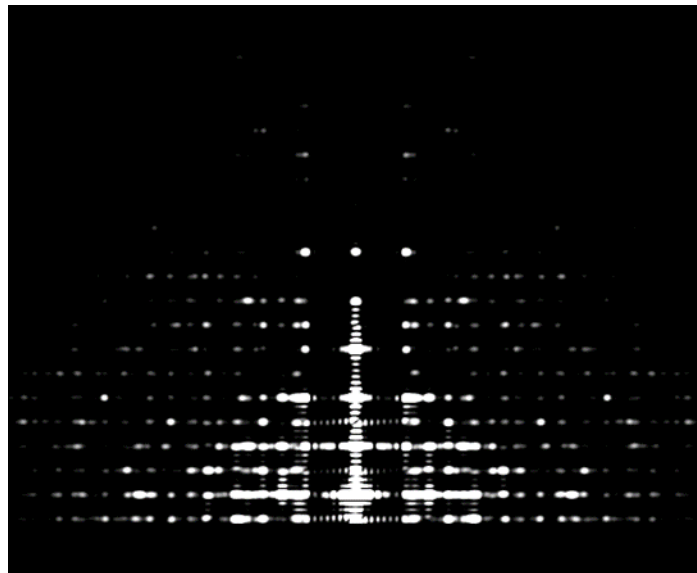
In this part, the details of the data analysis of the crystal structure prediction of the IL are discussed. The prediction is based on the simulated patterns of the [EMIM][TFSA] IL, which has been discussed in the main text to have a similar structure with the [EMIM][FSA] IL. The simulated patterns were generated based on

the kinematic scattering theory, which assumes that the intensity of the diffraction features is proportional to the square of the total scattered waves amplitude from all the atoms, or in the other word:

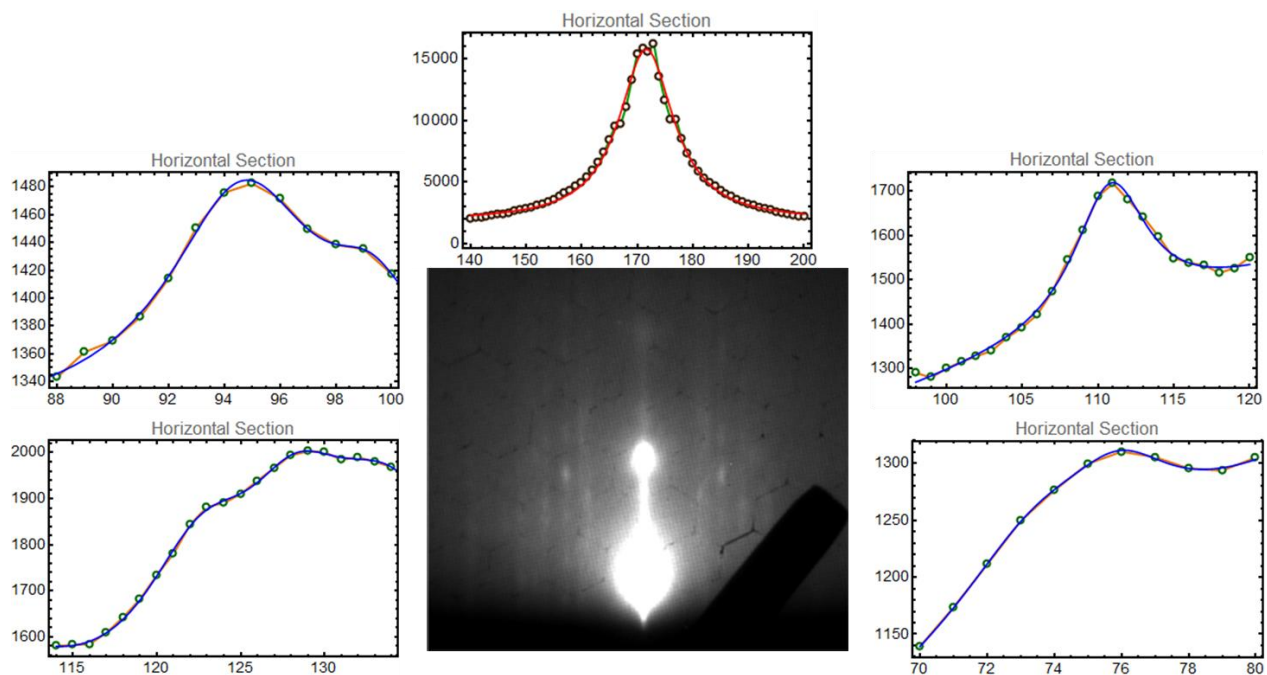
$$I \propto \left| \sum_j f_j^{(e)} \exp(-2\pi i \vec{s} \cdot \vec{r}_j) \right|^2$$

Where  $f_j^{(e)}$  is the atomic scattering factor of the  $j^{\text{th}}$  atom and  $s$  and  $r$  are the reciprocal and real lattice vectors.

The simulated pattern with  $c$ -vertical ( $a$ - $b$  plane parallel to HOPG surface) is shown below. Which is used for indexing the [EMIM][TFSA] IL diffraction pattern, and the output is then used for the [EMIM][FSA] IL to solve the structure.



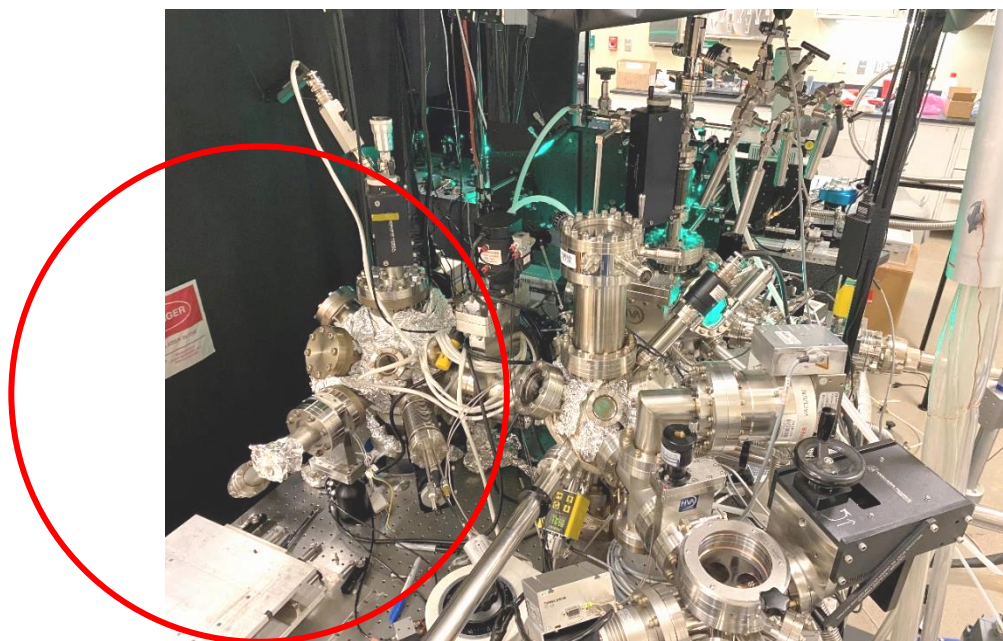
The [EMIM][FSA] IL peaks are first fitted with reasonable precision:



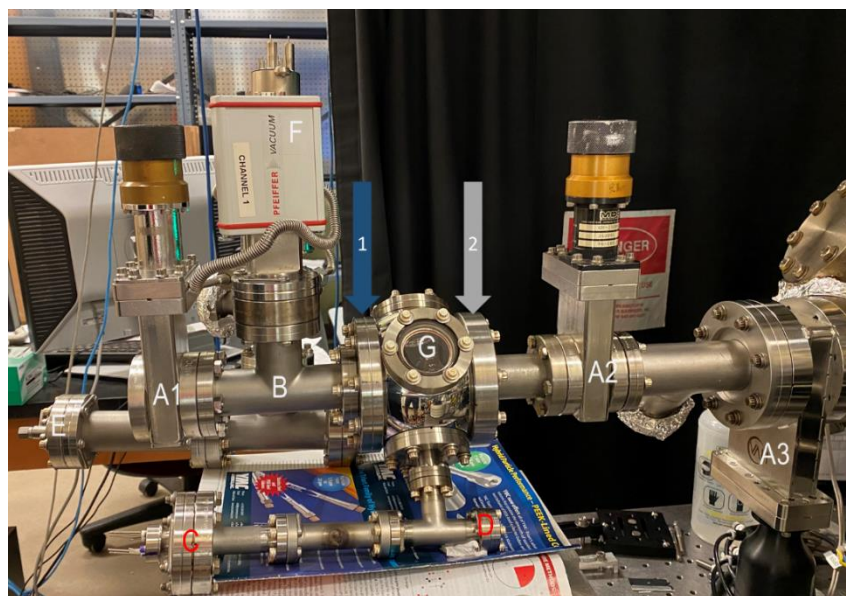
Furthermore, the S values are calculated the same as the example in the previous part for the [EMIM][TFSA] IL. Finally, in the last step, the inverse of the S vectors is assigned to the corresponding sets of planes (Indexing), which agrees with the rectangular unit cell assumption.

## Appendix B.1 Additional pictures of the portable chamber

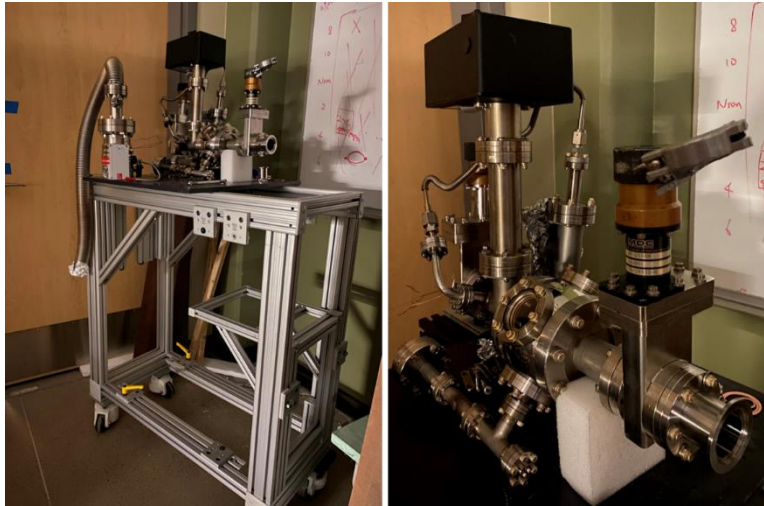
The actual RHEED setup and the location for the portable chamber next to the ionic liquid chamber.



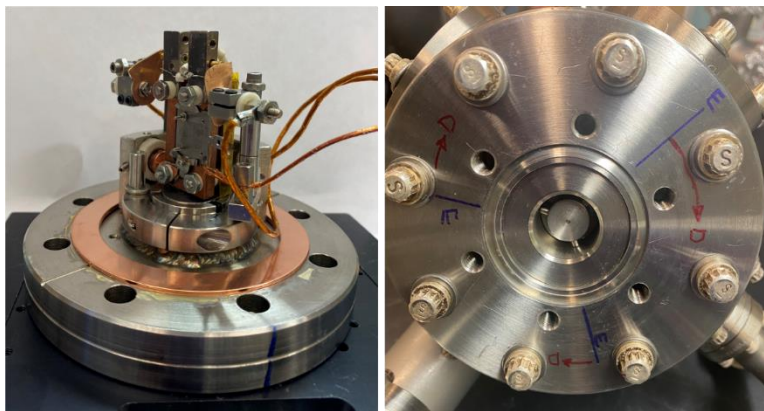
The portable chamber assembled on the IL chamber.



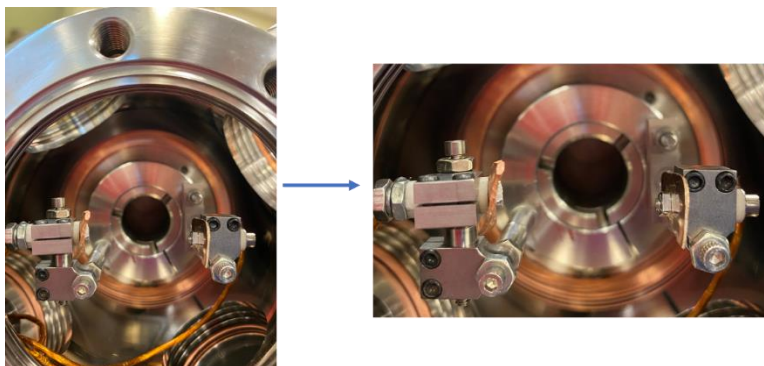
The portable chamber, detached from the IL, on the transfer cart.



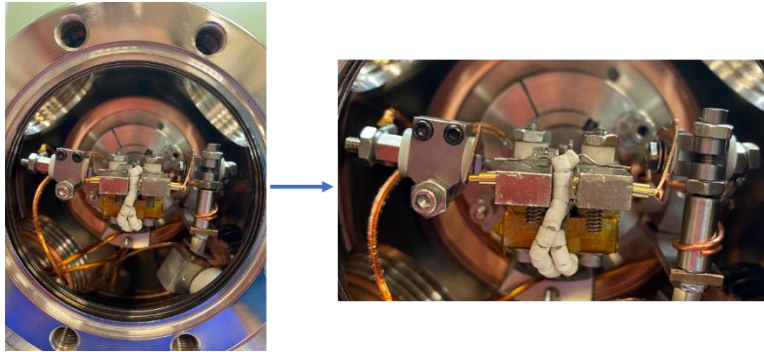
The custom-made sample car, sample receiver, and the back view of the pins for engagement with transfer arm.



Front view of the female section of the sample receiver for sample car engagement.



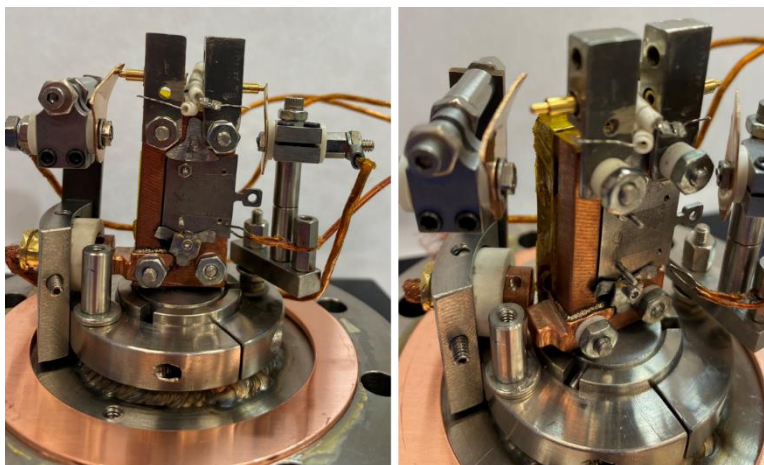
The front view of the sample car engaged on the sample receiver.



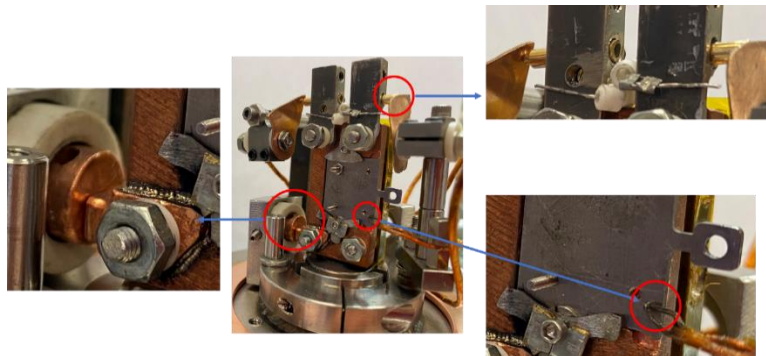
Disassembled sample car, with ceramic spacers, resistive heaters, and spring-loaded pins.



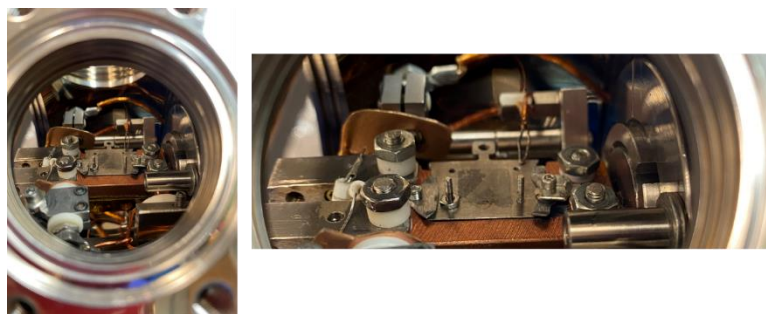
Engagement and disengagement of the electrical pins and the cold finger copper connections.



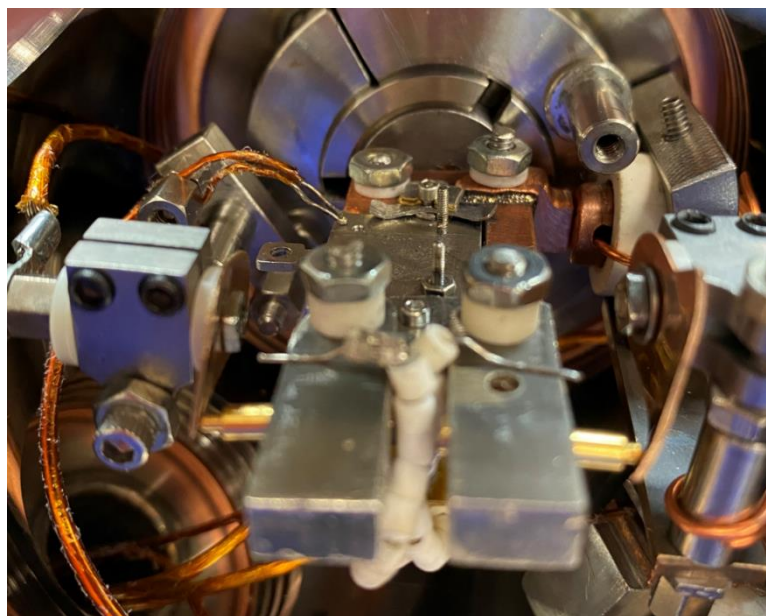
Close view of copper connection cold finger (left), electrical pins (top-right), thermocouple connection on the omicron plate (bottom-right).



Viewport view for SFG inputs and outputs, and the sample plate.



Front view of the sample car engaged, with all connections engaged at the same time.



The additional middle level with the transfer arm engagement holes, and adjustable height.



The dimensions of the transfer car (in mm).

